



TECHNISCHE  
UNIVERSITÄT  
WIEN

Vienna University of Technology

## DIPLOMARBEIT

# **Transition to superparamagnetic behaviour of magnetite nanoparticles used for hyperthermia applications**

Ausgeführt am Institut für Festkörperphysik  
der Technischen Universität Wien

unter der Anleitung von  
Univ.-Prof. Dipl.-Ing. Dr. techn. Josef Fidler  
Proj.-Ass. Dipl.-Ing. Gregor Zickler, B. Eng.

durch

Julia Toifl, B.Sc.  
Pappenheimgasse 67/2/11  
1200 Wien

---

Datum

---

Unterschrift

## Statutory Declaration

I herewith declare that I have authored this thesis independently and I have only used the declared sources/resources. I also declare that I have explicitly marked all materials which have been quoted either literally or by content from the used sources.

---

Place, Date

---

Signature

## Acknowledgements

First of all, I would like to express my thanks to my supervisor Univ.-Prof. Dipl.-Ing. Dr. techn. Josef Fidler for giving me the opportunity of this thesis and the great support and advice in the last months.

Special thanks are directed to my dear colleagues Gregor Zickler, Peter Toson, Ahmad Asali and Harald Huber for patiently answering all my questions and for being helpful and motivating every single day.

This diploma thesis would not have been possible without the cooperation with the University of Vienna. So, my sincere thanks go to Niusha Lasemi who did not only provide the investigated samples, but also her knowledge and time in a very friendly and obliging way.

Big thanks go to my parents Gerhard and Ingrid who supported me financially and mentally throughout my studies and never put me under pressure in the last five years.

My warm thanks to my sister, and friend, Elisabeth and my friends Angelika and Beate for every encouraging talk, for every time you listened understandingly and, of course, for proof-reading my diploma thesis.

And finally, I would like to thank Manuel for motivating me when I needed motivation, for pushing me when I needed to be pushed and for not saying anything at all, when all I needed was someone to listen. Thank you!

The funding from the European Community's Seventh Framework Programme (FP7-NMP) under Grant agreement no. 309729 (ROMEO) is acknowledged. TEM investigation was carried out using facilities at USTEM, TU Wien.

The author is grateful to Dr. Óscar Bomati-Miguel and his team from the Department of Applied Physics from the Universidad Autónoma de Madrid and to Univ.-Prof. Dr. Wolfgang Kautek from the Department of Physical Chemistry from the University of Vienna for providing the nanoparticle samples.

## Abstract

Magnetic nanoparticles are currently being explored as a widely usable tool in medical treatments. One of them is magnetic induction hyperthermia, where nanoparticles are directly injected or leaded to a tumour and are heated by an external alternating magnetic field. The produced heat can cause significant tumour necrosis.

The use of superparamagnetic nanoparticles in biomedical applications is of immense interest for today's research. Their magnetic properties, the knowledge of the transition to superparamagnetic behaviour and the influence of shape and material on these have to be understood to ensure medical treatments as accurate and secure as possible.

Therefore, the micromagnetic behaviour of four different models of nanoparticles, with respect to relevant shapes and materials in today's research, is simulated with the help of computational physics: Fe-sphere, Fe<sub>3</sub>O<sub>4</sub>-sphere, Fe<sub>3</sub>O<sub>4</sub>-disc and Fe<sub>20</sub>Ni<sub>80</sub>-disc. Two different kinds of numerical micromagnetic simulations based on the method of finite elements and the solution of the Landau-Lifshitz-Gilbert equation are performed, i.e. the magnetic field reversal and the thermal magnetization reversal using the nudged elastic band method. These simulations reveal the critical volume for superparamagnetic behaviour of magnetic nanoparticles and provide knowledge about the process of magnetization reversal.

Also, an investigation of real FeW nanospheres with a transmission electron microscope is approached. High resolution analysis and EELS as well as EDX measurements provide information about the geometry, crystal structure, size distribution and chemical composition of these nanospheres. Connecting the results of the performed simulations and the gained knowledge about the investigated FeW nanoparticles allow a statement about the suitability of the investigated real nanoparticles for biomedical applications.

The TEM investigations explored two different types of nanoparticles: homogenous and core/shell nanospheres with very broad size distributions. Various high resolution and FFT analysis made it possible to identify two different core crystal structures: Fe<sub>3</sub>O<sub>4</sub> and  $\alpha$ -Fe. Also EDX and EELS measurements confirmed a high amount of Fe in the core. HRTEM indicated the shell's crystal structure to be WO<sub>3</sub>.

At a defined time period between two switching processes by thermal activation of 100 seconds the micromagnetic simulations delivered the transition diameters to superparamagnetic behaviour for Fe<sub>3</sub>O<sub>4</sub> spheres (D=26.5 nm), Fe spheres (D=16.5 nm) and Fe<sub>3</sub>O<sub>4</sub> discs (D=29 nm, H=12 nm). Connecting the numerical and experimental results enabled the evaluation of the transition particle diameter for FeW nanoparticles to be 55 nm (Fe<sub>3</sub>O<sub>4</sub>-core) and 34 nm (Fe-core) for sample A1 and 52 nm (Fe<sub>3</sub>O<sub>4</sub>-core) and 32 nm (Fe-core) for sample B7. The amount of superparamagnetic particles lies between 23% - 43% for sample A1 and 37% - 71% for sample B7.

## Kurzfassung

Magnetische Nanoteilchen sind derzeit Objekt umfangreicher Forschungen im Bereich der medizinischen Behandlungen. Eine dieser ist Hyperthermie durch magnetische Induktion, wobei Nanopartikel direkt in einen Tumor injiziert werden. Durch Anlegen eines externen, alternierenden Magnetfeldes kommt es zu lokaler Hitzeentwicklung, die signifikante Tumornekrose verursachen kann. Ein tieferes Verständnis der magnetischen Eigenschaften von Nanoteilchen, deren Übergang zu Superparamagnetismus und den Einfluss von Form und Material ist wesentlich, um medizinische Behandlungen mit magnetischen Nanoteilchen so sicher und präzise wie möglich zu machen.

Deshalb wird das mikromagnetische Verhalten von vier verschiedenen Modellen von Nanopartikeln mithilfe von Computersimulationen untersucht: Fe-Kugeln, Fe<sub>3</sub>O<sub>4</sub>-Kugeln, Fe<sub>3</sub>O<sub>4</sub>-Scheiben und Fe<sub>20</sub>Ni<sub>80</sub>-Scheiben. Zwei unterschiedliche Arten von numerischen, mikromagnetischen Simulationen, beide basierend auf der Methode der Finiten Elemente und der Lösung der Landau-Lifshitz-Gilbert Gleichung, werden durchgeführt, z.B. die Ummagnetisierung mittels externem Feld und die Ummagnetisierung ausschließlich herbeigeführt durch thermische Fluktuationen, die durch die Nudged Elastic Band-Methode realisiert wird. Diese Simulationen liefern das kritische Volumen, ab dem Superparamagnetismus auftritt, und ein tieferes Verständnis über den Prozess der Ummagnetisierung.

Außerdem werden reale FeW-Nanoteilchen anhand eines Transmissionselektronenmikroskops untersucht. Die Hochauflösungsanalyse sowie EELS- und EDX-Messungen liefern Informationen über die Geometrie, Kristallstruktur, Größenverteilung und chemische Zusammensetzung dieser Nanopartikel. Das Zusammenführen der Simulationsergebnisse und dem gewonnenen Wissen über die realen FeW-Nanoteilchen ermöglicht es, eine Aussage über die Eignung der FeW-Nanopartikel für biomedizinische Anwendungen zu treffen.

Die TEM-Untersuchungen offenbarten zwei verschiedene Typen von Nanopartikeln: homogene Kugeln und Kugeln mit einer Kern/Schale-Struktur mit breiten Größenverteilungen. Mehrere Hochauflösungsbilder und FFT Analysen ermöglichten die Identifikation zweier unterschiedlicher Kernkristallstrukturen: Fe<sub>3</sub>O<sub>4</sub> und  $\alpha$ -Fe. Auch EDX und EELS Messungen bestätigten einen hohen Gehalt von Fe im Kern. HRTEM deutete auf eine WO<sub>3</sub>-Kristallstruktur der Schale hin.

Für eine definierte Zeit zwischen zwei Umklappprozessen verursacht durch thermische Aktivierung von 100 Sekunden lieferten die Simulationen die Übergangsdurchmesser zu superparamagnetischen Verhalten für Fe<sub>3</sub>O<sub>4</sub> Kugeln (D=26.5 nm), Fe-Kugeln (D=16.5 nm) und Fe<sub>3</sub>O<sub>4</sub>-Scheiben (D=29 nm, H=12 nm). Durch Zusammenführen von numerischen und experimentellen Ergebnissen ergeben sich die Übergangparameter für FeW-Nanopartikel zu 55 nm (Fe<sub>3</sub>O<sub>4</sub>-Kern) und 34 nm (Fe-Kern) für Probe A1 und 52 nm (Fe<sub>3</sub>O<sub>4</sub>-Kern) und 32 nm (Fe-Kern) für Probe B7. Der Anteil an superparamagnetischen Teilchen liegt folglich zwischen 23% - 43% für Probe A1 und 37% - 71% für Probe B7.

# Content

Statutory Declaration.....	II
Acknowledgements .....	III
Abstract .....	IV
Kurzfassung.....	V
1 Introduction.....	1
1.1 Nanoparticles – a brief retrospect.....	1
1.2 Application in Industry .....	2
1.3 Magnetic Nanoparticles in Biology.....	2
1.4 Application in Medicine .....	3
1.4.1 Hyperthermia Therapy .....	3
1.4.2 Contrast Agents in Magnetic Resonance Imaging (MRI).....	5
1.4.3 Drug Delivery.....	6
1.4.4 Applicable Materials .....	6
1.4.5 Applicable Geometries .....	8
2 Theoretical Background.....	11
2.1 Superparamagnetism .....	11
2.2 Theory of Micromagnetism .....	12
2.2.1 Gibbs free energy .....	12
2.2.2 Exchange energy .....	12
2.2.3 Anisotropy energy .....	13
2.2.4 Magnetostatic Self-Interaction .....	15
2.2.5 Zeeman Energy .....	15
2.2.6 Energy Minimization.....	15
2.3 The Stoner-Wohlfarth Model .....	17
2.4 Numerical Finite Element Micromagnetism .....	19
2.4.1 Hysteresis Loop Modelling (Magnetic Field Reversal).....	19
2.4.2 Thermal Magnetization Reversal (Nudged Elastic Band Method).....	25
3 Results of Micromagnetic Simulations of Fe-, Fe <sub>3</sub> O <sub>4</sub> - and Fe <sub>20</sub> Ni <sub>80</sub> -Nanoparticles.....	26
3.1 Superparamagnetic Transitions of Fe <sub>3</sub> O <sub>4</sub> -Spheres .....	26
3.2 Superparamagnetic Transitions of Fe-Spheres .....	33
3.3 Superparamagnetic Transitions of Fe <sub>3</sub> O <sub>4</sub> -Discs .....	38
3.4 Micromagnetic Simulation of Fe <sub>20</sub> Ni <sub>80</sub> -Discs .....	42

4	TEM-Characterization of FeW Nanospheres.....	45
4.1	Experimental Procedure .....	45
4.2	Preparation of FeW Nanoparticles .....	46
4.3	Description of the Investigated Samples .....	48
4.4	Determination of the Size Distribution.....	52
4.4.1	Size Distribution of Sample A1 .....	52
4.4.2	Size Distribution of Sample B7.....	54
4.5	Analysis of the Crystal Structure and Chemical Composition .....	55
4.5.1	Characterization of Sample Set (A) .....	55
4.5.2	Characterization of Sample Set (B).....	55
5	Discussion .....	62
5.1	Combining of Numerical and Experimental Results.....	62
5.2	Comparison of Fe <sub>3</sub> O <sub>4</sub> -Spheres and Fe <sub>3</sub> O <sub>4</sub> -Discs .....	64
5.3	Appearance of Incoherence for Fe <sub>20</sub> Ni <sub>80</sub> -Discs.....	64
6	Conclusions and Outlook.....	65
7	References.....	66
8	List of Figures .....	70
9	List of Tables .....	73
10	Appendix .....	74
10.1	hkl Tables .....	74
	Curriculum Vitae.....	80

# 1 Introduction

## 1.1 Nanoparticles – a brief retrospect

Against common beliefs nanoparticles have played a role in human history for a long time. Due to the fact that there exist natural nanoparticles, produced by weathering or volcano eruptions, their usage can be traced back to ancient times. Although the Romans did not know they were using magnetic nanoparticles as colour pigments in glass technology, the fabricated glass showed special optical properties like the famous Lycurgus Cup from the 4<sup>th</sup> century A.D. (figure 1), which today can be found in the British Museum in London. To receive the characteristic red colour of this ruby glass, gold nanoparticles have been used. It appears with a green colour when light comes from the outside and turns to red when it is illuminated from the inside.



Figure 1: The Lycurgus Cup in reflected (left) and in transmitted (right) light.  
© Trustees of the British Museum [1]

Like many other ancient technological approaches, this technique of colouring glass has been forgotten in medieval times and rediscovered in Europe in the seventeenth century. The first official scientific approach in nanotechnologies can be defined as Michael Faraday's work in the 1850's. He did systematic research on the interaction of light with metal, especially gold nanoparticles. This intense research resulted in his publication „Experimental Relations of Gold (and other Metals) to Light“, which was presented to the Royal Society of London in 1857 [2]. With the invention of the scanning tunnelling microscope and the knowledge about size-dependent effects such as the quantum size effect, the term „nanotechnology“ was born in the 1980's. These size-dependent effects can be observed in relation to, for instance, electronic or magnetic properties of a material. A very interesting magnetic property at nanoscale is called superparamagnetism which describes a magnetization reversal of a ferromagnetic material due to thermal activation energy and without an external field. This phenomenon will be explained in detail in upcoming chapters. In 2008, the International Organization for Standardization (ISO) defined a nanoparticle as a discrete nano-object where all three Cartesian dimensions are more than 1 nm and less than 100 nm [3]. Due to the endless possibilities nanomaterials offer to industry, medicine and also pharmacy, nanotechnology is nowadays one of the most funded and invested in research areas worldwide.



## 1.2 Application in Industry

Nanoparticles can be found in many different fields of industry. In this section only a broad overview of industrially applied nanoparticles is given, because the nanoparticles investigated in this diploma thesis lead the focus to the medical application.

Nanoparticles appear in nearly every aspect of daily life. For instance, easy cleanable surfaces on ceramics and glasses have been made possible by nanoceramic particles [4]. Also scratch resistant surfaces like in sunglasses make use of nanocomposites. Big branches such as the textiles [5] or cosmetics [6] industries could not be imagined without the support of nanotechnology today. Specially engineered nanofibers ensure water-repellence and wrinkle-avoidance in clothes. Titanium oxide nanoparticles are used in sunscreens [6] because they offer comparable UV protection properties and due to the fact that titanium dioxide is transparent at nanoscale the effect of white sunscreen on the skin is avoided.

In addition, also the construction branch gains from nanotechnology. Nowadays steel design is focused on the reduction of stress risers, which are later on responsible for initial cracks. These cracks can cause fatigue failure during the life cycle of the steel construction. To avoid these cost-intensive cracks, copper nanoparticles are added to the surface to increase evenness of the steel [7]. In further consequence, the use of nanoparticles leads to a higher lifespan of buildings and better safety.

## 1.3 Magnetic Nanoparticles in Biology

The ability of certain animals such as migratory birds to orient and navigate according to the earth's magnetic field has always fascinated humanity. Until today, the origin of this effect called magnetoreception has not been fully understood. There exist two main hypotheses nowadays which do not exclude each other [8]: The first one is based on the idea that due to the exposure to blue light a pair of radicals is formed which is affected by the earth's magnetic field because of its two unpaired electrons. The second explanation involves the existence of small particles of magnetite in the body. These magnetite nanoparticles would be able to correspond to the earth's magnetic field.

This hypothesis has gotten rising attention in the last decades: In 1975, Richard Blakemore [9] announced the discovery of so-called magnetotactic bacteria. This special type of bacteria demonstrates a

behaviour called magnetotaxis, which describes the fact that the bacterium is able to orient itself and also migrate in the direction of the earth's magnetic field. This is possible because the bacteria contains magnetite nanoparticles which form in chains and are therefore able to act as magnetic dipoles. Figure 2 illustrates a magnetotactic bacterium with well-visible magnetite nanoparticles inside. The appearance of magnetite in the heads of birds has been proven by several research groups [10], [11].



Figure 2: Magnetotactic bacteria containing chains of magnetic crystals [11]

## **1.4 Application in Medicine**

### **1.4.1 Hyperthermia Therapy**

The term “hyperthermia” defines a body temperature above the normal value of approximately 37°C. Artificially induced hyperthermia is nowadays a highly investigated field of research in medicine. Especially in cancer treatment hyperthermia has shown some promising results in recent years [12].

The aim of the hyperthermia treatment is to kill or weaken tumour cells without damaging healthy cells. Tumour cells have a disorganized and compact vascular structure, which makes it more difficult for them to dissipate heat than for normal cells [13]. Therefore hyperthermia can cause tumour necrosis or make the tumour cells more sensitive for additional treatments. For instance, chemotherapy drugs have a higher impact at higher temperatures, which enables the use of a lower dose of these drugs and a reduction of drug side effects. Also radiotherapy has shown good compatibility with hyperthermia treatments [14]. Due to their poor vascular structure tumour cells show low pH and oxygen concentrations which make them often resistant to radiation damage due to the low amount of free radicals. An additional hyperthermia therapy heats the tumour and therefore increases the blood flow, causing a rising oxygen rate [15].

#### **1.4.1.1 Methods of Heating**

Depending on the type of cancer there are different kinds of hyperthermia therapies. If there are already metastases in different parts of the body, whole body hyperthermia can be applied. In combination with chemotherapeutic drugs hot water blankets or thermal chambers can be used to heat up a body to a temperature of 42°C [16]. Unfortunately, whole body hyperthermia is accompanied by side effects such as vomiting, dizziness or nausea. Also the circumstance that the whole body is heated unnecessarily and many healthy cells are strained causes a lot of scepticism.

A better approach to treat tumours is local hyperthermia. The principle is to directly aim the tumour and therefore not unnecessarily heat healthy cells all over the body. To deliver heat, different techniques have been developed using ultrasound, microwave heating and also magnetic hyperthermia.

#### **1.4.1.2 Magnetic Hyperthermia**

Magnetic hyperthermia is based on the idea that magnetic nanoparticles can produce heat by transforming the electromagnetic energy of a high-frequency field to thermal energy. The magnetic nanoparticles, mostly suspended in a fluid, are either injected directly into the tumour or lead to tumour with the help of external magnets. If then the patient is put in an alternating external field with a frequency between several kHz and 1MHz [17], only the tissue, with the magnetic nanoparticles inside, is heated. The average temperature which is reached in this type of local hyperthermia treatment is 42°C to 46°C [17].

The heating itself is accomplished by several independent heating mechanisms which partly show bigger effects at nanoscale. In case of superparamagnetic nanoparticles, they show no ferromagnetic properties until aligned by an external field. In further consequence, the

nanoparticles can remain in the patient's body after a hyperthermia treatment because they do not cause a remanent field in the body. So, multiple hyperthermia treatments can be realized following only one injection of nanoparticles. Furthermore, the probability of an aggregation of superparamagnetic nanoparticles is smaller because they do not attract each other magnetically. Also, superparamagnetic particles allow better control over the treatment due to the fact that these nanoparticles provide a strong response to an external field [18]. The commonly used material for magnetic hyperthermia treatment is  $\text{Fe}_3\text{O}_4$  [19].

The heating mechanisms inside small particles in an external, alternating field are hysteresis losses, Brownian rotation, eddy current heating and susceptibility losses. Hysteresis loss appears due to the reversal of magnetization when an alternating field is applied. Whenever the field changes its direction, also the magnetic moments inside the nanoparticles change their orientation. The power needed for the realignment after every sweep of the field is known as hysteresis loss. Depending on the size distribution of the nanoparticles and the frequency of the external field, hysteresis loss can contribute significantly to the heating process.

Brownian rotation describes the fact that particles in a fluid can rotate to align their moments in the direction of the external field. The appearance of particle rotation depends on the viscosity of the fluid, the particle volume and also the temperature. The exact influence of Brownian rotation to heating efficiency is hard to define due to the possibility of nanoparticles not able to rotate because of sticking.

The third heating mechanism is based on susceptibility losses. When a particle is located in an alternating field, the moments oscillate to stay aligned with the field, which causes susceptibility losses proportional to the frequency of the field.

When a changing field is applied, the electrical conductivity of the particles induces eddy currents on the surface of the particles. These eddy currents also produce heat, but they also cause limiting effects on hysteresis and susceptibility losses by affecting the impact of the field on the nanoparticles. Eddy currents are not relevant for magnetic hyperthermia due to the fact that they are negligible for particles with a diameter under 100 nm, if the frequency of the applied field is less than 10 GHz [20].

Which heating mechanism occurs, depends on the particle size, but it is uncertain which mechanism is typically characteristic for a specific particle volume. Depending on the particle size distribution more than one mechanism can appear simultaneously.

Up to now, magnetic hyperthermia has not become a widely used standard-therapy in cancer treatment. The first company in the European Union to receive the approval for treatment of brain tumours using magnetic hyperthermia was the MagForce AG [21]. Applying their „NanoTherm therapy“, they inject nanoparticles of approximately 15 nanometres diameter with an iron oxide core and an aminosilane coating into tumours and then apply a field which changes polarity up to 100.000 times per second. The treatment either irreparably damages tumour cells or sensitizes them for additional chemo- or radiotherapy.

### 1.4.2 Contrast Agents in Magnetic Resonance Imaging (MRI)

The commonly used method to image physiological processes and the anatomy of a body is magnetic resonance imaging. It represents the state-of-the-art medical imaging technique in radiology. MRI scanners use strong magnetic fields, radio waves and field gradients to form images of the body.

MRI is based on the idea that strong magnetic fields excite the hydrogen nuclei of the body resonantly which induces an electric signal. The contrast of the image is caused by the fact that different types of tissue have different relaxation times. With MRI contrast agents the visibility of internal body structures can be improved. These nanoparticles shorten the relaxation times of atoms within body tissues which causes a better contrast (figure 3).

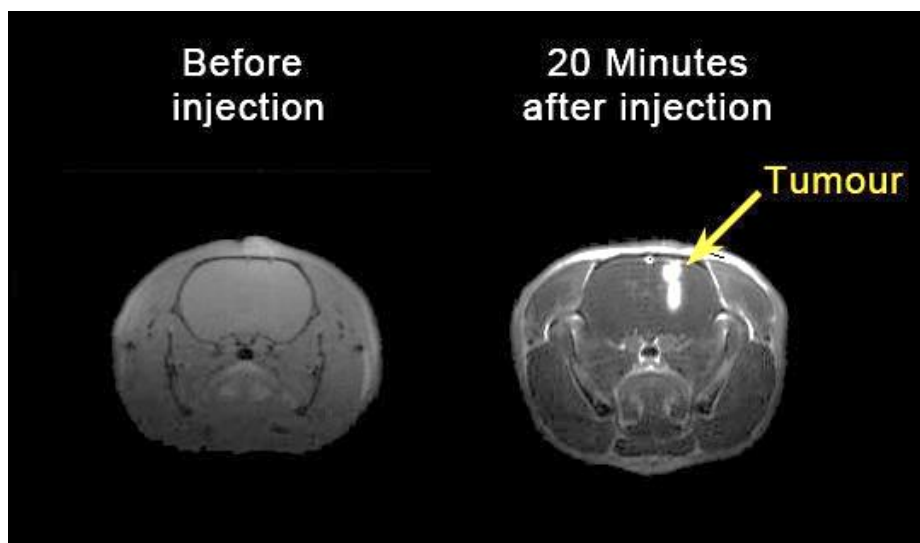


*Figure 3: MRI images of rat brain glioma before and 20 minutes after injection of gadolinium nanoparticles [22]*

The widely used nanoparticles are lanthanide metals containing gadolinium ions which is used for enhancement of vessels and to improve the visibility of tumours. After the imaging the gadolinium in the body distributes in the body and is finally eliminated by the kidneys.

Also superparamagnetic iron oxide nanoparticles, so called SPIONs, are in use as contrast agents. Their good biocompatibility and the fact that iron oxide is easily degradable by the body enables a lot of possible uses in medical applications for iron oxide nanoparticles, which will be focused on in chapter 1.5.1.

### 1.4.3 Drug Delivery

Modern technology enables the usage of magnetic nanoparticles for drug delivery by attaching drugs to the magnetic nanoparticle. This idea was born in the 1978 by Senyi, Widder and colleagues [23].

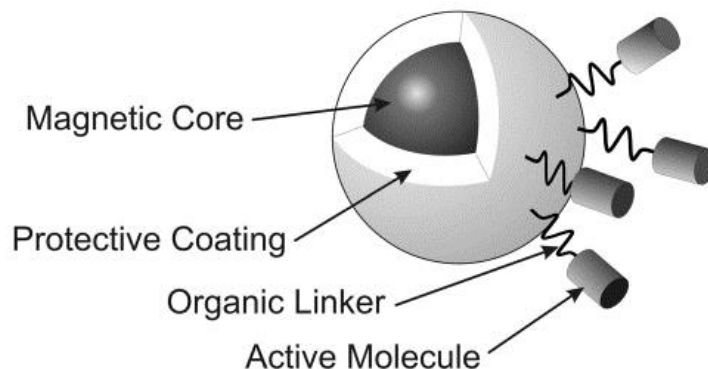


Figure 4: Possible design for a drug delivering nanoparticle [24]

The basic idea is that therapeutic agents are either attached to or encapsulated inside a magnetic nanoparticle. The nanoparticle then, including the drug, is injected into the bloodstream or, if possible, near the target tissue. Exact targeting is enabled by external magnetic fields which can force the nanoparticles in a determined direction. Once the nanoparticle has reached the target area, the drug, in form of active biomolecules, can be released. This concept is most efficient, if the target is near the body surface because of the better interaction of field and nanoparticles. A possible model for a drug carrying nanoparticle can be seen in figure 4. To widen this application to organs deeper in the body, there is recent research on implanting magnets near the target [25].

### 1.4.4 Applicable Materials

Principally, materials which show high saturation magnetization are preferred for biomedical use because they show higher sensitivity and efficiency [26]. High saturation magnetization is a property of, for instance, transition metals such as Fe, Ni or Co or metal oxides like  $\text{Fe}_3\text{O}_4$  or  $\text{Fe}_2\text{O}_3$ . Due to the fact that pure metals are toxic and extremely sensitive to oxidation, they are not relevant for biomedical applications. In contrast, iron oxides are highly biocompatible and show a strong magnetic response [27]. In addition, iron oxide magnetic nanoparticles are chemically stable, which is also an important property for biomedical applications. In consequence to these advantageous properties of iron oxide magnetic nanoparticles, they have become the object of interest in research concerning biomedical applications such as the mentioned magnetic hyperthermia, magnetic resonance imaging and drug delivery.

#### 1.4.4.1 Magnetite ( $\text{Fe}_3\text{O}_4$ ) nanoparticles

Magnetite is one of the longest known naturally magnetic materials in human history. The term “magnetite” traces back from the location Magnesia in Asia Minor, where large deposits of magnetite were discovered [28]. The use of navigational devices based on magnets goes back to Chinese sailors of the eleventh century [29]. Since 200 B.C. these natural magnets,

also nickname “lodestones”, have been used as fortune-telling devices [30]. As it can be seen, this naturally occurring magnetic material offers many interesting properties which can find application in diverse research areas.

$\text{Fe}_3\text{O}_4$  shows a cubic inverse spinel structure which consists of a cubic close packed array of oxide ions where all of the  $\text{Fe}^{2+}$  ions occupy half of the octahedral sites and the  $\text{Fe}^{3+}$  are split across the remaining octahedral sites and the tetrahedral sites.

$\text{Fe}_3\text{O}_4$  is ferrimagnetic caused by the fact that the electron spins of the  $\text{Fe}^{\text{II}}$  and  $\text{Fe}^{\text{III}}$  ions in the octahedral sites are coupled and the spins of the  $\text{Fe}^{\text{III}}$  ions in the tetrahedral sites are coupled but anti-parallel to the first ones. The net effect is that the magnetic contributions of both sets are not balanced and there is a permanent magnetism. Due to the spinel type structure there are six easy directions corresponding to the three  $\langle 111 \rangle$  axes, in which anisotropy energy is minimal [31].

Magnetite plays an essential role in today’s research in magnetic nanoparticles for biomedical applications. Special attention is paid to so-called SPIONs (superparamagnetic iron-oxide nanoparticles). SPIONs consist of cores made of iron oxides that can be targeted to a required area with the help of external magnets. Their superparamagnetism eliminates a main reason for agglomeration, the magnetic force. Also, their small sizes prevent from deposition caused by gravitation [32]. These targeted nanoparticles are helpful to reduce the necessary amount of drugs for medical treatments such as hyperthermia in combination with chemotherapy. A reduction of side effects is the logical consequence.

The typical structural configuration of a SPION is formed by a magnetic particle core which is usually made of magnetite or maghemite and a coating consisting of a biocompatible polymer. The coating shields the magnetic core from the environment and can also contain attachment points for cytotoxic drugs or antibodies [33].

The necessary external field is usually generated by a strong permanent magnet like Nd-Fe-B and is fixed outside the body. The SPIONs, mostly in form of a ferrofluid, are then injected into the patient and localized at the target with the help of the external magnets. The drug can then be released by changes in physiological conditions such as temperature or pH or by enzymatic activity [34].

So far, biocompatible SPIONs using magnetite cores have been widely used for in vivo biomedical applications such as release of therapeutic agents [35], magnetic resonance imaging [36] and hyperthermia. SPIONs with core sizes of 3-6nm and dextran coating such as Endorem, Feridex or Combidex have already been approved for MRI in patients [37].

#### **1.4.4.2 Another approach: Gold nanoparticles**

Due to the long relationship between mankind and gold in medical concerns, such as the “Aurum potable”, the “drinkable gold”, used for the diagnosis of syphilis until the 20<sup>th</sup> century [38], the material gold is also an issue in today’s medical research.

In recent years gold nanoparticles have gained attention for possible applications in biomedicine due to their promising biocompatibility, stability and low toxicity. The range of gold nanoparticle use in biomedicine is extremely broad. Research areas include biosensorics, detection, targeted drug delivery, optical bioimaging etc. This broad range is caused by the

unique electronic, optical and physical properties of gold nanoparticles. Especially the surface plasmonics theory provides great possibilities in biosensorics. The collective excitation of conduction electrons results in plasmon resonance, which represents the basic detection mechanism in gold-based bio-sensors [39].

### **1.4.5 Applicable Geometries**

In further consequence of the tremendous interest in nanoparticle research for biomedical applications, not only appropriate materials are searched for, but also the influence of different shapes of magnetic nanoparticles is highly investigated these days. On the next pages a brief insight about potential geometries and their advantages is provided.

#### **1.4.5.1 Nanospheres**

The only nanoparticle geometry which has already taken the step from research to practical application is the spherical nanoparticles. In use for hyperthermia treatments in human bodies by MagForce AG [21], a leading company in the usage of magnetic nanoparticles for cancer treatment, and certified by the U.S. Food and Drug Administration (FDA) [40], it is the only established and widely used geometry for nanoparticles for magnetic hyperthermia these days. Although nanospheres show promising results, research groups are currently looking for ways to optimize the heating efficiency of nanoparticles to reduce the amount of nanoparticles for a hyperthermia treatment to an amount as low as possible.

#### **1.4.5.2 Nanodiscs**

One approach to gain higher heating efficiency are nanodiscs. In 2015, Yang et al. [36] presented a comparison between the magnetic hyperthermia properties of nanospheres and nanodiscs, both made of  $\text{Fe}_3\text{O}_4$ . Their results revealed that nanodiscs show a much higher specific absorption rate (SAR) than their isotropic counterparts. The specific absorption rate is a measure for the ability of a particle to produce heat in consequence of an applied alternating field. In many industrial applications such as mobile phones a high SAR value is unwelcome, but in hyperthermia treatments it is highly desirable. The commonly used unit for a SAR value is watts per gram of nanoparticles

Yang et al. [36] supposed that the parallel alignment of the nanodiscs in respect to the applied ac field, is the reason for the higher SAR values. This hypothesis was confirmed by the good agreement of their experimental results and magnetic simulations. According to Yang et al. the observed parallel alignment could enhance the SAR value by a factor of 2 compared to the randomly oriented case. To overcome the difficulty of producing nanodiscs of monodispersed size, for instance Tiberto et al. [41] developed a new method to produce  $\text{Fe}_{20}\text{Ni}_{80}$  nanodiscs by nanosphere lithography. This promising method will be discussed in chapter 3.4, where also magnetic simulations will be performed to gain further knowledge about the magnetic properties of  $\text{Fe}_{20}\text{Ni}_{80}$  nanodiscs.

### 1.4.5.3 Nanocubes

Another highly investigated shape for magnetic nanoparticles is the cubic geometry. Focussing on magnetic hyperthermia, the optimization of the heating efficiency of the nanoparticles is a main goal.

To compare the heating properties of nanocubes and nanospheres Boubeta et al. [42] performed an experimental and theoretical analysis of both geometries.

The results of Boubeta et al. demonstrate that cubic iron oxide particles have superior magnetic heating efficiency compared to spherical particles of similar sizes. As an explanation for the higher SAR value, they assume the chain-like particle assembling of the nanocubes (figure 5(b)) and also the higher surface anisotropy of cubic nanoparticles than spherical ones.

The cubics' tendency towards aggregation into chains which is facilitated by the cubic shape is assumed to be the main source of the higher heating efficiency of nanocubes in comparison to nanospheres. These results represent another milestone in achieving minimal particle concentration in tissue for a magnetic hyperthermia treatment.

Also, for biomedical imaging such as magnetic resonance imaging, nanocubes showed promising results. In 2010, Zhen et al. [43] managed to produce highly monodisperse  $\text{Fe}_3\text{O}_4$  nanocubes and compared them to their spherical counterparts using cryo-TEM, XRD, SQUID and MRI relaxivity measurements. The study revealed that cubic iron oxide nanoparticles have a higher degree of relaxivity and crystallinity which promises high potential of nanocubes for magnetic resonance imaging.

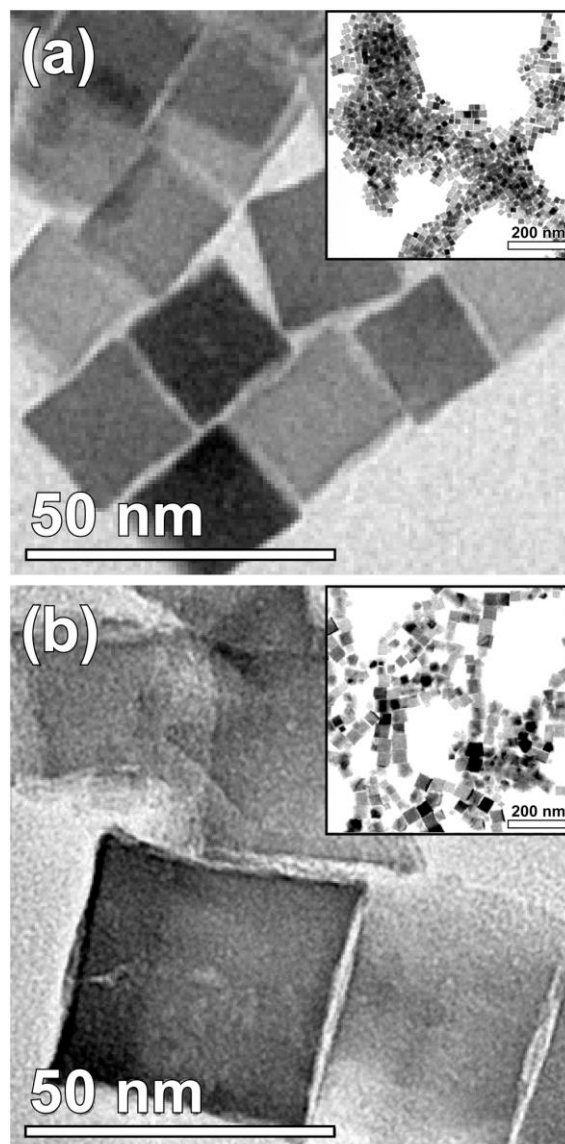


Figure 5: Iron-oxide nanocubes (a) with average edge length of 20.5 nm; inset reveals 2D self-assembly arrangements. (b) Corresponding TEM micrograph of 40 nm nanocubes: Observation of chain-like configurations [42]



#### **1.4.5.4 Nanorods**

Another approach with the aim of reaching maximum heating efficiency focusses on the investigation of nanorods. In 2016, Das et al. published a study concerning the tunable high aspect ratio of iron oxide nanorods for enhanced hyperthermia [40]. They demonstrated that the SAR of iron oxide nanostructures can be enhanced and tuned by altering their aspect ratio. The calorimetric and ac magnetometric experiments with an ac field of 800 Oe on highly crystalline Fe<sub>3</sub>O<sub>4</sub> nanorods performed by Das et al. showed large SAR values (862 W/g), higher than for their spherical (~140 W/g) and cubic (~314 W/g) counterparts of similar volume. An increase of the aspect ratio of the nanorods from 6 to 11 improved the SAR by 1.5 times. The investigated nanorods had an average height from 41 nm to 65 nm and an average width from 5.7 nm to 10 nm. Furthermore, Das et al. observed that the rapid parallel alignment of the nanorods by the applied ac field had positive effects on the SAR values.

The examples above clearly express that the optimization of the heating efficiency of magnetic nanoparticles in use for biomedical applications has not finished yet. Due to the fact that nanoparticles tend to accumulate in liver, kidneys and other parts of the body [44], further studies are necessary to reduce the amount of nanoparticles needed for a successful hyperthermia treatment to a number as low as possible.

## 2 Theoretical Background

### 2.1 Superparamagnetism

The effect of superparamagnetism in specific magnetic materials has already been described by C.P. Bean and J.D. Livingston in 1959 [45]. As a result of the rapid changes in magnetic data storage history and the development of nanotechnology this type of magnetism has become more relevant than ever.

Superparamagnetism is a type of magnetism that occurs in small ferromagnetic or ferrimagnetic nanoparticles. This implies sizes around a few nanometres to a couple of tenth nanometres, depending on the material. Additionally, these nanoparticles are single-domain particles. Without an external magnetic field, the net moment is zero. As soon as an external field is applied, the nanoparticles react similarly to a paramagnet with the one exception that their magnetic susceptibility is much larger.

Normally, any ferromagnetic or ferrimagnetic material can behave paramagnetically. This is from a certain temperature on and upwards, the so called Curie temperature  $T_C$ . However, superparamagnetic behaviour is observed below the Curie temperature and thus has to be explained differently. Characteristic for the superparamagnetic behaviour of a particle is the randomly flipping of the direction of its magnetization. This effect is induced only by thermal energy. Néel proposed that the relaxation time for such a spin flip is determined by the product of an attempt frequency  $\tau_0^{-1}$  and the Boltzmann probability  $e^{-\Delta E/k_B T}$  that the particle has the thermal energy necessary to surmount the barrier. The inverse spin-flip frequency is the relaxation time given by the Néel-Arrhenius-equation [46]:

$$\tau_N = \tau_0 * e^{\Delta E/k_B T} \quad (1)$$

Where the average length of time that it takes for the nanoparticle's magnetization to randomly flip as a result of thermal fluctuations is given by  $\tau_N$ .  $\tau_0$  represents the so called attempt time, which is a length of time characteristic of a material, typically between  $10^{-9}$  and  $10^{-11}$  seconds. The energy barrier associated with the magnetization moving from an easy initial state to an easy final state is given by  $\Delta E$ .  $K_B$  is the commonly known Boltzmann constant and  $T$  is the temperature. A widely used approximation for  $\Delta E$ , which shows the dependency of the energy barrier on the particle volume, is given by

$$\Delta E \cong K_1 V. \quad (2)$$

The relaxation time is of great interest for various applications such as the already mentioned magnetic hyperthermia treatment. Also for magnetic storage devices the so called superparamagnetic limit has to be overpowered to enable smaller storage devices with a reasonable period of time in which data does not get lost. To determine the relaxation time knowledge about the energy barrier between an initial state and a final state has to be given. This energy barrier can be calculated by computational simulations based on the nudged elastic band method. To perform this kind of simulations basic knowledge about the principles of micromagnetics and, building on those, the finite element method is essential.

## 2.2 Theory of Micromagnetism

### 2.2.1 Gibbs free energy

In micromagnetism the magnetic state is – at given temperature, applied field and elastic tension – fully described by the magnetic polarisation  $\mathbf{J}(\mathbf{r})$  or the magnetization  $\mathbf{M}(\mathbf{r})$ . The magnetic polarisation

$$\mathbf{J}(\mathbf{r}) = \mu_0 \mathbf{M}(\mathbf{r}) \quad (3)$$

is connected to the z-component  $S_Z$  of the Spin  $\mathbf{S}$  in the following way:

$$|\mathbf{J}(\mathbf{r})| = \mu_0 |\mathbf{M}(\mathbf{r})| = g \mu_B S_Z(\mathbf{r}) / \Omega(\mathbf{r}) \quad (4)$$

With Landé-factor  $g$ , the Bohr magneton  $\mu_B$  and  $\Omega(\mathbf{r})$  as the local atomic volume per magnetic ion. The local magnetic moment is given by  $\mu_B S_Z(\mathbf{r})$ . The primary task of micromagnetics is the determination of the polarisation vector  $\mathbf{J}(\mathbf{r})$ . The starting point therefore is represented by the Gibbs free energy with the quantities temperature  $T$ , elastic stress tensor  $\sigma$  and the external field  $H_{ext}$ . The energy density of the Gibbs free energy is given by:

$$\omega' = U - TS - \sigma * \varepsilon - \mathbf{J}_S * \mathbf{H}_{ext} \quad (5)$$

In formula (5),  $U$  describes the energy density of the inner energy,  $S$  represents entropy per unit volume,  $\sigma$  the strain tensor and  $\varepsilon$  the stress tensor. The free energy  $U - TS$  includes the following energy terms: exchange, anisotropy, dipolar and elastic energy terms. In the thermodynamic equilibrium a system shows a minimum in the total Gibbs free energy:

$$\delta \omega = \delta \int_V \omega' dV = 0 \quad (6)$$

where for constant  $T$ ,  $\sigma$  and  $\mathbf{H}_{ext}$  the variation is performed in respect to the internal magnetic variables of the system. Due to thermal activation the system is able to surmount an energy barrier and to go to another local energy minimum. In this diploma thesis the finite-element-method is used to calculate the energy for complex magnetic systems. Micromagnetism is based on continuum terms for the energy terms included in  $U$ . The static and dynamic magnetic properties of a system are determined by the relative contribution of the different magnetic energy terms to the free energy. The magnetic energy terms are exchange energy, magnetostatic energy, magnetic anisotropy and, in case an external field is applied, the Zeeman energy.

### 2.2.2 Exchange energy

The origin of magnetic order is exchange interaction. It is based on the Coulomb repulsion between two ions and the Pauli Exclusion Principle. Depending on the arrangement of the atoms the exchange energy leads to different spin arrangements such as ferromagnetism, antiferromagnetism or ferrimagnetism. The Pauli Exclusion Principle keeps two electrons

with parallel spin on distance to each other and therefore reduces the Coulomb repulsion. The difference between parallel and antiparallel spin setup is the exchange energy.

If all spins are aligned in a parallel way, the exchange energy is minimal. So, the state of uniform magnetization is most preferable for this energy term. Principally the exchange interaction is strong, but it shows only a short range.

In quantum mechanics exchange interaction is described by the Heisenberg Hamiltonian:

$$E_{exch} = -\sum_i \sum_{j \neq i} J_{ij} \mathbf{S}_i \mathbf{S}_j \quad (7)$$

$J_{ij}$  represents the exchange integral between the spins  $i$  and  $j$ .  $\mathbf{S}_i$  and  $\mathbf{S}_j$  are the spin operators. In micromagnetics the spin operators are replaced by classical vectors and only nearest neighbour interactions between the spins are regarded.

$$E_{exch} = -\sum_i \sum_{j \neq i} J_{ij} \mathbf{S}_i \mathbf{S}_j = -JS^2 \sum_{NN} \cos \phi_{ij} \quad (8)$$

Due to the fact that the exchange energy is very strong between nearest neighbour spins and because of the short range of this type of interaction, this approximation is justified.  $\phi_{ij}$  is the angle between the spins  $\mathbf{S}_i$  and  $\mathbf{S}_j$ . Only small angles between neighbored spins appear on short distances due to the strong exchange interactions. In continuum theory the exchange energy is approximated by a single, isotropic exchange stiffness constant  $A$ :

$$E_{exch} = A \int (\nabla * \mathbf{s})^2 dV \quad (9)$$

where  $\mathbf{s} = \mathbf{M}/M_s$ .

### 2.2.3 Anisotropy energy

In the theoretical model, the Heisenberg operator is isotropic and the energy is independent of the direction of the magnetization in the sample. Real magnetic materials are not isotropic and not all directions of magnetization are equally probable. There are different kinds of anisotropy such as magnetocrystalline anisotropy, surface anisotropy, shape anisotropy and magnetoelastic anisotropy. The most important of these is the magnetocrystalline anisotropy caused by spin-orbit-interaction which couples the spins to the crystal lattice. As a consequence, spins prefer to align in specific directions of the crystal. The magnetization in a ferromagnet positions itself in a preferred crystallographic direction, the so-called easy axis. The magnetocrystalline anisotropy is characterized by the anisotropy coefficients.

The simplest kind is uniaxial anisotropy. The anisotropy of a hexagonal crystal only shows dependence of the angle between the magnetization and the easy direction and can be expressed as a Taylor-series:

$$E_{ani} = K_0 V + K_1 V \sin^2 \phi + K_2 V \sin^4 \phi + \dots \quad (10)$$

The type of anisotropy for a material is dependent of the sign of  $K_1$  and  $K_2$ . If both constants are positive the magnetic system has an easy axis. In the case of two negative signs the system

has an easy plane. If the signs are mixed, the ratio between  $K_1$  and  $K_2$  decides, whether the anisotropy is of type easy axis, easy plane or easy cone (figure 6).

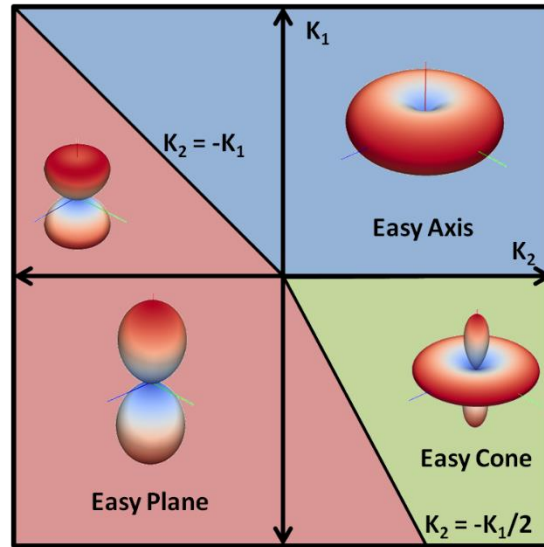


Figure 6: Anisotropy type depending on the uniaxial constants  $K_1$  and  $K_2$  [47]

Another important – and for this diploma thesis relevant – type of magnetocrystalline anisotropy is cubic anisotropy. This type is described by a different approach:

$$E_{ani} = K_1 V (s_x^2 s_y^2 + s_y^2 s_z^2 + s_x^2 s_z^2) + K_2 V s_x^2 s_y^2 s_z^2 \quad (11)$$

where  $s_x, s_y, s_z$  are the direction cosines of the normalized magnetization direction. The dependency on the signs of  $K_1$  and  $K_2$  is shown in figure 7:

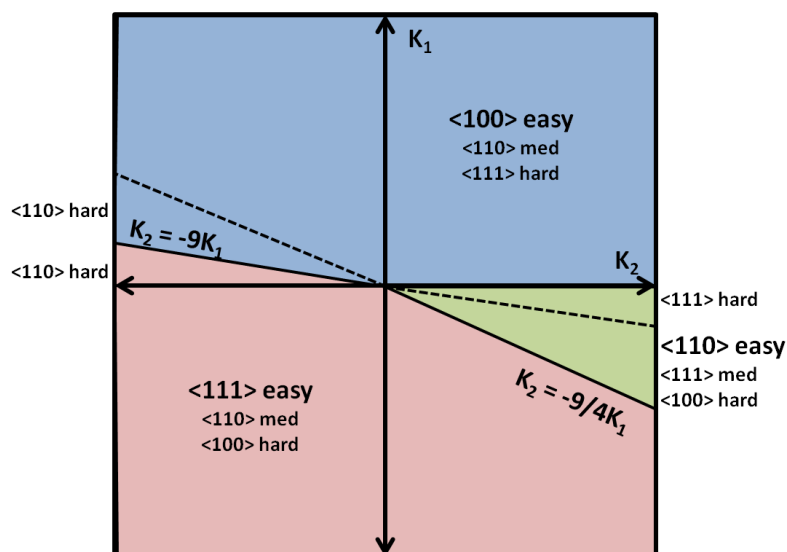


Figure 7: Easy, intermediate and hard axes in dependence on the cubic anisotropy constants  $K_1$  and  $K_2$  [47]

## 2.2.4 Magnetostatic Self-Interaction

The magnetostatic self-interaction energy describes the interaction between magnetic dipoles. It shows long range character and is responsible for the existence of magnetic domains. The corresponding energy term can be written as:

$$E_{ms} = -\frac{\mu_0}{2} \int \mathbf{H}_d \mathbf{M} dV = -\frac{1}{2} \int \mathbf{J} \mathbf{H}_d dV \quad (12)$$

If a particle is divided into domains, also the other energy terms of the Gibbs free energy have to be taken into account. The exchange interaction prefers, as mentioned, a parallel alignment of spins. But if there are two domains with a grain boundary in between, the spins are antiparallel. This means a loss of exchange energy, which is higher than the gain of magnetostatic energy. In contrast to exchange interaction, the magnetostatic self-interaction has a long range.

## 2.2.5 Zeeman Energy

The Zeeman energy describes the interaction of a magnetic moment with an external field. If the moment is aligned parallel to the external field, the Zeeman energy is minimal. The Zeeman energy term is given by:

$$E_Z = -\mu_0 \int \mathbf{H}_{ext} \mathbf{M} dV = - \int \mathbf{J} \mathbf{H}_{ext} dV \quad (13)$$

## 2.2.6 Energy Minimization

Including the discussed energy terms above, the total magnetic Gibbs free energy is given by:

$$E_{tot} = E_{exch} + E_{ani} + E_{ms} + E_Z \quad (14)$$

with the exchange energy  $E_{exch}$ , the magnetic anisotropy  $E_{ani}$ , the magnetoelastic self-interaction  $E_{ms}$  and the Zeeman energy  $E_Z$ . The minimization of the total Gibbs free energy leads to the static micromagnetic equilibrium conditions, which can be written as torque equations:

$$\mathbf{L} = [\mathbf{J} \times \mathbf{H}_{eff}] = 0 \quad (15)$$

In an equilibrium the torque on the direction of the magnetization has to be zero for each  $\mathbf{r}$ . The effective field  $\mathbf{H}_{eff}$  includes the exchange field  $\mathbf{H}_{exch}$ , the anisotropy field  $\mathbf{H}_{ani}$ , the demagnetizing field  $\mathbf{H}_D$  and the external field  $\mathbf{H}_{ext}$ :

$$\mathbf{H}_{eff} = \mathbf{H}_{exch} + \mathbf{H}_{ani} + \mathbf{H}_D + \mathbf{H}_{ext} \quad (16)$$

The effective field  $\mathbf{H}_{eff}$  can be obtained by performing the negative functional derivation of the energy density  $\omega$ :

$$\mathbf{H}_{eff} = -\frac{\delta \omega}{\delta \mathbf{J}} \quad (17)$$

The classical equation of motion which connects a magnetic moment with a mechanical angular momentum is given by:

$$\frac{d\mathbf{L}}{dt} = \mathbf{D} = \boldsymbol{\mu} \times \mathbf{B} \quad (18)$$

In respect to the relation  $\boldsymbol{\mu} = \gamma\mathbf{L}$  it changes to:

$$\frac{d\boldsymbol{\mu}}{dt} = \gamma \cdot \boldsymbol{\mu} \times \mathbf{B} \quad (19)$$

This relation describes a precession of the magnetic moment. In micromagnetics the magnetic moment is replaced by the magnetization, which symbolizes the undamped precession of the magnetization around the effective field. Due to the relation between the magnetization  $\mathbf{M}$  and the polarization  $\mathbf{J}$  given in (3), the precession term can be written as:

$$\frac{d\mathbf{J}}{dt} = -\gamma(\mathbf{J} \times \mathbf{H}_{eff}) \quad (20)$$

Landau, Lifshitz and Gilbert have modified the equation by a damping term, which results in the Landau-Lifshitz-Gilbert equation ([48], [49]):

$$\frac{d\mathbf{J}}{dt} = -\gamma \cdot (\mathbf{J} \times \mathbf{H}_{eff}) - \gamma \frac{\alpha}{J_s} \cdot \mathbf{J} \times (\mathbf{J} \times \mathbf{H}_{eff}) \quad (21)$$

Where  $\gamma$  is the gyromagnetic ratio and  $\alpha$  is a dimensionless constant called the damping factor. Figure 8 illustrates the damped precession of the magnetization around the effective field.

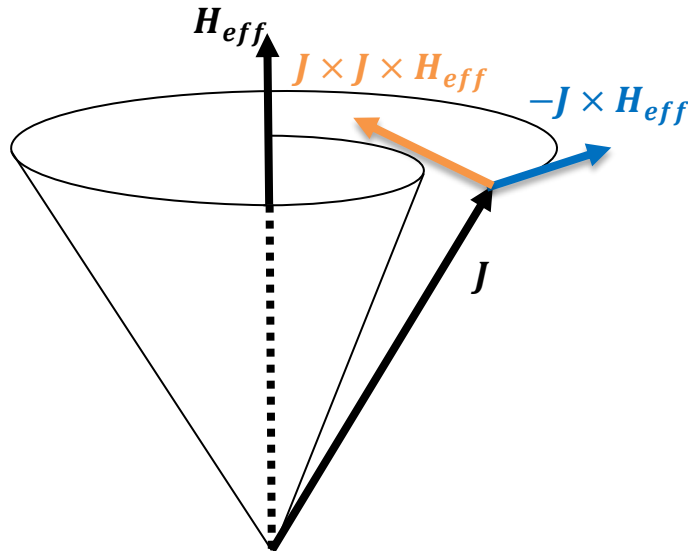


Figure 8: Damped magnetization precession

The solution of the Landau-Lifshitz-Gilbert-equation (LLG) will present the basis for later performed micromagnetic simulations.

### 2.3 The Stoner-Wohlfarth Model

The Stoner-Wohlfarth model [50] is a simple but helpful model of magnetization reversal which assumes a coherent way of magnetization reversal. In the limit of very small particles this model is able to reproduce the exact micromagnetic behaviour. The basic hypothesis of the Stoner-Wohlfarth model is a constant magnetization throughout the magnet. Consequently, during magnetization reversal the exchange energy does not change and the coercivity is equal to the anisotropy field.

The initial point of the model is the Stoner-Wohlfarth particle, a uniformly magnetized rotational ellipsoid with uniaxial anisotropy in a field applied at an angle  $\alpha$  to the anisotropy axis (figure 9).

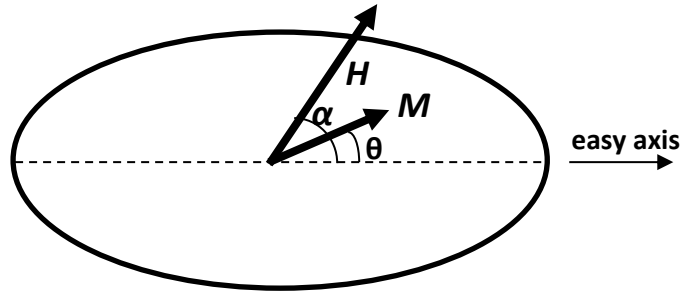


Figure 9: Stoner-Wohlfarth particle (rotational ellipsoid)

The energy density is given by

$$E_{tot} = K_u \sin^2 \theta - \mu_0 M H \cos(\alpha - \theta) \quad (22)$$

with  $K_u$  as the sum of magnetocrystalline anisotropy  $K_1$  and shape anisotropy  $K_{sh} = \frac{1}{2} \mu_0 M_S^2 (N_x - N_z)$ ,  $\mu_0$  as the vacuum permeability,  $M$  as the magnetization and  $H$  as the external field,  $\alpha$  as the angle between the anisotropy axis and the applied field  $H$  and  $\theta$  as the angle between the anisotropy axis and the magnetization  $M$ . The demagnetizing factor  $N$  is given by a 3x3 tensor with the diagonal elements  $N_x$ ,  $N_y$ ,  $N_z$ . These fulfil the following equation:

$$N_x + N_y + N_z = 1 \quad (23)$$

In case of a rotational ellipsoid only two of the three components are independent:

$$N_x = N_y = N_{\perp}, \quad N_z = N_{\parallel} \quad (24)$$



With the relations (23) and (24) the shape anisotropy  $K_{sh}$  can be given as:

$$\begin{aligned}
 K_{sh} &= \frac{\mu_0}{2} M_s^2 (N_x - N_z) \\
 &= \frac{\mu_0}{2} M_s^2 \left( \frac{1 - N_z}{2} - N_z \right) \\
 &= \frac{\mu_0}{2} M_s^2 \left( \frac{1 - 3N_z}{2} \right) \\
 &= \frac{\mu_0}{4} M_s^2 (1 - 3N_z)
 \end{aligned} \tag{25}$$

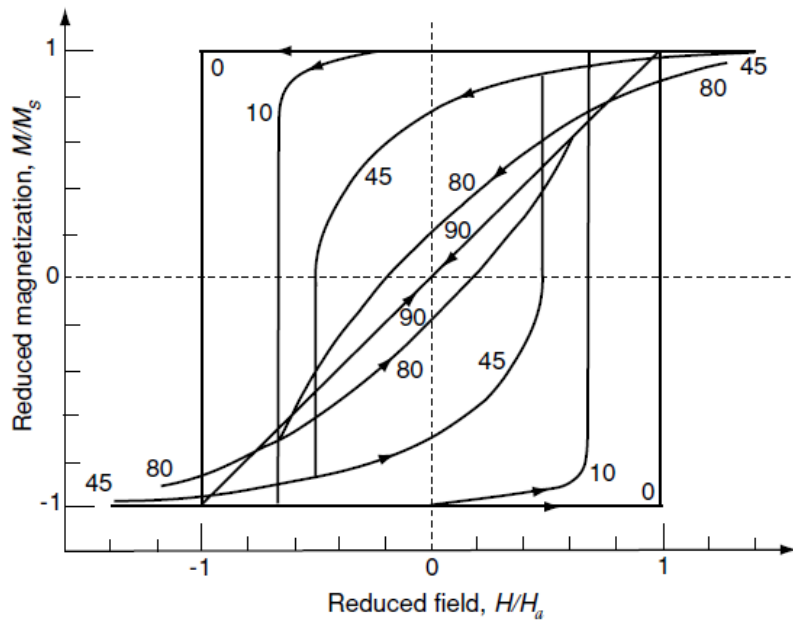


Figure 10: Magnetization curves for the Stoner-Wohlfarth model for various angles  $\alpha$  between the field direction and the easy axis [50]

Varying the angle  $\alpha$  between the direction of the external field and the anisotropy axis influences the shape of the hysteresis curve (figure 10). Applying the external field aligned to the anisotropy axis, delivers the case of a square hysteresis curve. The other extreme, the external field applied  $90^\circ$  to the anisotropy axis, generates a line without hysteresis area. If  $\alpha$  equals zero, the coercivity is equal to the anisotropy field  $H_c = 2K_u/\mu_0 M_s$ :

$$H_c = (2K_1/\mu_0 M_s) + [(1 - 3N_z)/2]M_s \tag{26}$$

## 2.4 Numerical Finite Element Micromagnetism

To solve the Landau-Lifshitz-Gilbert-equation (LLG) and therefore gain information about the magnetic properties of a sample, the method of finite elements is used in computational physics. In our case, a sample is discretized using finite elements, tetrahedrons. The simulation programme “FEMME” [51] then solves the LLG-equation in every nod of the tetrahedrons, which means that the pointing direction of a magnetic moment in a nod is known after the calculation.

### 2.4.1 Hysteresis Loop Modelling (Magnetic Field Reversal)

In a first step the geometry of interest is designed using the visualization program GID (version 12.0.7) [52] which also enables to assign a material to the drawn geometry. The designed geometries include Fe-spheres, Fe<sub>3</sub>O<sub>4</sub>-spheres, Fe<sub>3</sub>O<sub>4</sub>-discs and Fe<sub>20</sub>Ni<sub>80</sub> discs. Finally, to apply the finite element method by filling up the geometry with tetrahedrons, so called meshing. The size of the tetrahedrons depends on the exchange length ([53],[54]) of a material which can be determined by

$$l_{ex} = \min \left( \sqrt{\frac{A}{K_1}}, \sqrt{\frac{A}{(J_s^2/\mu_0)}} \right), \quad (27)$$

containing exchange constant  $A$ , magnetocrystalline anisotropy constant  $K_1$ , magnetization polarisation  $J_s$  and vacuum permeability  $\mu_0$ . For the choice of an appropriate mesh size the exchange length  $l_{ex}$  serves as an upper limit. Figure 11 illustrates a shape drawn with GID before and after meshing.

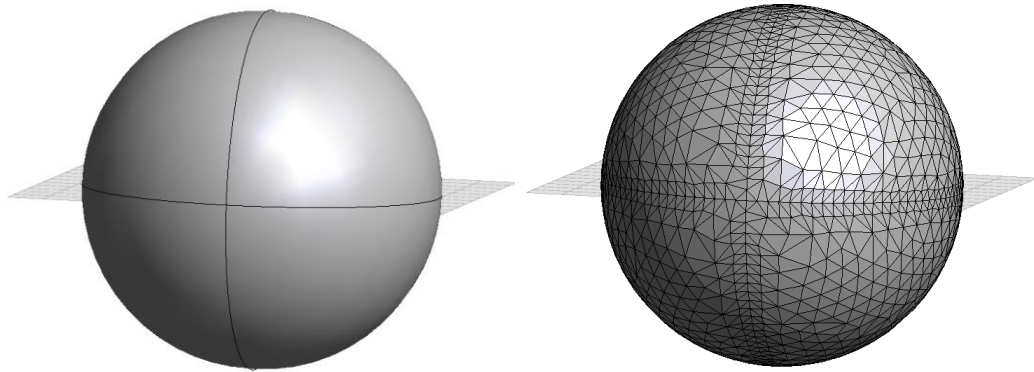


Figure 11: Sphere with a diameter of 25 nm before (left) and after meshing (right) in GID

The used material parameters for Fe, Fe<sub>3</sub>O<sub>4</sub> and Fe<sub>20</sub>Ni<sub>80</sub> are given in table 1. The calculated exchange lengths according to formula (27) are given in table 2.

<i>Parameter</i>	<i>Fe [55]</i>	<i>Fe<sub>3</sub>O<sub>4</sub> [56]</i>	<i>Fe<sub>20</sub>Ni<sub>80</sub> [57]</i>
<i>A [pJm<sup>-1</sup>]</i>	25	7	10
<i>J<sub>s</sub> [T]</i>	2.15	0.6	1.0
<i>K<sub>1</sub> [kJm<sup>-3</sup>]</i>	46	-13	0
<i>K<sub>2</sub> [kJm<sup>-3</sup>]</i>	15	-1	0

Table 1: material parameters of Fe, Fe<sub>3</sub>O<sub>4</sub> and Fe<sub>20</sub>Ni<sub>80</sub> used for the numerical micromagnetic simulations

<i>Material</i>	$\sqrt{\frac{A}{K_1}}$	$\sqrt{\frac{A}{(J_s^2/\mu_0)}}$
<i>Fe</i>	23.31 nm	2.61 nm
<i>Fe<sub>3</sub>O<sub>4</sub></i>	23.20 nm	4.94 nm
<i>Fe<sub>20</sub>Ni<sub>80</sub></i>	-	3.41 nm

Table 2: Calculated exchange lengths for the three simulated materials Fe, Fe<sub>3</sub>O<sub>4</sub> and Fe<sub>20</sub>Ni<sub>80</sub>

To make out the mesh sizes as small as necessary, but as big as possible, for a correct calculation of the magnetization reversal process, different mesh sizes have been tested to control the stability of the coercivity  $H_c$ . If  $H_c$  does not vary, the mesh size is small enough to deliver accurate simulation results. The charts below (figure 12) illustrate the received coercivity  $H_c$  simulated with different mesh sizes.

Due to the fact that the spheres were only drawn once at a diameter of D=100 nm and then scaled down to the smaller diameters, only the D=100 nm sphere is shown. In the case of the discs, which were not scaled down, the graphs show the discs with the smallest geometry size/mesh size ratio. If these discs show a stable value for the coercivity  $H_c$ , the mesh size is also appropriate for larger geometries. The constancy on three decimal places was taken as measure for a sufficiently small mesh size. The graphs show that with smaller mesh sizes the value for the coercivity  $H_c$  levels off. In respect to these results, appropriate mesh sizes were chosen for the numerical simulations.

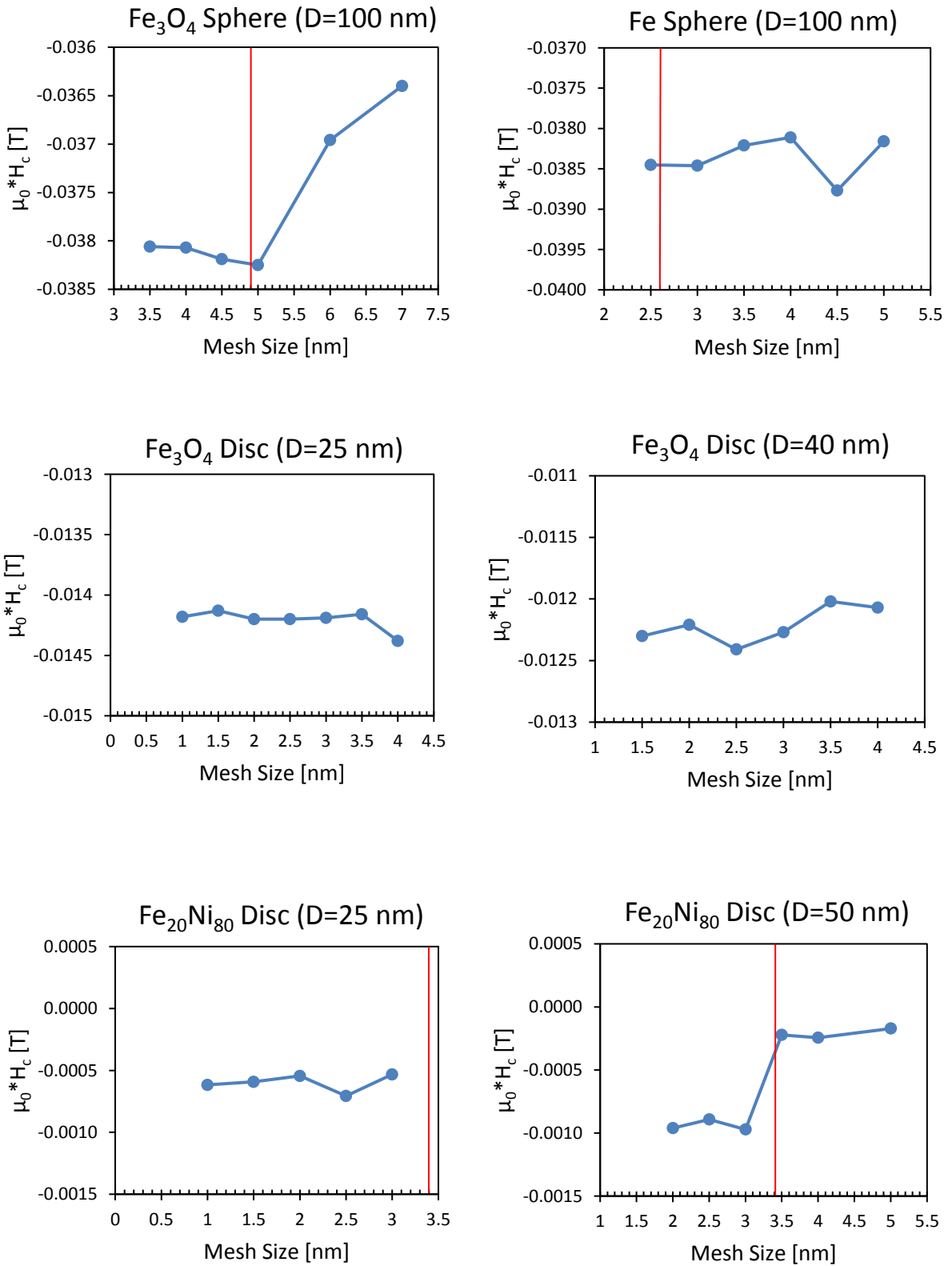


Figure 12: values for the coercivity  $H_c$  delivered from numerical simulations at different mesh sizes; the smaller the mesh size the more accurate and stable the result for the coercivity  $H_c$ . The red lines mark the calculated values (documented in table 2) serving as an upper limit for the mesh sizes used for the micromagnetic simulations.

The applied mesh sizes for the simulated geometries are documented in table 3. The designed spheres were drawn with a diameter of  $D = 100$  nm and meshed at this size with a mesh size of 3.5 nm for  $Fe_3O_4$  and 2.5 nm for Fe. This geometry was then scaled down directly in the simulation file “master.par” to simulate smaller spheres which do all have the same ratio between size and mesh size.

<i>Discs</i>			
	<b>height [nm]</b>	<b>diameter [nm]</b>	<b>mesh size [nm]</b>
<i>Fe<sub>20</sub>Ni<sub>80</sub></i>	12	25	1
	12	50	2
	12	100	2
	12	200	2
<i>Fe<sub>3</sub>O<sub>4</sub></i>	12	25	2
	12	40	3
	12	50	3
	12	60	3
	12	80	3
	12	100	3
	12	200	3
<i>Spheres</i>			
	<b>diameter [nm]</b>	<b>mesh size [nm]</b>	
<i>Fe<sub>3</sub>O<sub>4</sub></i>	100	3.5	(scaled down)
<i>Fe</i>	100	2.5	(scaled down)

Table 3: mesh sizes for the simulated geometries; the spheres were drawn with a diameter of 100 nm and scaled down to smaller diameters

After the designing and meshing process, the data received from GID finds its application in the simulation software FEMME. An overview of the output of GID is given in table 4.

<i>file type</i>	<i>delivered information</i>
<i>.inf</i>	number of nodes, volume and surface elements
<i>.knt</i>	cartesian coordinates of the nodes
<i>.ijb</i>	list of surface triangles
<i>.ijk</i>	list of surface tetrahedrons
<i>.ijl</i>	list of line elements
<i>.gbe</i>	intergranular exchange
<i>.ini</i>	initial magnetization
<i>.krn</i>	material parameters

Table 4: output from GID; information of the finite element grid

With the received data from GID and the two files master.par and femme-run.sh all information and tools necessary for a simulation are provided. The file master.par contains information about the writing interval, the stray field and the direction of the external field. To ensure that the direction of the anisotropy constant  $K_2$  cannot vary during the simulation the command "name\_K2 = AXIS" has been set. Another important tool is the command "name\_size = 0.5e-9" which enables to scale a geometry up or down including its mesh grid. This function ensures a stable ratio between the size of the mesh grid and the geometry size. In the example given a designed geometry is scaled down to half of its initial size. A segment of a master.par file for magnetization reversal caused by an external field is given in figure 13. The femme-run.sh file is necessary to start the numerical simulation.

```

ProblemName = name_skal
InitialTime = 0.0e-9
TimeInterval = 0.2e-9
TimeIntervalInp = 3e-9
FinalTime = 30e-9
name_skal_ini = 0
name_K2 = AXIS
name_size = 0.5e-9
name_alpha = 1.0
HextON = 1
alpharot = 0.1
betarot = 0.1
gammarot = 0.1
> 0      0.0  0.0  1.5      0      1      20      1000
> 300    0.0  0.0  -1.5
> 600    0.0  0.0  1.5
name_hmag = ON

```

*Figure 13: Cut-out of a master.par file for field magnetization reversal performed by FEMME*

The program FEMME simulates a complete magnetization reversal caused by an external field, from an initial magnetization state with all moments parallel aligned, to a final magnetization state with the magnetic moments in the exact opposite direction and finally, back to the initial state. During this micromagnetic simulation FEMME delivers data containing the x-, y- and z-components of the external field and of the magnetization inside the geometry in predefined time steps. This data contains all information needed to visualize the hysteresis curve of the object which was realized with OriginPro (8.6G 64Bit). In addition, the program produces .inp-files in specific time intervals which can be used to animate the magnetization reversal process with the image processing program ParaView (version 4.2.0) [58]. A hysteresis curve which can be received from the micromagnetic simulation is presented exemplarily in figure 14. The visualizations of the two minimum energy states of the hysteresis curve **A** and **B** are given below. To highlight the parallel alignment of all vectors, the spheres were cut in half.

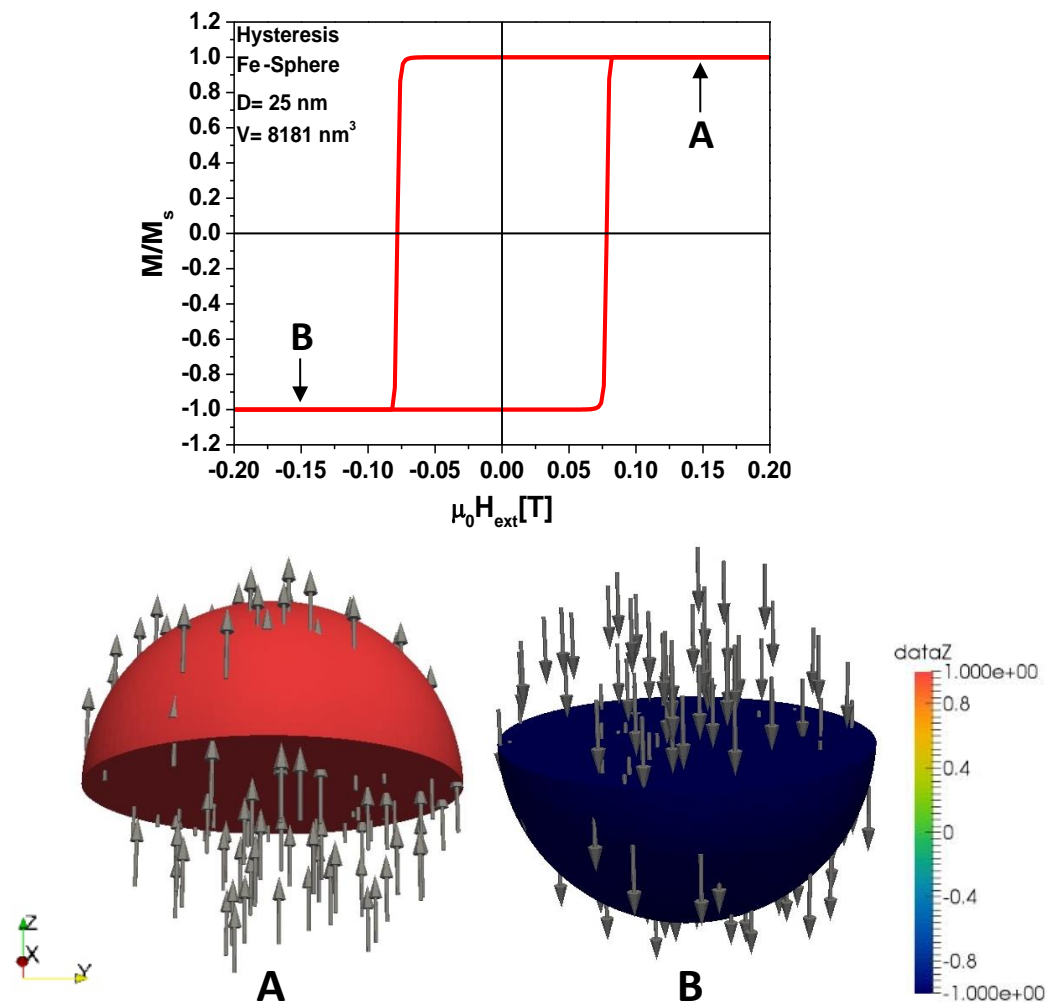


Figure 14: Exemplary hysteresis curve of a Fe-Sphere with a diameter of 25 nm and the visualization of two minimum energy states A and B

## 2.4.2 Thermal Magnetization Reversal (Nudged Elastic Band Method)

Next to the magnetization reversal caused by an external field, the simulation tool FEMME offers the possibility to simulate the magnetization reversal of a geometry only caused by thermal fluctuations. This type of simulation enables to investigate the stability of a magnetic state without any influences from external fields. To calculate the lifetime of a magnetic state and, in consequence, to determine the critical volumes of particles regarding superparamagnetic behaviour, it is necessary to have knowledge about the energy barrier between two energy minima. Therefore, the nudged elastic band method is a promising tool ([59], [60], [61]):

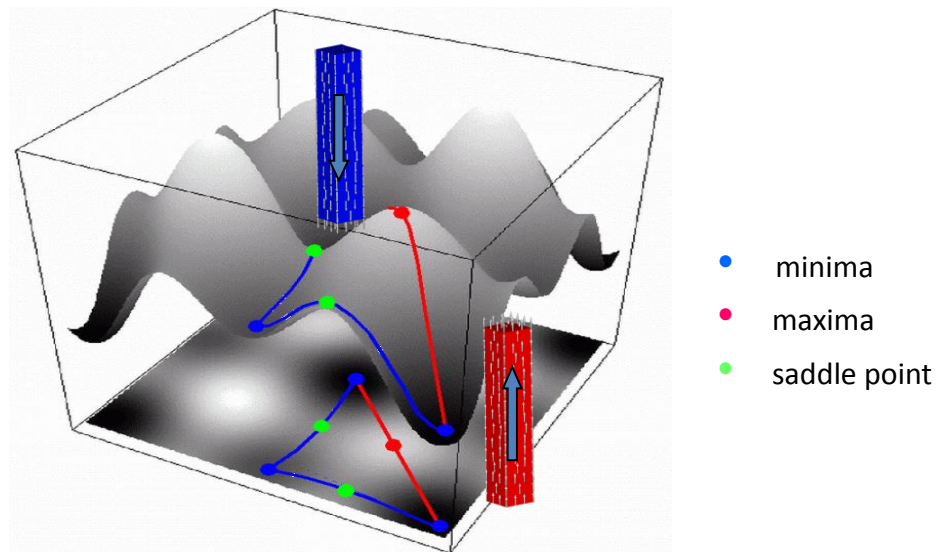


Figure 15: Visualization of the basic idea of the nudged elastic band method

The starting point is a guessed path connecting two energy minima. The two energy minima are provided by previous magnetization field reversal simulations. These two states are characterized by the fact that all magnetic moments are aligned in the same direction. Then, the programme is searching for the most probable path by moving the points on a path following an algorithm, which models the tension of an elastic band around a mountain. The optimum path can be found by an iterative process. In each iteration step the states are moved parallel to the negative energy gradient and vertically to the path. An optimization algorithm causes the energy gradient to point only in the direction of the path. The simulation delivers the relevant data in form of .log file which contains the received path called minimum energy path (MEP). The knowledge about the height of the energy barrier is the central aim of this simulation. This result enables the calculation of the lifetime of a magnetic state by utilizing the Néel-Arrhenius-equation (1) and, consequently, allows the formulation of a statement about the size at which nanoparticles can be declared as superparamagnetic.



### 3 Results of Micromagnetic Simulations of Fe-, Fe<sub>3</sub>O<sub>4</sub>- and Fe<sub>20</sub>Ni<sub>80</sub>-Nanoparticles

In order to determine the critical diameter or volume for the transition to superparamagnetic behaviour of a geometry, the maximum lifetime for a superparamagnetic state has to be defined. In this diploma thesis a time of 100 seconds was chosen which approximately matches the time required to measure the remanence of a nanoparticle with a vibrating sample magnetometer (VSM) ([45],[62]). Regarding formula (1),

$$\tau_N = \tau_0 * e^{\Delta E/k_B T}, \quad (1)$$

a lifetime of 100 seconds means an energy barrier for the transition from superparamagnetic to thermally stable behaviour of

$$\Delta E = \ln(\tau_N * \tau_0^{-1}) k_B T = 25 k_B T. \quad (28)$$

To guarantee the validity of the Néel-Arrhenius-equation (1) it is necessary to verify that the transition from one stable state to another is only performed by coherent switching of magnetization. This means that the Néel-Arrhenius equation is only valid if no incoherent behaviour is observed during the switching process of magnetization. In order to check the switching behaviour both magnetic field reversal and thermal reversal have been investigated for each object.

#### 3.1 Superparamagnetic Transitions of Fe<sub>3</sub>O<sub>4</sub>-Spheres

As discussed in chapter 1.4.4 magnetite in form of nanospheres presents the most commonly used material for biomedical applications such as magnetic hyperthermia. Therefore, it seems self-evident to investigate Fe<sub>3</sub>O<sub>4</sub> nanospheres in order to get a better understanding of the magnetization reversal processes which play a decisive part in magnetic hyperthermia treatments because of their role in heat generation. Various numerical, micromagnetic simulations of magnetite spheres with different diameters have been performed using the model in figure 16 and the dimensions in table 5. The simulations were executed according to the procedure described in chapter 2.4.

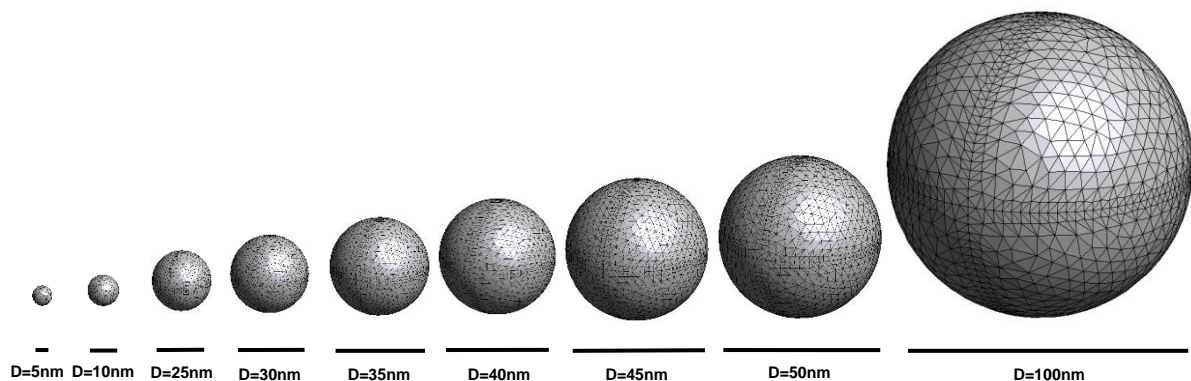


Figure 16: Models of simulated magnetite nanospheres ranging from diameter  $D=5\text{nm}$  up to  $D=100\text{nm}$  (designed with GID); the mesh size was scaled down from  $D=100\text{nm}$  with the geometry size

<i>Diameter</i> [nm]	<i>Volume</i> [nm <sup>3</sup> ]
5	65
10	524
25	8181
30	14137
35	22449
40	33510
45	47713
50	65450
100	523599

Table 5: diameters and correlating volumes of the simulated magnetite nanospheres

First of all, the switching behaviour of the nanospheres caused by an external field are regarded. Therefore, a complete reversal from the [111] direction to the [-1-1-1] direction and back to the [111] direction has been performed for all sizes of Fe<sub>3</sub>O<sub>4</sub> nanospheres. This magnetization reversal can be seen for nanospheres with a diameter of D=50 nm and D=100 nm in figure 17 and 18. Illustrating different steps of the reversal process graphically reveals incoherent switching behaviour which is expressed by vortex formation. The nanosphere with a diameter of D=50 nm shows coherent switching behaviour which is a first step towards the validation of the Néel-Arrhenius-equation (1). However, the D=100 nm nanosphere obviously executes the magnetization reversal by vortex nucleation.

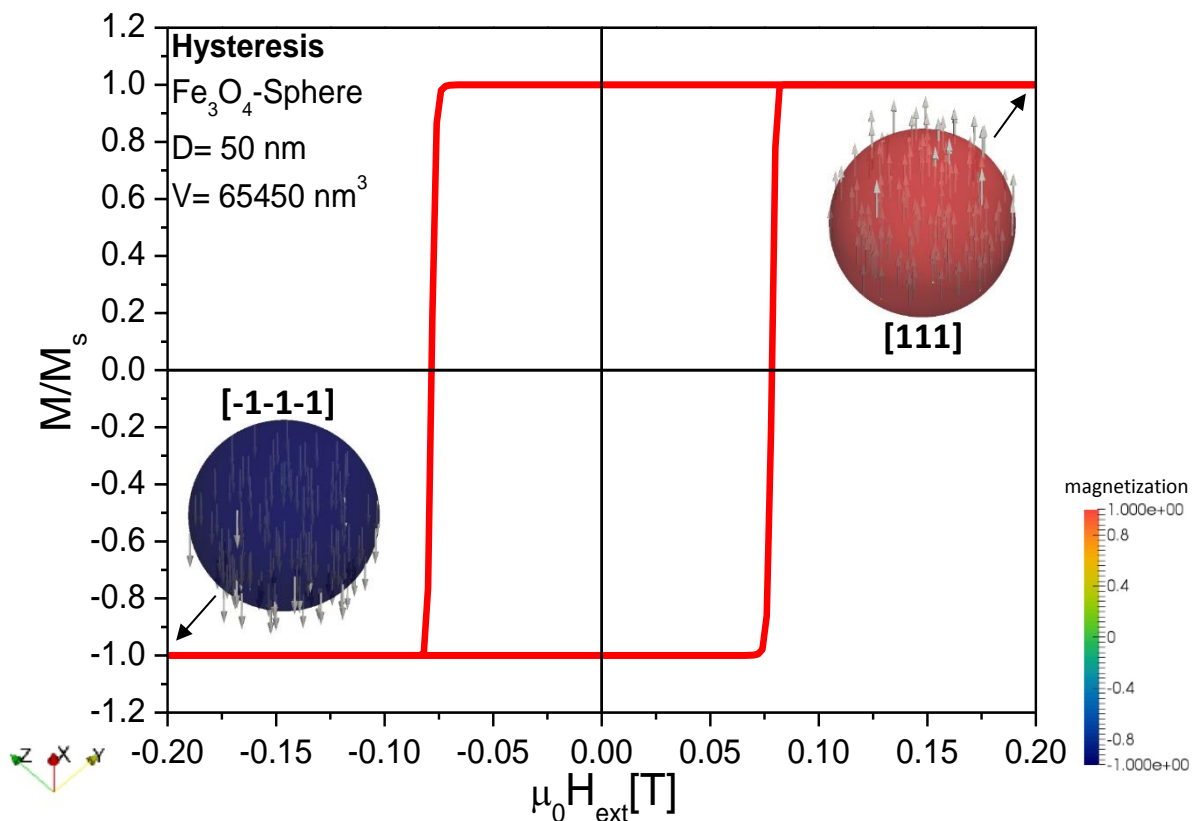


Figure 17: field magnetization reversal from the [111] to the [-1-1-1] direction of a Fe<sub>3</sub>O<sub>4</sub> nanosphere with D=50 nm; coherent switching behaviour

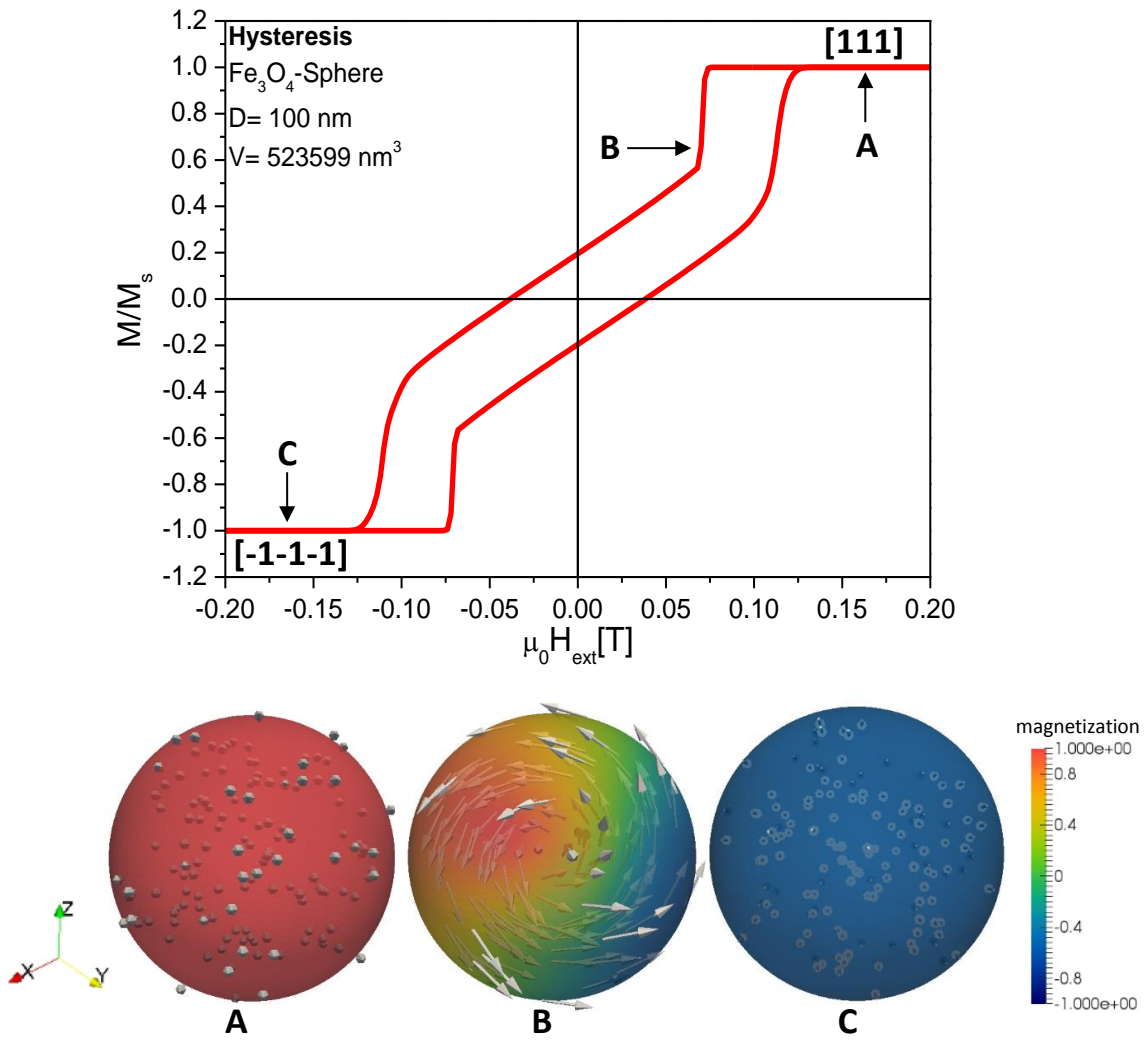


Figure 18: field magnetization reversal from the  $[111]$  to the  $[\bar{1}\bar{1}\bar{1}]$  direction of a  $\text{Fe}_3\text{O}_4$  nanosphere with  $D=100 \text{ nm}$ ; incoherent switching behaviour

The magnetization reversals caused by thermal fluctuations were performed from one easy direction of the crystal structure to a neighbouring easy direction. As mentioned in chapter 1.4.4.1, Fe<sub>3</sub>O<sub>4</sub> shows a spinel type structure with six easy directions corresponding to the three <111> axes with minimum anisotropy energy. Table 6 illustrates the easy direction combinations investigated by numerical simulations. The fourth combination means a complete reversal process from the [111] direction to the opposite [-1-1-1] direction which is relevant for magnetic hyperthermia treatments.

Initial easy direction	Final easy direction
[111]	[-111]
[-111]	[-11-1]
[-11-1]	[-1-1-1]
[111]	[-1-1-1]

Table 6: Simulated energy paths from one easy direction to another easy direction of Fe<sub>3</sub>O<sub>4</sub>

Regarding the minimum energy paths (MEPs) from the [111] to the [-111] direction for the nanospheres with D=50 nm and D=100 nm shows a coherence behaviour similar to the field reversal process. The particle with D=50 nm still shows coherent switching behaviour without any vortex formation (figure 19) and the larger nanosphere with D=100 nm already shows incoherence in magnetization reversal (figure 20). According to these results the validity of the Néel-Arrhenius-equation for the calculation of the limit to superparamagnetic behaviour is ensured for Fe<sub>3</sub>O<sub>4</sub> nanospheres with a diameter up to D=50 nm.

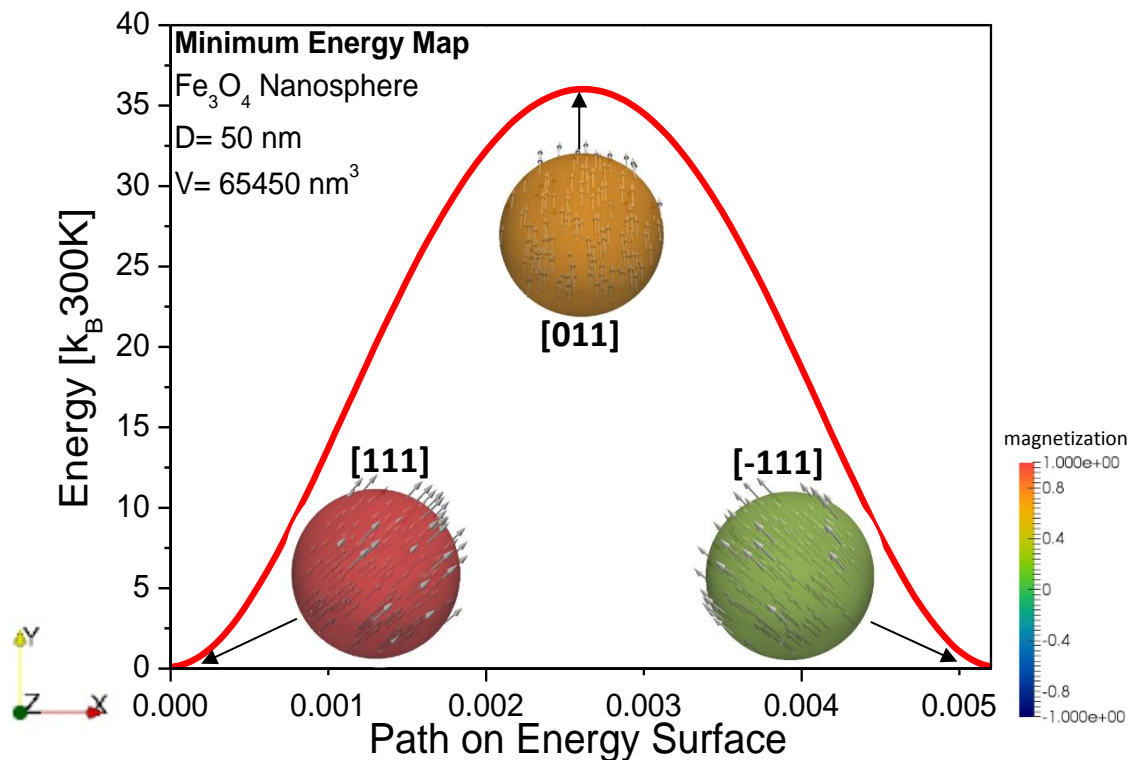


Figure 19: thermal magnetization reversal of the D=50 nm Fe<sub>3</sub>O<sub>4</sub> nanosphere from the [111] to the [-111] direction showing only coherent switching behaviour

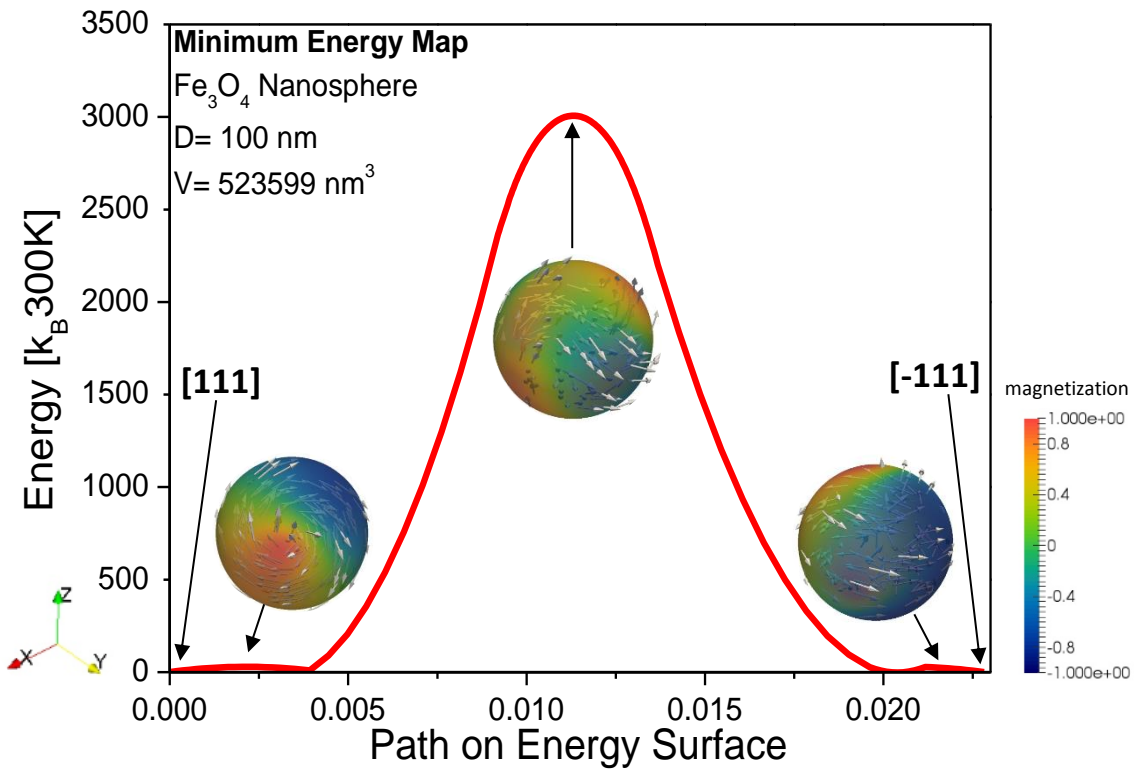


Figure 20: thermal magnetization reversal of the  $D=100 \text{ nm}$   $\text{Fe}_3\text{O}_4$  nanosphere from the [111] to the [-111] direction showing vortex formation

Exemplarily, the minimum energy maps (MEPs) for the energy path from the [111]-direction to the [-111]-direction are given in figure 21 for eight of nine simulated spheres. Due to the incoherent switching behaviour, and consequently invalidity of the Néel-Arrhenius-equation, of the largest nanosphere with  $D=100 \text{ nm}$ , this geometry is not considered for the determination of the superparamagnetic transition limit.

As the graphs in figure 21 clearly show, the energy barrier, given on the y-axis, rises with growing diameter of the particular nanosphere. The relation between particle diameter or particle volume and energy barrier is illustrated in figure 22 for all simulated easy direction combinations. These graphs enable the determination of the critical diameters/volumes for the transition from ferromagnetic to superparamagnetic behaviour.

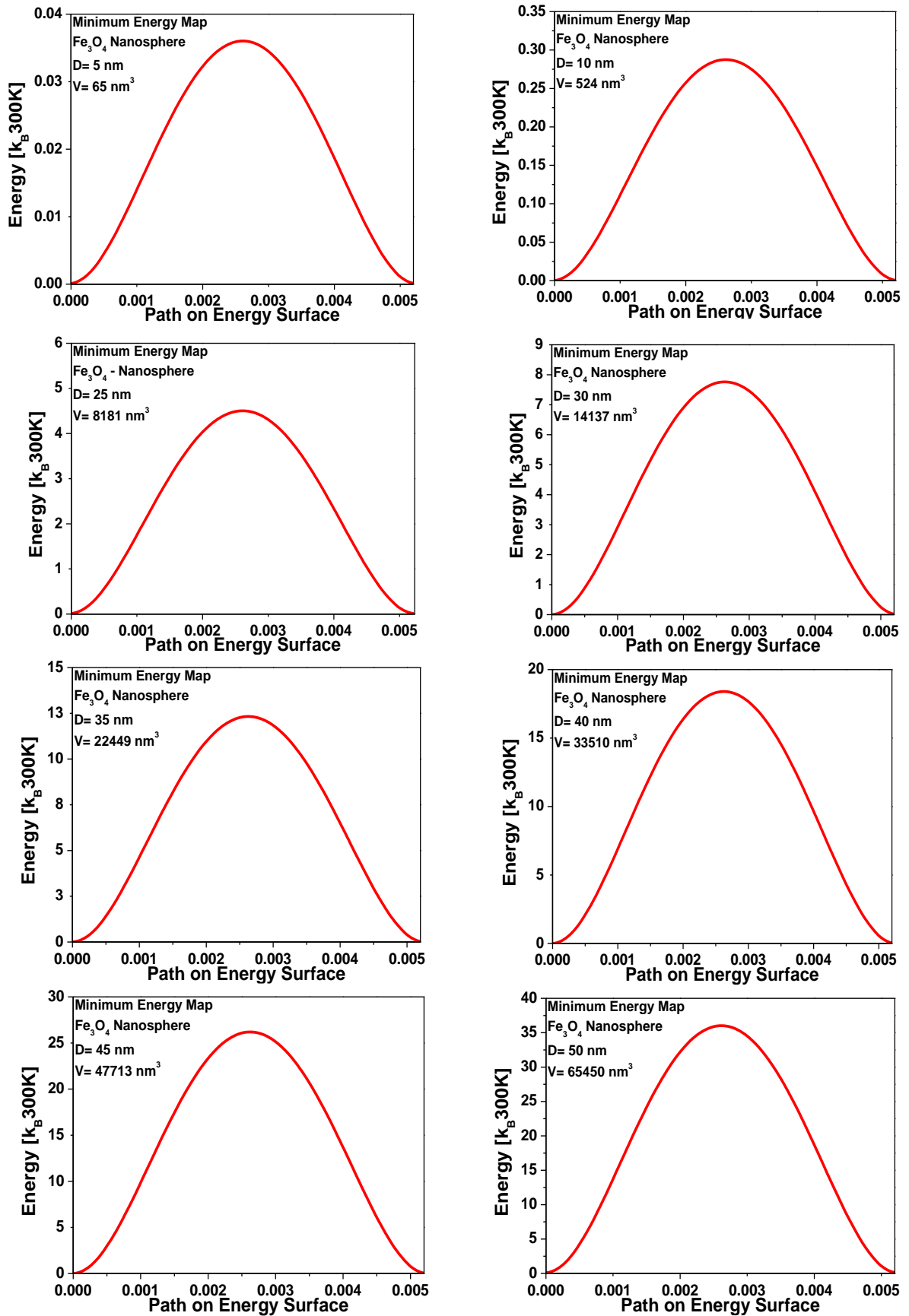


Figure 21: MEPs for the transition from the  $[111]$  to the  $[-1\bar{1}1]$  direction of  $\text{Fe}_3\text{O}_4$ ; the images are arranged according to rising diameter/volume

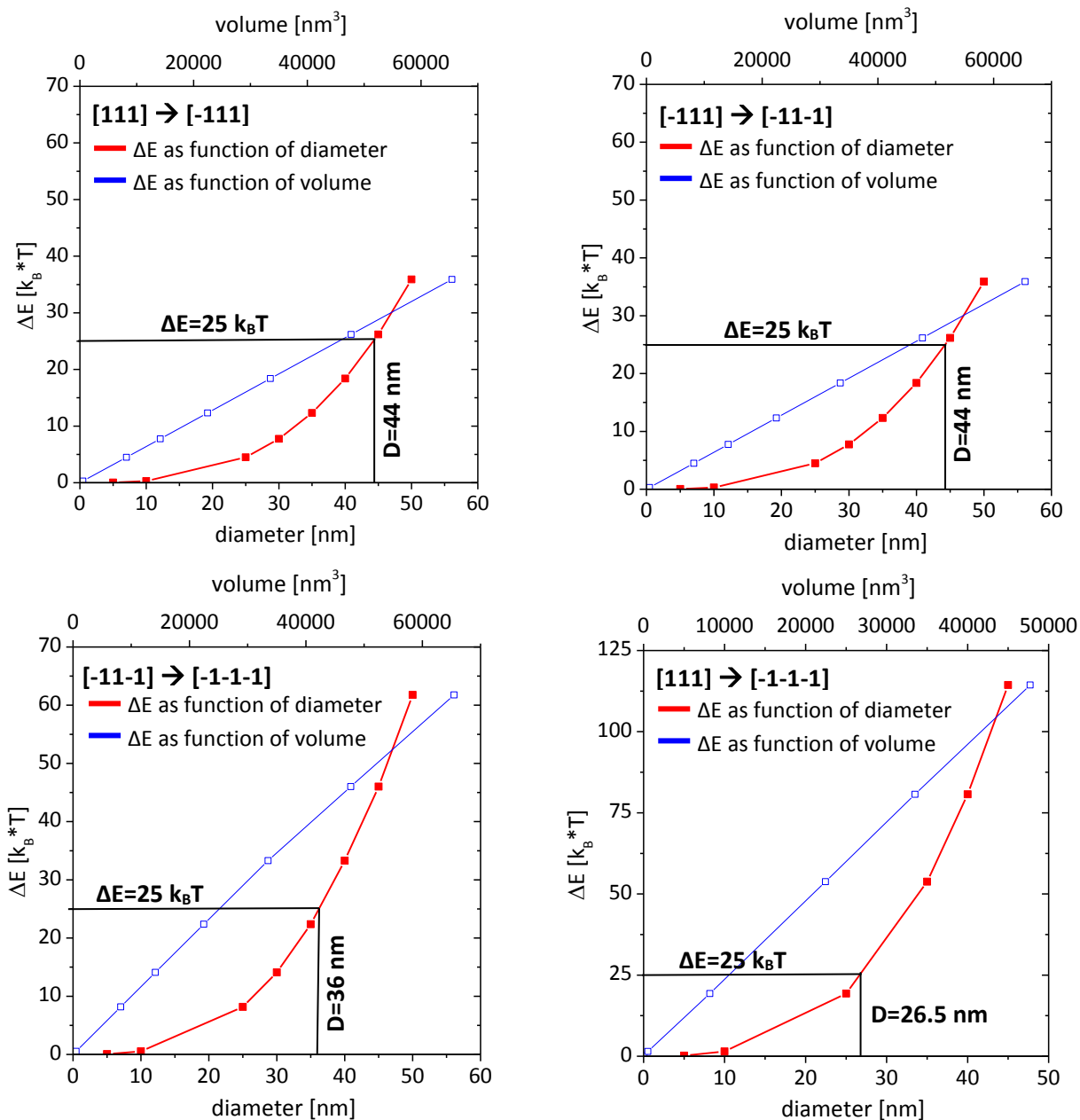


Figure 22: Relation between transition diameter/transition volume and energy barrier revealing when superparamagnetic behaviour appears for a  $Fe_3O_4$  nanosphere; the red curve corresponds to the primary x-axis (diameter) and the blue curve corresponds to the secondary x-axis (volume)

The red curve in the graphs in figure 22 shows the relation between the energy barrier and the particle diameter on the primary x-axis. Also, the graphs include a blue curve corresponding to the secondary x-axis representing the relation between the energy barrier and the particle volume which is approximately linearly in conformity with the approximative formula presented in chapter 2.1:

$$\Delta E \cong K_1 * V \quad (2)$$

The critical diameters/volumes to superparamagnetic behaviour delivered from the illustrated relations above are summarized in table 7. The magnetization reversal from the [111] to the [-1-1-1] direction shows the lowest critical diameter/volume because all three other reversals,

from [111] to [-111], from [-111] to [-11-1] and from [-11-1] to [-1-1-1], contribute to this energy path.

<i>Initial/final state</i>	<i>Transition diameter [nm]</i>	<i>Transition volume [nm<sup>3</sup>]</i>
[111]/[-111]	44	44602
[-111]/[-11-1]	44	44602
[-11-1]/[-1-1-1]	36	24429
[111]/[-1-1-1]	26.5	9744

*Table 7: Summary of all transition diameters and corresponding transition volumes of different magnetization reversals for nanospheres made of magnetite*

### 3.2 Superparamagnetic Transitions of Fe-Spheres

The potential of iron nanoparticles for possible use for biomedical applications has led various research groups to deeper investigate the heating efficiency of iron nanoparticles [63]. Therefore, a closer look at the magnetization reversal of iron nanospheres is taken in this chapter. The used model and dimensions for the simulations are provided in figure 23 and table 8.

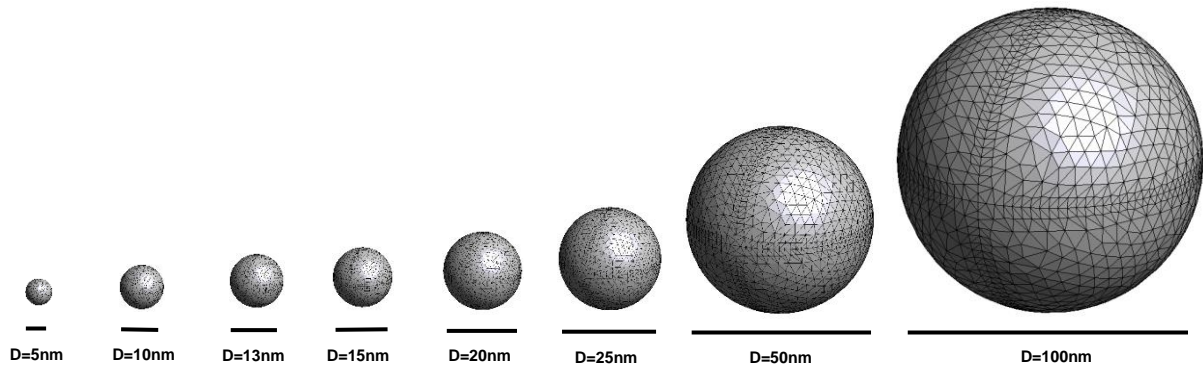


*Figure 23: Models of simulated iron nanospheres ranging from diameter  $D=5\text{nm}$  up to  $D=100\text{nm}$  (designed with GID); the mesh size was scaled down from  $D=100\text{nm}$  with the geometry size*

<i>Diameter [nm]</i>	<i>Volume [nm<sup>3</sup>]</i>
5	65
10	524
13	1150
15	1767
20	4189
25	8181
50	65450
100	523599

*Table 8: diameters and correlating volumes of the simulated iron nanospheres*



Analogous to chapter 3.1, simulating the field magnetization reversal reveals the appearance of incoherent switching behaviour from a specific particle size onwards. Due to the cubic crystal structure of iron, the easy directions are [001], [010], [100] and [00-1]. The field magnetization reversal is performed from the [001] to the [00-1] direction. In the case of iron nanospheres the transition from coherent to incoherent switching behaviour can be observed between nanospheres with a diameter of  $D=25\text{ nm}$  and  $D=50\text{ nm}$  (figure 24).

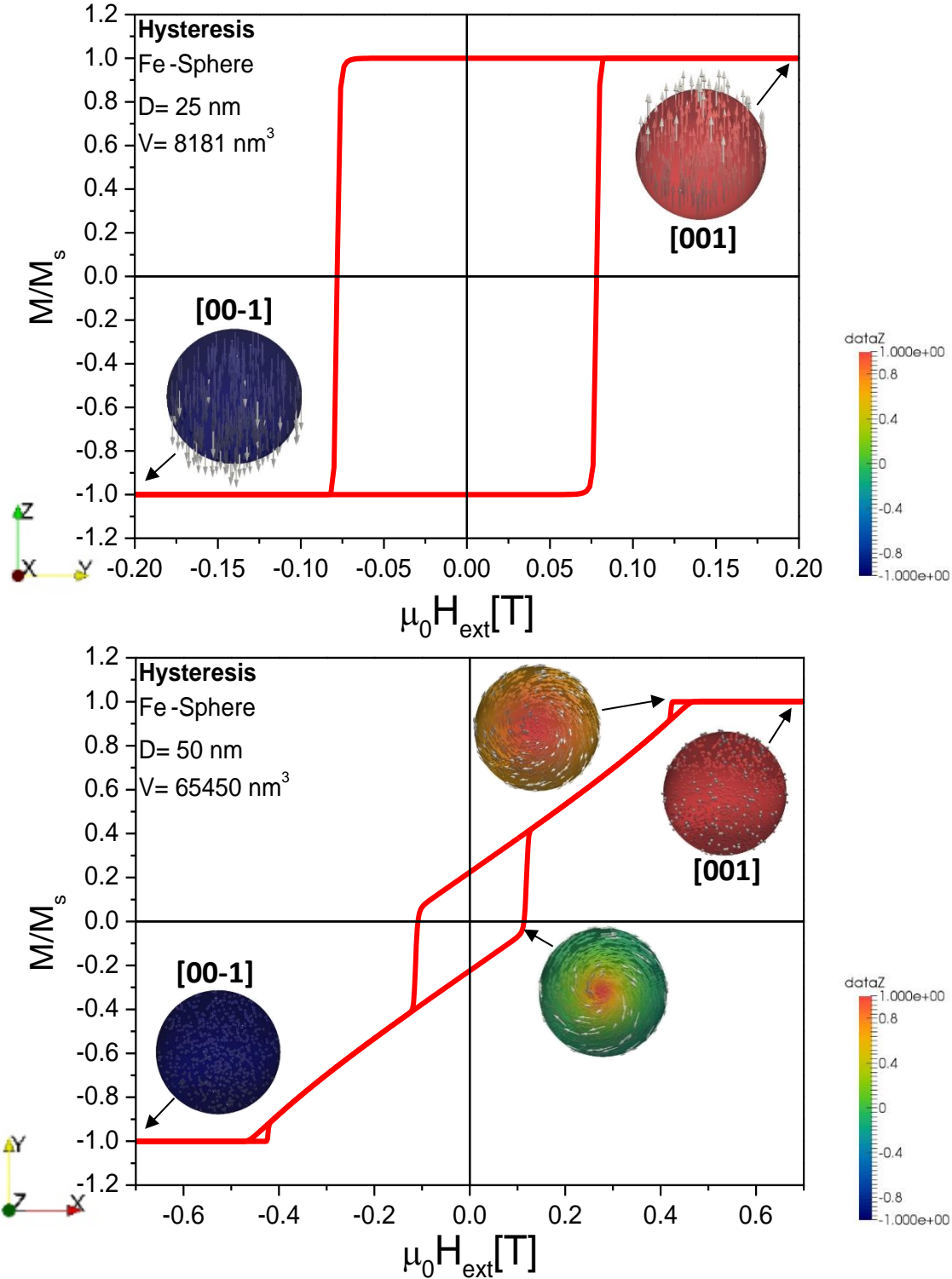


Figure 24: field magnetization reversal from the [001] to the [00-1] easy direction of iron nanospheres with  $D=25\text{ nm}$  (upper graph) and with  $D=50\text{ nm}$  (lower graph); transition from coherent to incoherent switching behaviour

The thermal magnetization reversals were simulated for five different combinations of easy directions of iron's crystal structure, given in table 9. Regarding the minimum energy paths (MEPs) in figures 25 and 26 from the [001] to the [010] direction for the nanospheres with  $D=25$  nm and  $D=50$  nm shows a coherence behaviour similar to the field reversal process. Coherent switching behaviour can be guaranteed for the iron nanosphere with  $D=25$  nm, but not for the  $D=50$  nm sphere. According to these results the validity of the Néel-Arrhenius-equation for the calculation of the limit to superparamagnetic behaviour is ensured for Fe nanospheres with a diameter up to  $D=25$  nm.

Initial easy direction	Final easy direction
[001]	[010]
[001]	[100]
[010]	[00-1]
[100]	[00-1]
[001]	[00-1]

Table 9: Simulated energy paths from one easy direction to another easy direction of Fe

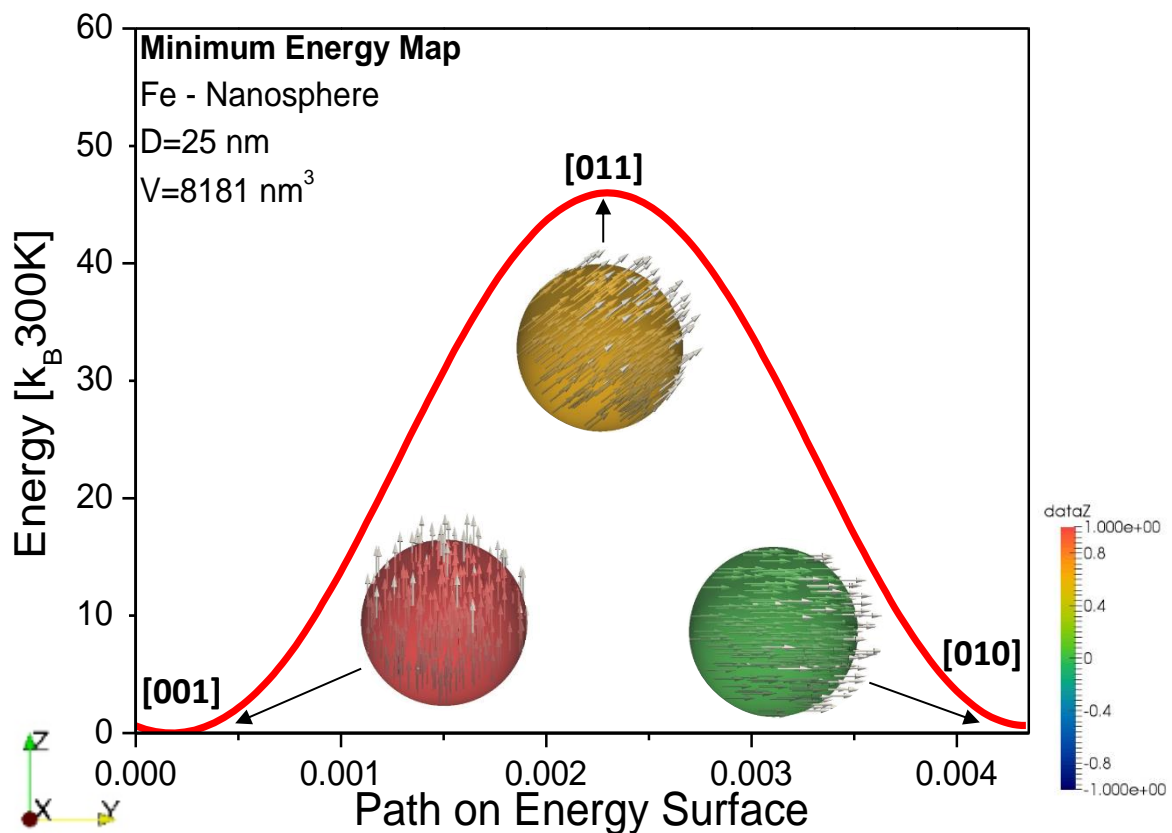


Figure 25: thermal magnetization reversal of the  $D=25$  nm Fe nanosphere from the [001] to the [010] direction showing only coherent switching behaviour

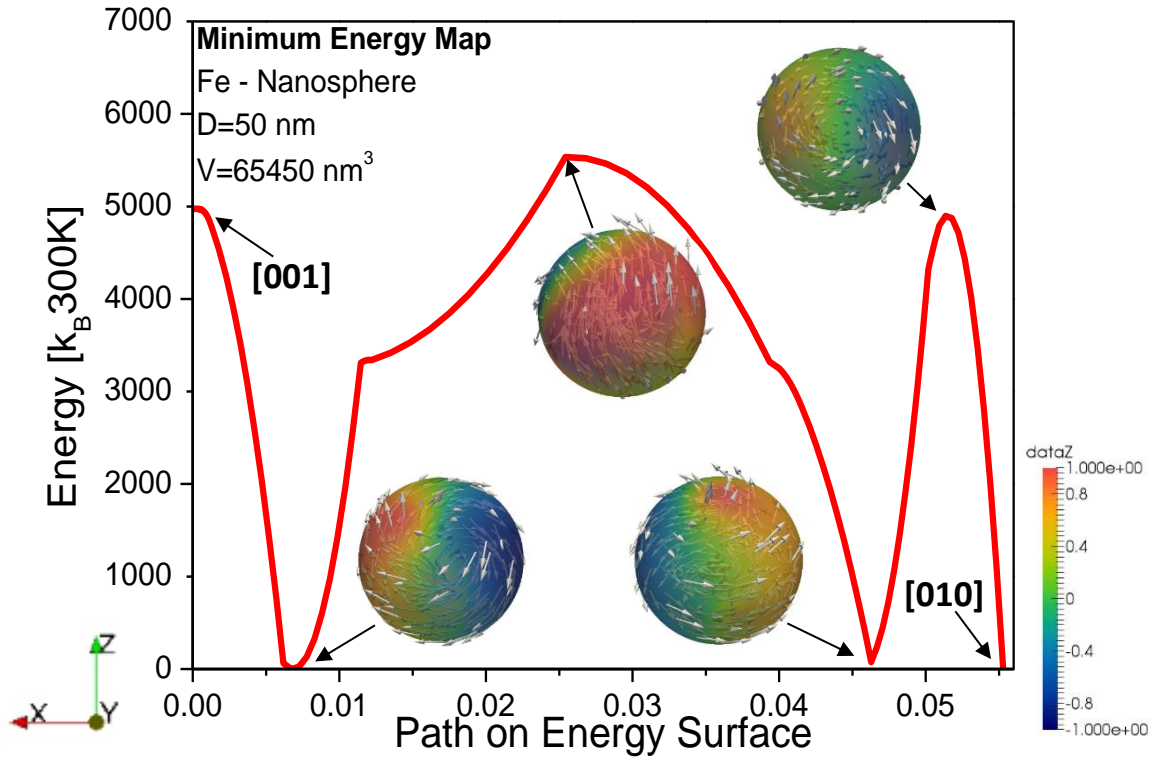


Figure 26: thermal magnetization reversal of the  $D=50$  nm Fe nanosphere from the [001] to the [010] direction showing vortex formation

The minimum energy maps received from micromagnetic simulation enable the interrelation of energy barrier and particle diameter or volume, shown in figure 27, and consequently deliver the transition parameters for superparamagnetic behaviour which are given in table 10. In comparison to the  $\text{Fe}_3\text{O}_4$  nanosphere, the transition parameters are significantly smaller for all simulated energy paths. Due to the fact that the energy barrier is not only dependent of the particle volume  $V$ , but also of the magnetocrystalline anisotropy  $K_1$ , the type of material has also influence on the transition parameters. These results make sense because  $\text{Fe}_3\text{O}_4$  has a smaller value for  $K_1$  than Fe, causing the energy barriers for iron to be higher than for  $\text{Fe}_3\text{O}_4$  and therefore harder to overwind resulting in smaller transition parameters.

<i>Initial/final state</i>	<i>Transition diameter [nm]</i>	<i>Transition volume [nm<sup>3</sup>]</i>
[001]/[010]	19.5	3882
[001]/[100]	17.5	2806
[010]/[00-1]	20.5	4511
[100]/[00-1]	20.5	4511
[001]/[00-1]	16.5	2352

Table 10: Summary of all transition diameters and corresponding transition volumes of different magnetization reversals for nanospheres made of iron

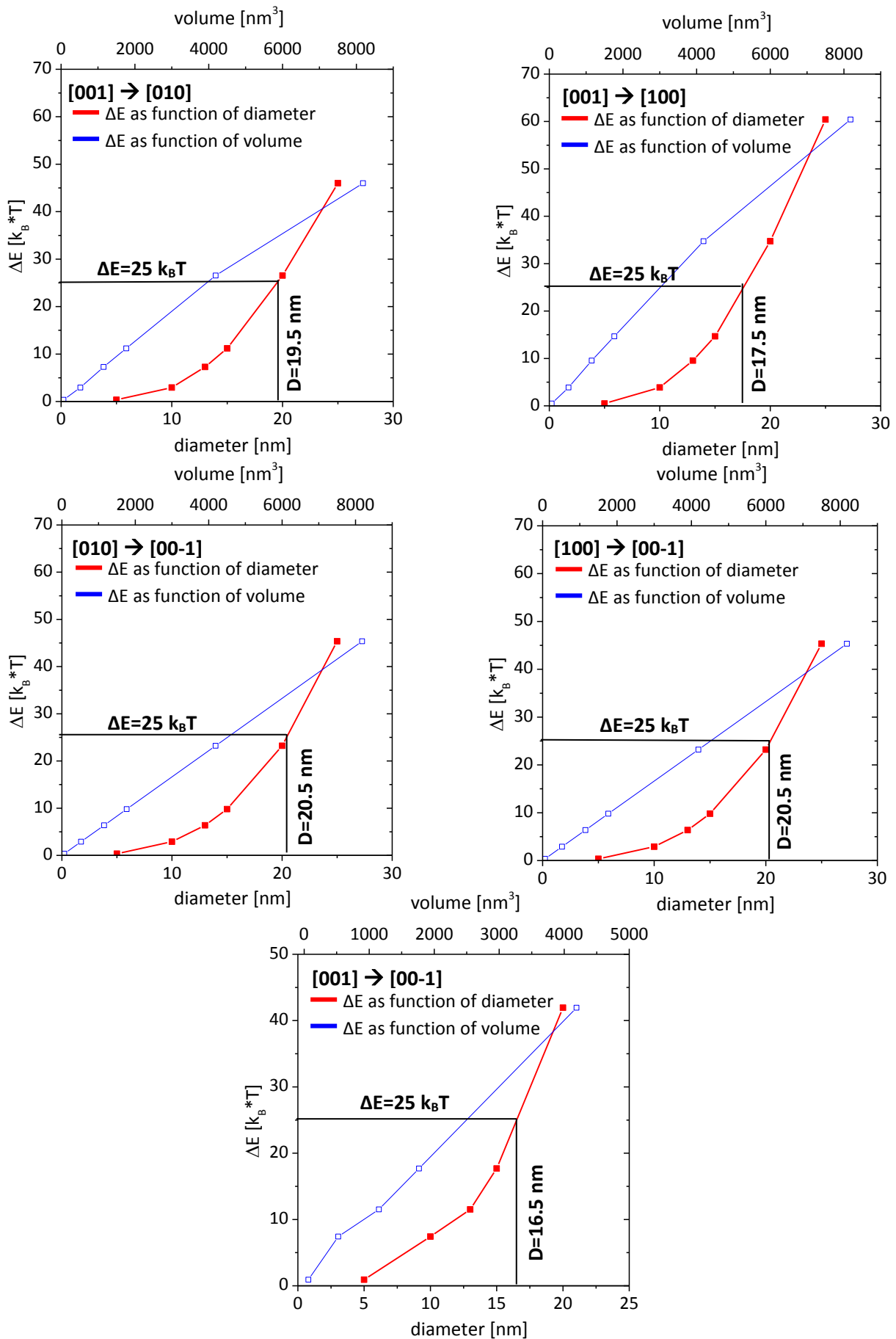


Figure 27: Relation between transition diameter/transition volume and energy barrier revealing when superparamagnetic behaviour appears for an iron nanosphere; the red curve corresponds to the primary x-axis (diameter) and the blue curve corresponds to the secondary x-axis (volume)

### 3.3 Superparamagnetic Transitions of $\text{Fe}_3\text{O}_4$ -Discs

As discussed in chapter 1.4.5, the approach to optimize the heating efficiency for hyperthermia treatments by trying other geometries than spheres is of current interest. Especially nanodiscs show promising results because of their chain-like arrangement which has a positive effect on heat generation.

To investigate the influence of shape on the magnetization reversal and the transition to superparamagnetic behaviour nanodiscs made of magnetite have been simulated. These can, later on, be compared to their spherical counterparts made of the same material. The used model and dimensions are given in figure 28 and table 11.

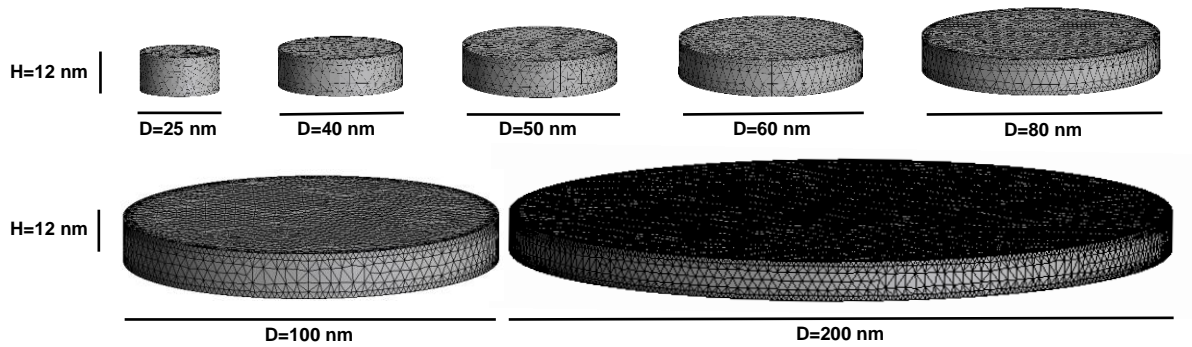


Figure 28: Models of simulated  $\text{Fe}_3\text{O}_4$  nanodiscs ranging from diameter  $D=25$  nm up to  $D=200$  nm at a constant height of  $H=12$  nm (designed with GID)

Height [nm]	Diameter [nm]	Volume [nm <sup>3</sup> ]
12	25	5890
12	40	15080
12	50	23562
12	60	33929
12	80	60319
12	100	94248
12	200	376991

Table 11: height, diameters and correlating volumes of  $\text{Fe}_3\text{O}_4$  nanodiscs

The numerical simulations of the field magnetization reversal deliver hysteresis curves showing incoherent switching behaviour for all models. The simulation was performed, analogously to the  $\text{Fe}_3\text{O}_4$  nanosphere, from the [111] easy direction to the [-1-1-1] easy direction and backwards. The hysteresis curves for the smallest ( $D=25$  nm) and the largest ( $D=200$  nm) are given in figure 29, both revealing incoherent magnetization reversal. If the application of the Néel-Arrhenius-equation is possible, is now dependent on the switching behaviour of thermal magnetization reversal.

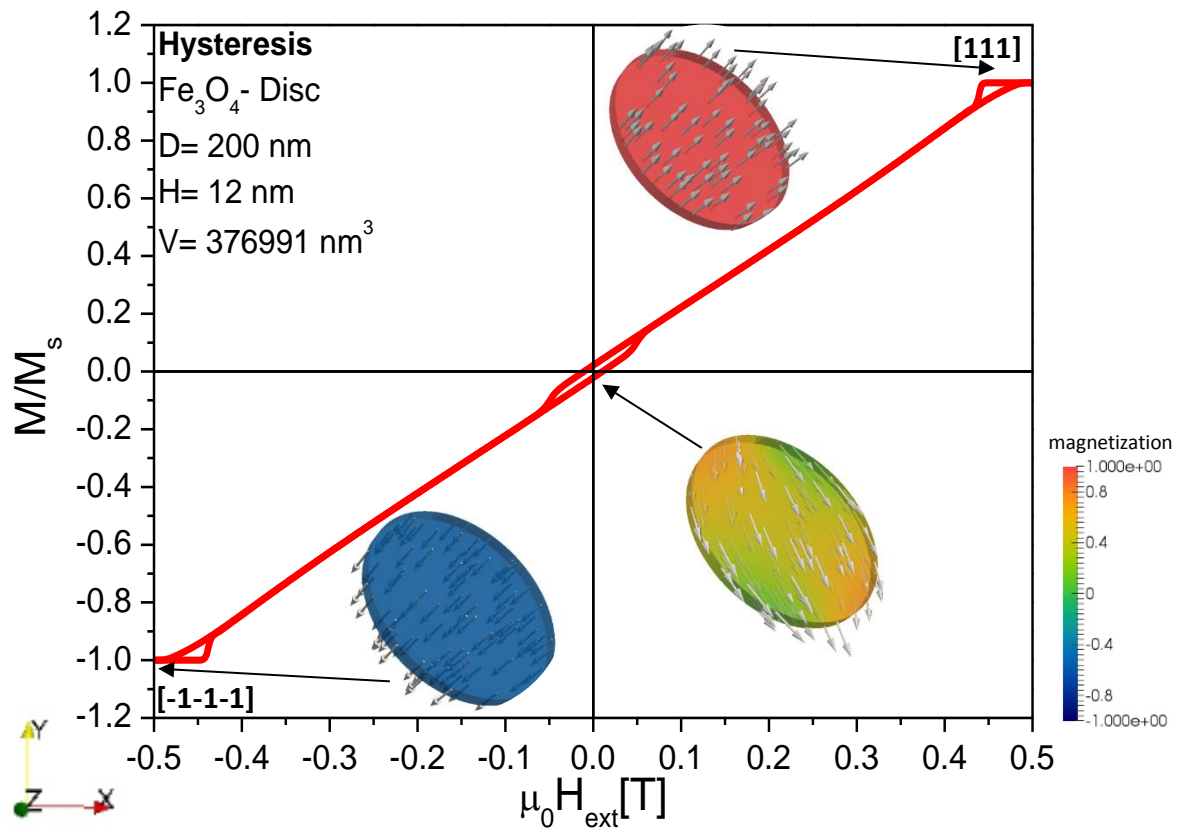
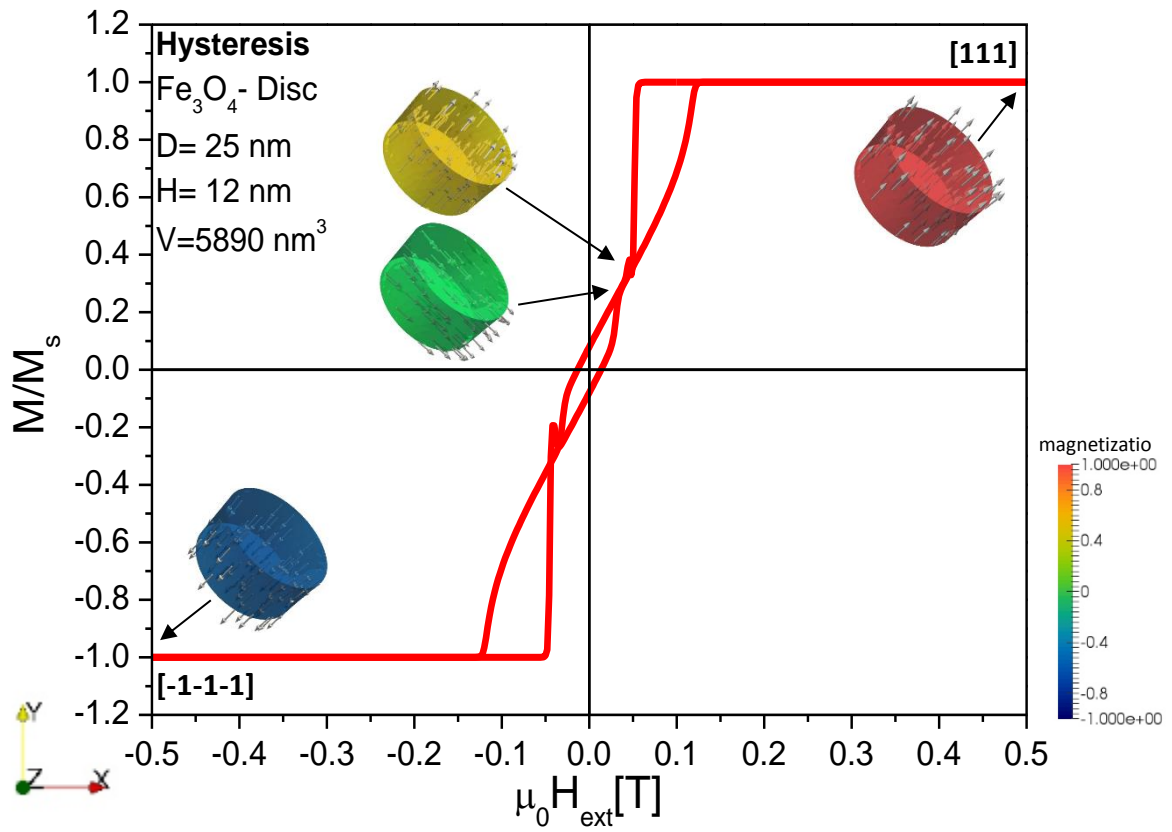


Figure 29: field magnetization reversal from the [111] to the [-1-1-1] easy direction of  $\text{Fe}_3\text{O}_4$  nanodiscs with  $D=25\text{ nm}$  (upper graph) and with  $D=200\text{ nm}$  (lower graph), both at a constant height of  $H=12\text{ nm}$ ; both show incoherent switching behaviour which is also proved by the additional pictures in the graphs

For the thermal magnetization reversals the same easy direction combinations as for the  $\text{Fe}_3\text{O}_4$  nanosphere were simulated to make a comparison between the two geometries possible. These four combinations are listed in table 12. In contrary to the field magnetization reversal, no incoherent switching behaviour was observed at the reversals caused by thermal fluctuations. Even the biggest geometry, a nanodisc with a diameter of  $D=200$  nm, showed only coherent switching. The minimum energy map of the  $D=200$  nm nanodisc and illustrations of different time steps are provided for the energy path from the  $[111]$  to the  $[-111]$  easy direction in figure 30. Hence, the determination of the transition parameters by usage of the Néel-Arrhenius-equation is legitimate and the results are shown in table 13 and figure 31.

Initial easy direction	Final easy direction
$[111]$	$[-111]$
$[-111]$	$[-11-1]$
$[-11-1]$	$[-1-1-1]$
$[111]$	$[-1-1-1]$

Table 12: Simulated energy paths from one easy direction to another easy direction of  $\text{Fe}_3\text{O}_4$

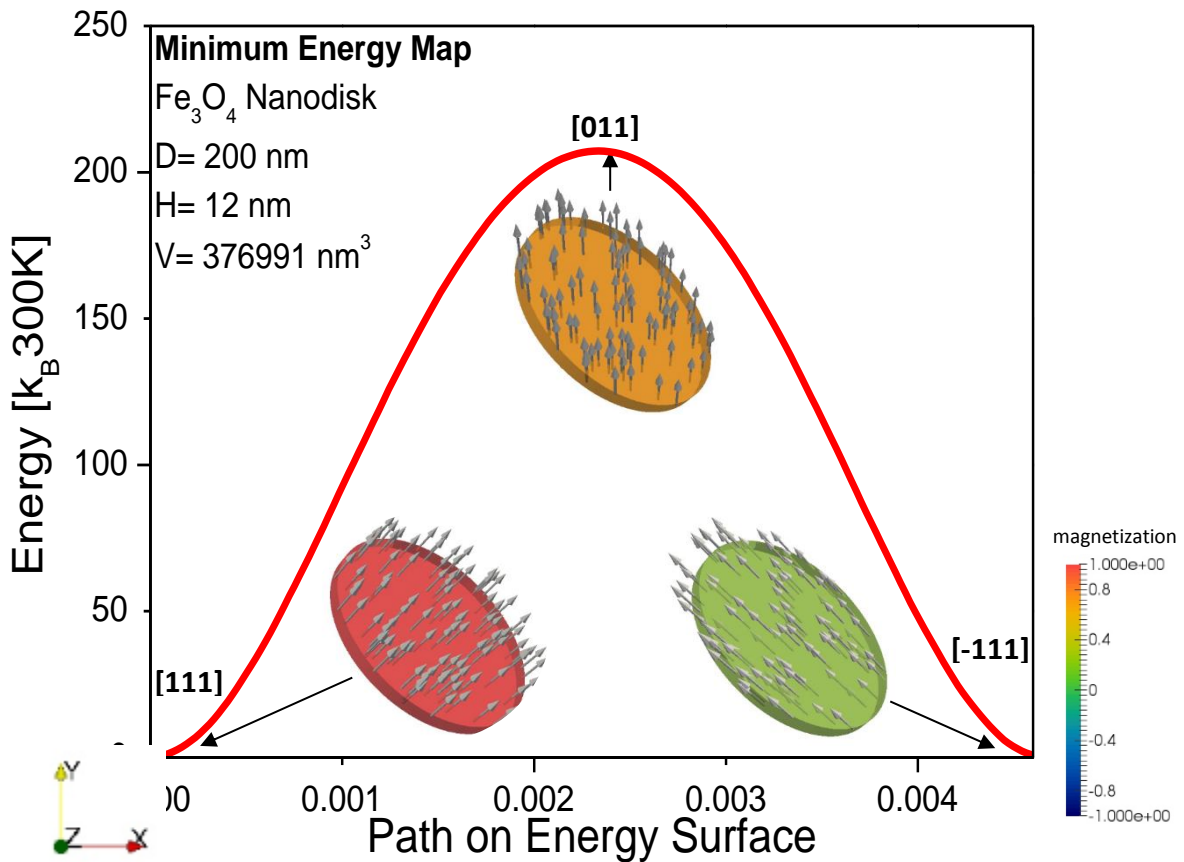


Figure 30: thermal magnetization reversal of the  $D=200$  nm  $\text{Fe}_3\text{O}_4$  nanodisc from the  $[111]$  to the  $[-111]$  direction showing only coherent switching behaviour

<i>Initial/final state</i>	<i>Transition diameter [nm]</i>	<i>Transition volume [nm<sup>3</sup>]</i>
[111]/[-111]	69	44871
[-111]/[-11-1]	69	44871
[-11-1]/[-1-1-1]	47	20819
[111]/[-1-1-1]	29	7926

Table 13: Summary of all transition diameters and corresponding transition volumes of different magnetization reversals for nanodiscs made of Fe<sub>3</sub>O<sub>4</sub>

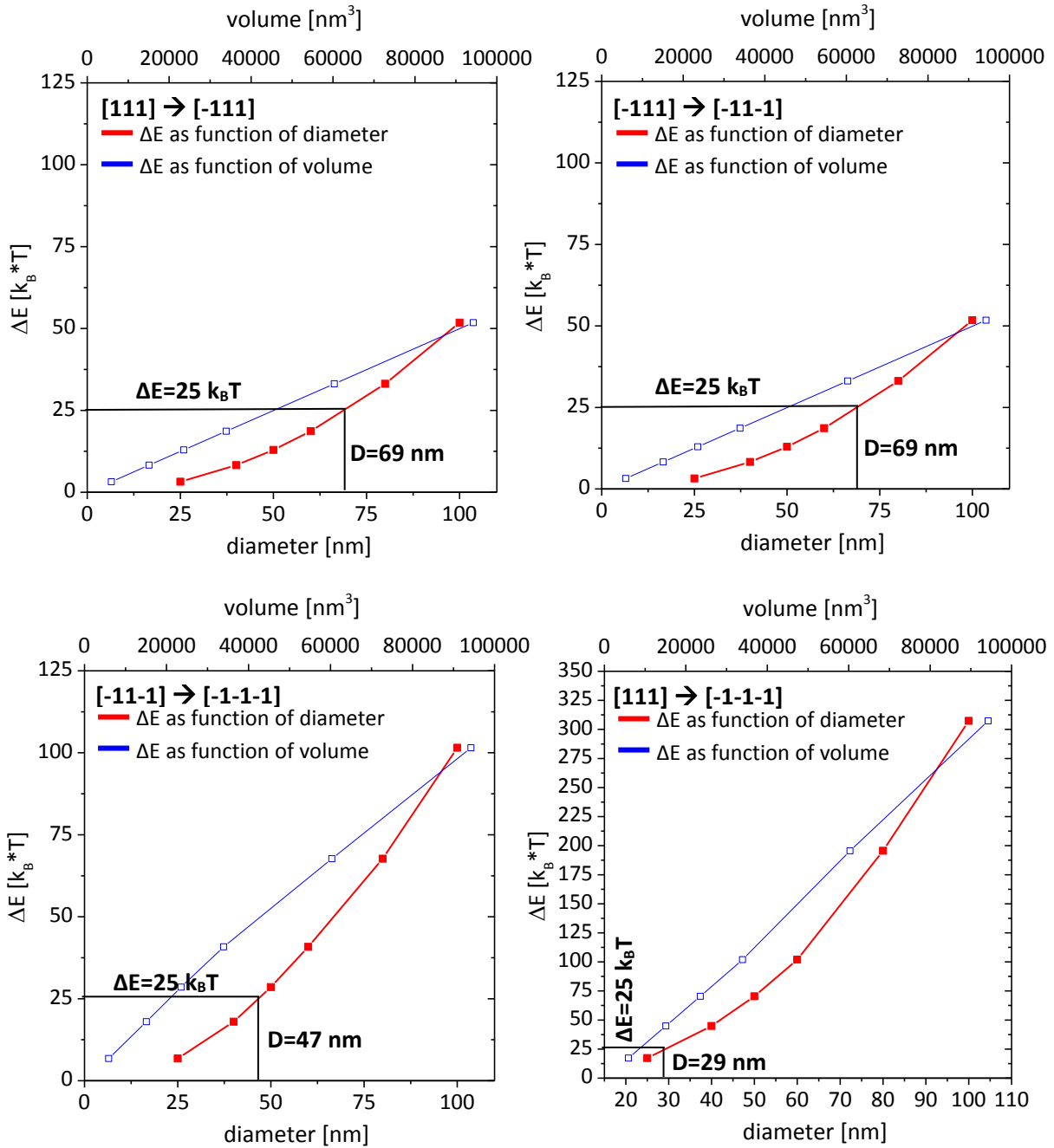


Figure 31: Relation between transition diameter/transition volume and energy barrier revealing when superparamagnetic behaviour appears for a Fe<sub>3</sub>O<sub>4</sub> nanodisc; the red curve corresponds to the primary x-axis (diameter) and the blue curve corresponds to the secondary x-axis (volume)



### 3.4 Micromagnetic Simulation of Fe<sub>20</sub>Ni<sub>80</sub>-Discs

The research in applicability of other geometries than spheres is a highly investigated area of science and has shown interesting results in the last years. The control on shape and dimension of nanoparticles is a primary aim of today's research to eliminate unexpected magnetic behaviour. A promising tool to obtain nanodiscs with monodisperse dimensions is a highly novel method called nanosphere lithography. In 2015, Tiberto et al. [41] presented their work on the fabrication of Fe<sub>20</sub>Ni<sub>80</sub> nanodiscs produced by nanosphere lithography. These nanodiscs are claimed to be suitable magnetic carriers for biomedical applications showing high saturation magnetization and low coercivity.

In a first step a Fe<sub>20</sub>Ni<sub>80</sub> film is deposited on an optical resist which lays on a Si substrate. Then a monolayer of polystyrene nanospheres is put on the permalloy. These nanospheres automatically arrange in a hexagonal lattice and are later downsized by plasma etching. In the next step the free-laying Fe<sub>20</sub>Ni<sub>80</sub> is removed by etching. After removing the nanospheres by sonication in deionized water, the optical resist is dissolved by usage of acetone. What remains are the monodispersed, free-standing Fe<sub>20</sub>Ni<sub>80</sub> nanodiscs. Figure 32 illustrates the described fabrication of nanodiscs by nanosphere lithography.

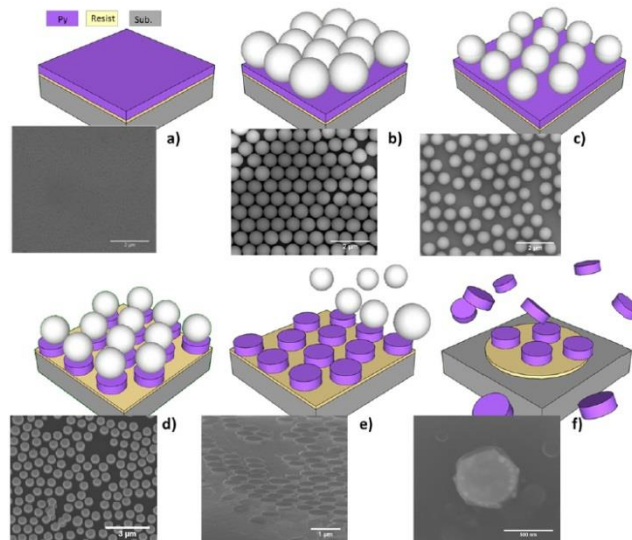


Figure 32: (a) deposition of Fe<sub>20</sub>Ni<sub>80</sub>; (b) deposition of polystyrene nanospheres; (c) shrinking of nanospheres by etching; (d) removing Fe<sub>20</sub>Ni<sub>80</sub> by etching; (e) nanosphere removal by sonication; (f) dissolution of optical resist using acetone [41]

The produced nanodiscs have a height of H=30 nm and a diameter of D=650 nm. According to Tiberto et al., the magnetization reversal is marked by magnetic vortex nucleation which makes them suitable for biomedical applications being detectable at relatively low-frequency, where they display a collective mode spin resonance excitation [64]. For a deeper understanding of the magnetic behaviour of Fe<sub>20</sub>Ni<sub>80</sub> nanodiscs, especially its magnetization reversal, micromagnetic simulations have been performed. Due to computing capacity and in expectation of observing superparamagnetic behaviour, nanodiscs with smaller dimensions than by Tiberto et al. have been investigated. In respect to the method of nanosphere

lithography, the simulated nanodiscs also show constant height and a growing diameter. Figure 33 and table 14 inform about the simulated models and their dimensions.

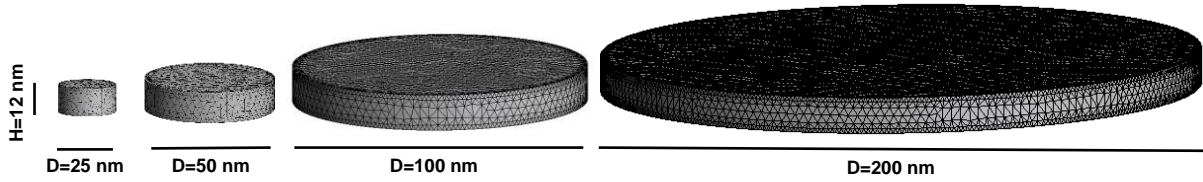


Figure 33: Modells of simulated permalloy nanodiscs ranging from diameter  $D=25$  nm up to  $D=200$  nm with a constant height of  $H=12$  nm (designed with GID)

Height [nm]	Diameter [nm]	Volume [nm <sup>3</sup> ]
12	25	5890
12	50	23562
12	100	94248
12	200	376991

Table 14: Dimensions of simulated  $Fe_{20}Ni_{80}$  nanodiscs (constant height in respect to the method of nanosphere lithography)

Similar to the  $Fe_3O_4$  nanodiscs, the field magnetization reversal shows incoherent behaviour for all simulated model sizes. Exemplarily, the  $D=100$  nm  $Fe_{20}Ni_{80}$  nanodisc, which switches magnetization with clear vortex formation, is illustrated in figure 34. Due to the fact that the magnetocrystalline anisotropy of permalloy is zero and consequently no crystalline direction is preferable, the modells were simulated from the  $[001]$  to the  $[00-1]$  direction. If the application of the Néel-Arrhenius-equation is possible, is now dependent on the switching behaviour of thermal magnetization reversal.

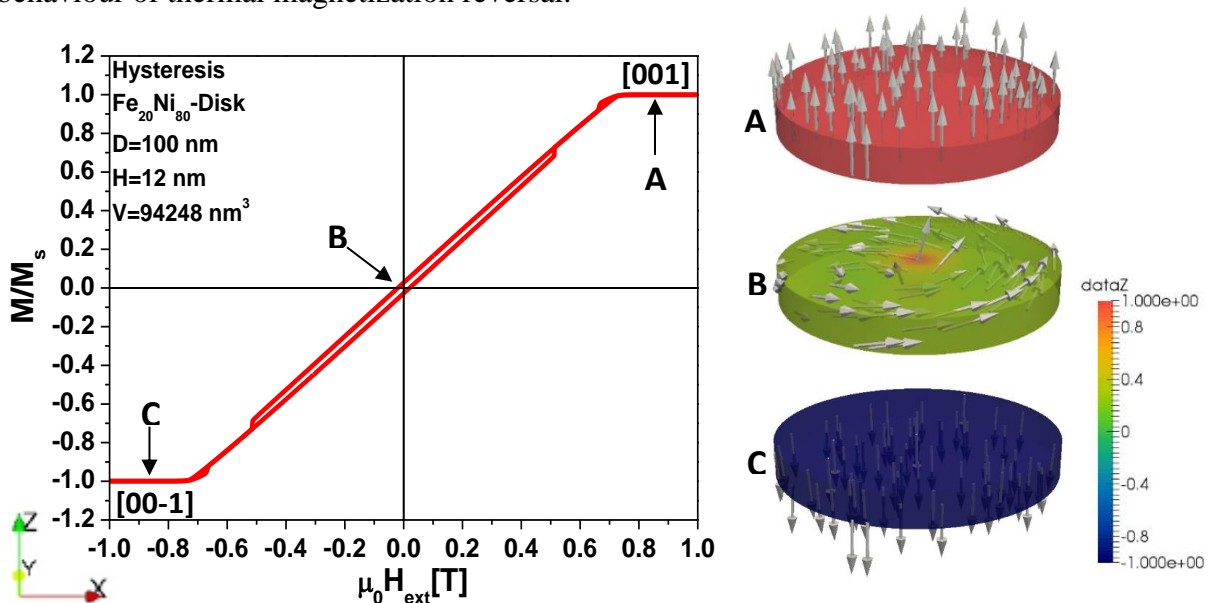


Figure 34: field magnetization reversal from the  $[001]$  to the  $[00-1]$  easy direction of  $Fe_{20}Ni_{80}$  nanodisc with  $D=100$  nm and a constant height of  $H=12$  nm; vortex formation

The analysis of the thermal magnetization reversals revealed that even the smallest model with a diameter of  $D=25$  nm showed incoherent switching behaviour and that the two biggest models with  $D=100$  nm and  $D=200$  nm are characterized by formation of magnetic domains. These interesting results are documented below in figure 35 for the  $D=25$  nm and the  $D=200$  nm nanodisks with an energy path from the  $[001]$  to the  $[100]$  direction. Resulting from the appearing incoherence, a determination of the transition parameters for superparamagnetic behaviour on the basis of the Néel-Arrhenius-equation is not achievable. Nevertheless, this observation provides some possible advantages which will be discussed in chapter 5.

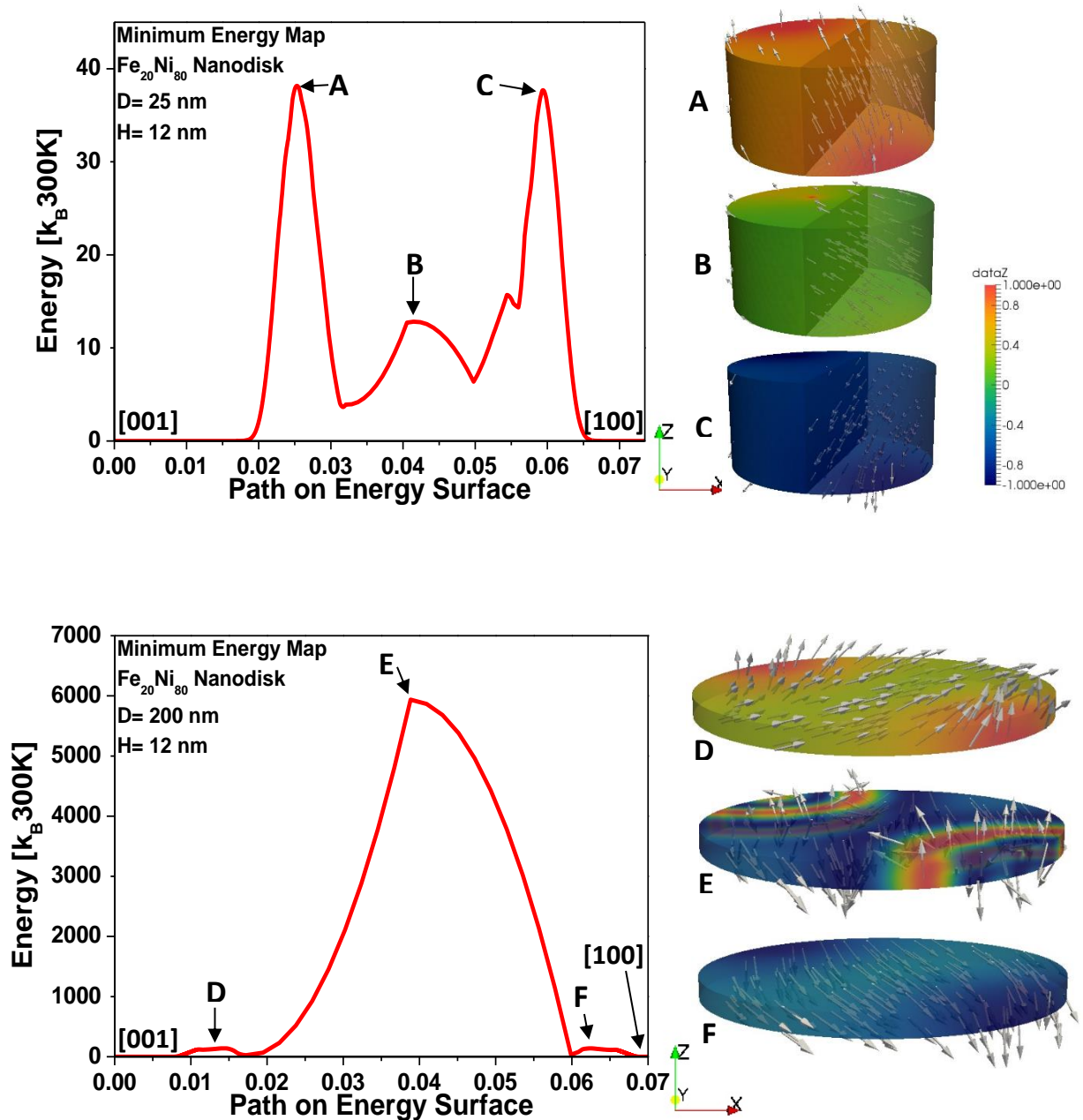


Figure 35: thermal magnetization reversal of the  $D=25$  nm  $\text{Fe}_{20}\text{Ni}_{80}$  nanodisk (upper graph) and the  $D=200$  nm  $\text{Fe}_{20}\text{Ni}_{80}$  nanodisk (lower graph) from the  $[001]$  to the  $[100]$  direction; all simulated models show incoherent switching behaviour

## 4 TEM-Characterization of FeW Nanospheres

### 4.1 Experimental Procedure

The following experimental approach allowed another perspective to the topic of nanoparticles. FeW-nanoparticles, provided by the University of Vienna and the Universidad Autónoma de Madrid, were investigated with different methods, such as high resolution transmission electron microscopy (HRTEM), electron energy loss spectroscopy (EELS) and energy-dispersive X-ray spectroscopy (EDX).

To determine the geometry and the crystal structure of the FeW nanoparticles investigations with a transmission electron microscope (TEM) were performed. This type of microscope uses high energy electrons to take high resolution pictures of a material's crystal structure. The acceleration voltage of the electrons is 200 kV, which accelerates the electrons to approximately 70% of light speed. The wavelength of about 3pm and taking into account lens aberration leads to a maximum resolution of 0.1 nm for an analytical field emission TEM equipped with a high angular annular dark field detector (HAADF) such as the used TECNAI FEI F20 which was used for receiving high resolution bright field images. The field emission TEM was used at spot size 1 and had a C2-aperture with a diameter of 70  $\mu\text{m}$  inserted. To reduce contamination caused by storing the samples were put into a plasma cleaner for 30 seconds before the TEM investigations.

For the determination of the size distribution only overview images were needed which allowed the usage of the TECNAI G20 with a LaB<sub>6</sub> cathode which is not able to provide such high resolution as a field emission TEM.

To receive information about the chemical composition of the nanoparticles EDX and EELS investigations have been performed. The EDX measurements were done by a Silicon Drift Detector (SDD) by the company EDAX. This detector has 4096 channels and was operated at an exposure time of 50 seconds. For the measurements spot size 6 was used and a C2-aperture with a diameter of 30  $\mu\text{m}$  was inserted. The samples were tilted by 20° to the detector. The amplification was 7.68 and the dispersion was 10 eV/channel. The images were taken at a camera length of 200 mm.

Another approach to gain knowledge about the chemical composition was done performing EELS measurements with a Gatan Tridiem GIF electron energy loss spectrometer with 2048 channels. A C2-aperture with a diameter of 30  $\mu\text{m}$  was inserted and spot size 6 was used. In respect of searching for both Fe and W, two different drift tubes were needed. The first drift tube with an exposure time of 1 second was at 450 eV for detecting elements such as iron or oxygen. The second one was at 1300 eV for the detection of tungsten and had an exposure time of 5 seconds. The camera length was 30 mm and the dispersion was 0.5 eV/channel.

## 4.2 Preparation of FeW Nanoparticles

The investigated nanoparticles were fabricated by laser ablation in liquid. This technique enables the production of pure and highly stable nanoparticles. Two sets of samples were provided, one of them produced at the Universidad Autónoma de Madrid<sup>1</sup>, Spain, and the other one fabricated at the University of Vienna<sup>2</sup>, Austria. The experimental laser setup used in the University of Vienna is shown in figure 36.



Figure 36: experimental setup for laser ablation in liquid (University of Vienna)<sup>2</sup>

First of all, FeO and WO are heated and pressed to a ceramic plate. A small piece of these ceramics is glued onto the bottom of a glass cylinder which is filled with ethanol or distilled water. Then the plate is irradiated with a pulsed laser beam which causes laser ablation. The processes during laser ablation are illustrated in figure 37.

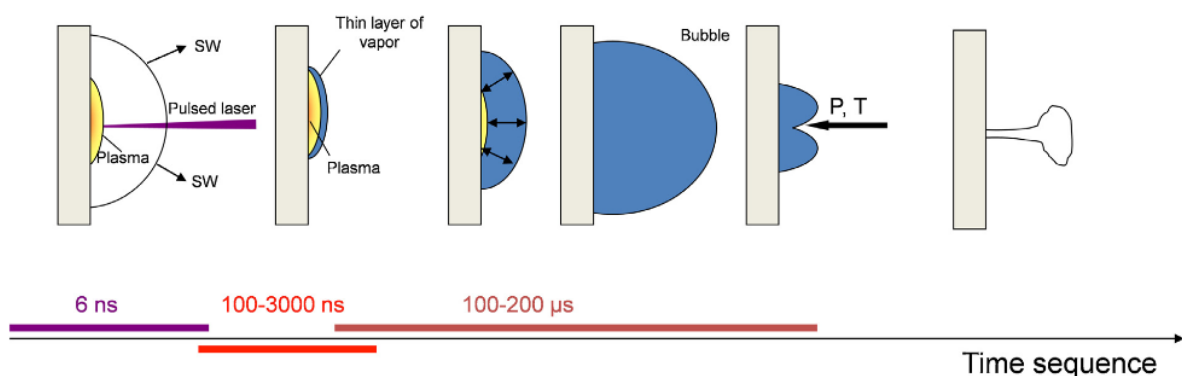


Figure 37: Time sequence of laser ablation in a liquid [65]

<sup>1</sup> Dr. Óscar Bomati-Miguel, Universidad Autónoma de Madrid, Departamento de Física Aplicada, Facultad de Ciencias, 28049 Madrid

<sup>2</sup> Univ.-Prof. Dr. Wolfgang Kautek, University of Vienna, Faculty of Chemistry, Department of Physical Chemistry, Physical Chemistry and Nanotechnology of Interfaces, Währinger Straße 42, 1090 Vienna

The intense laser beam evaporates the target and many atoms and molecules are ejected from the target. These ablated particles form a hot plasma in front of the ceramic target. The plasma expands which causes a shock wave in the surrounding liquid. Then the plasma itself slows down until it finally extinguishes. After the disappearance of the emissive plasma, we observe the formation of a cavitation bubble in ambient liquid, which is another unique phenomenon of liquid-phase laser ablation. This formation is caused by the thin layer of vapour between the plasma and the liquid, which has a very high pressure. The cavitation bubble, which contains material of the ceramic plate, expands with time. After reaching the maximum size, the cavitation bubble shrinks continuously and collapses at a point close to the target surface. Nanoparticles surrounded by liquid are the result. ([65], [66])

After this fundamental preparation step, the nanoparticles in liquid have to be prepared for a TEM-investigation. The preparation of sample set (A) of the Universidad Autónoma de Madrid was finished in Madrid by placing drops of the liquid containing nanoparticles on a copper grid with a carbon film. The liquid, ethanol, then evaporated and only the nanoparticles were left on the carbon film.

Sample set (B) from the University of Vienna was provided in liquid form, so the second preparation step was accomplished at the TU Vienna. To keep the amount of carbon on a particle as small as possible, copper grids with lacey carbon films, as pictured in figure 38, were used. This made it possible to find nanoparticles on the edge of a carbon film to determine the chemical composition without a high influence of the carbon. The preparation itself was accomplished similar to the preparation performed in Madrid: One drop of the nanoparticle solution was placed on the ring with the copper grid and then the ethanol evaporated. This process was repeated three times per sample to ensure that a sufficient amount of nanoparticles was found on the carbon film.

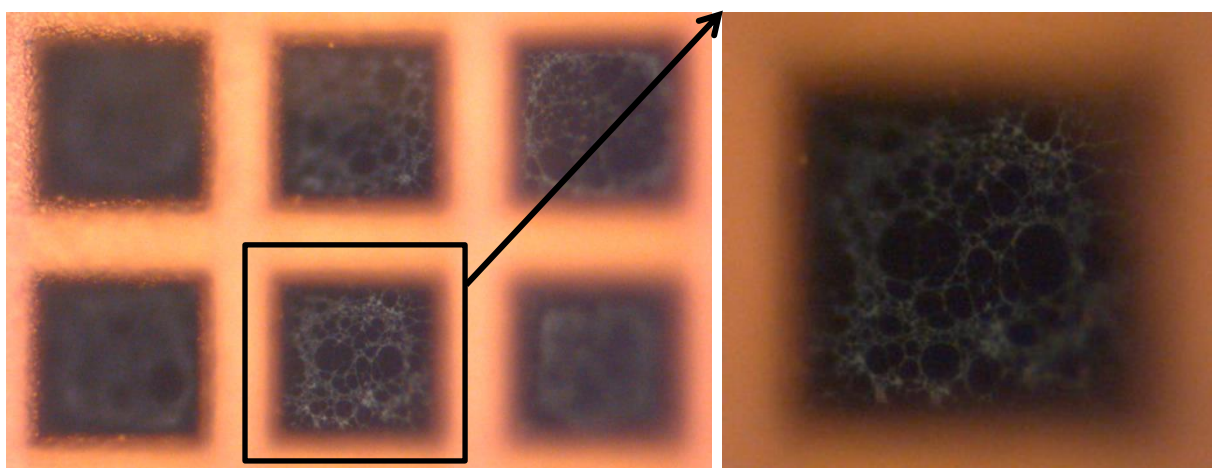


Figure 38: (a) section of a ring with a copper grid and lacey carbon film on the grid;  
(b) magnified lacey carbon film

### 4.3 Description of the Investigated Samples

Two sample sets (A) and (B), one of each preparation location, were investigated. The main differences between the two experimental setups for fabrication in Spain and Austria are the applied laser wavelength and the laser repetition rate which differ significantly from each other. These differences had a big influence on the nanoparticles' properties which will become obvious later on. The data concerning the production of the nanoparticles by laser ablation in liquid is provided in table 15.

	<i>Sample set (A)</i>	<i>Sample set (B)</i>
<b><i>Manufactured</i></b>	University of Vienna, Austria	Universidad Autónoma de Madrid, Spain
<b><i>Target</i></b>	FeO-WO ceramic	
<b><i>Solvent</i></b>	Ethanol	
<b><i>Laser wavelength</i></b>	<b>532 nm</b>	<b>1064 nm</b>
<b><i>Laser repetition rate</i></b>	<b>20 Hz</b>	<b>25 kHz</b>
<b><i>Laser pulse duration</i></b>	5 ns	few ns
<b><i>Laser power</i></b>	950 mW	≈ 1000 mW

Table 15: Preparation parameters for both sample sets (A) and (B)

According to the used target composition of FeO and WO ceramic, there are several possibilities of expectable phases of the resulting nanoparticles. The most probable phases are listed below (table 16) and have been paid special attention to during the analysis of the crystal structure of the nanoparticles.

<b><i>Expected Phases</i></b>					
<b><i>Iron-based</i></b>	$\alpha$ -Fe	FeO	Fe <sub>2</sub> O <sub>3</sub>	Fe <sub>3</sub> O <sub>4</sub>	
<b><i>Tungsten-based</i></b>	W	WO <sub>2</sub>	WO <sub>3</sub>	W <sub>2</sub> O <sub>5</sub>	W <sub>5</sub> O <sub>14</sub>
<b><i>Mixture</i></b>	WFe <sub>2</sub>	FeW <sub>x</sub> O <sub>y</sub>			

Table 16: List of expectable phases

With the knowledge of their atomic positions the most important crystal structures of the phases from table 17 were designed with the software VESTA [67]. These are given on the following pages.

crystal structure	lattice constants [nm]			space group	reference
	a	b	c		
$\alpha$ -Fe	0.2866	0.2866	0.2866	Im-3m (229)	[68]
FeO	0.427	0.427	0.427	Fm-3m (225)	[69]
Fe <sub>2</sub> O <sub>3</sub>	0.523	0.503	1.375	R-3c h (167)	[70]
Fe <sub>3</sub> O <sub>4</sub>	0.8397	0.8397	0.8397	Fd-3m O1 (227)	[71]
W	0.3160	0.3160	0.3160	Im-3m (229)	[72]
WO <sub>2</sub>	0.5563	0.4896	0.5663	P21/c (14)	[73]
WO <sub>3</sub>	0.7298		0.3899	P6/mmm (191)	[74]

Table 17: possible crystal structures and lattice parameters for the prepared nanoparticles

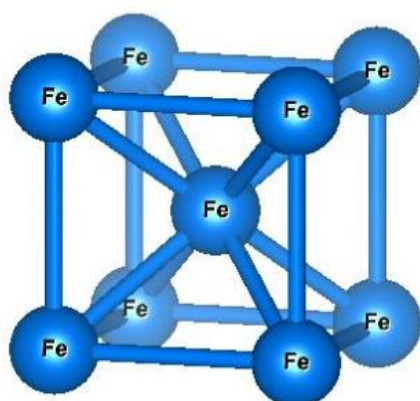


Figure 39: unit cell of  $\alpha$ -Fe

$\alpha$ -Fe				
atom	position	x	y	z
Fe	2a	0	0	0

Table 18: atomic positions of  $\alpha$ -Fe

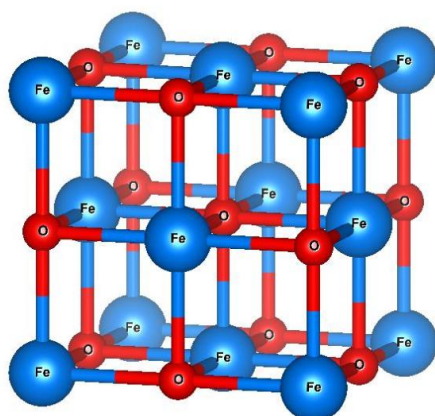


Figure 40: unit cell of FeO

FeO				
atom	position	x	y	z
O	4b	0.5	0.5	0.5
Fe	4a	0	0	0

Table 19: atomic positions of FeO



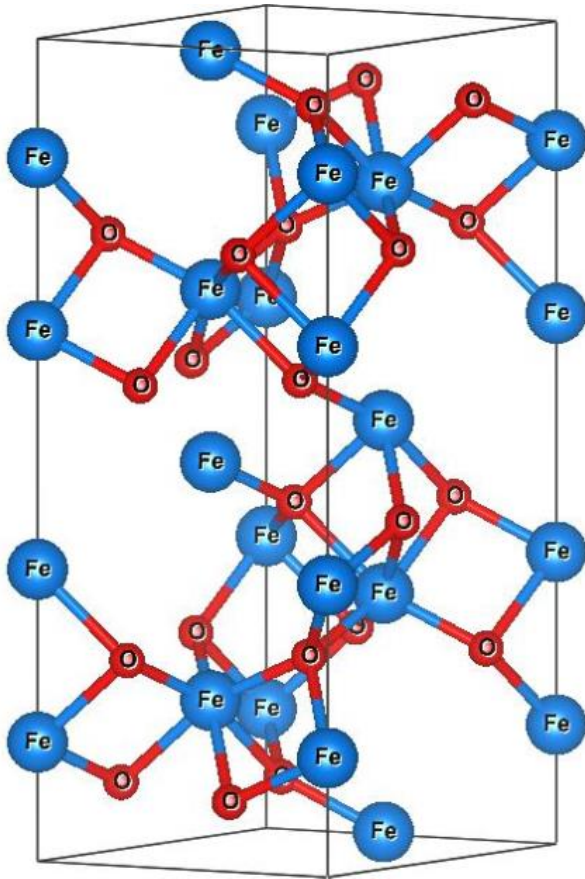


Figure 41: unit cell of  $Fe_2O_3$

### $Fe_2O_3$

atom	position	x	y	z
O	18e	0.3082	0	0.25
Fe	12c	0	0	0.14502

Table 20: atomic positions of  $Fe_2O_3$

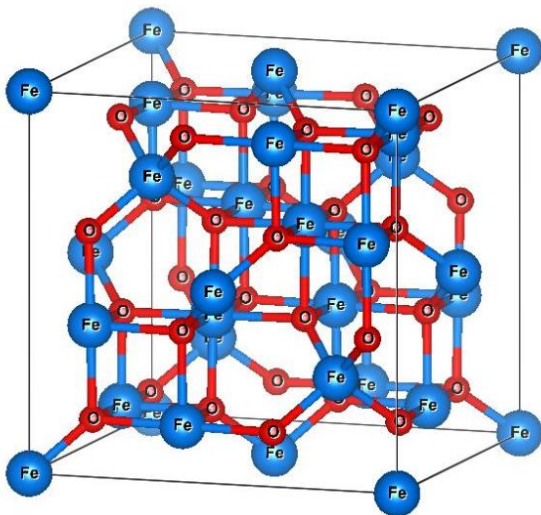


Figure 42: unit cell of  $Fe_3O_4$

### $Fe_3O_4$

atom	position	x	y	z
O	32e	0.246	0.246	0.246
Fe2	16c	0	0	0
Fe1	8b	0.375	0.375	0.375

Table 21: atomic positions of  $Fe_3O_4$

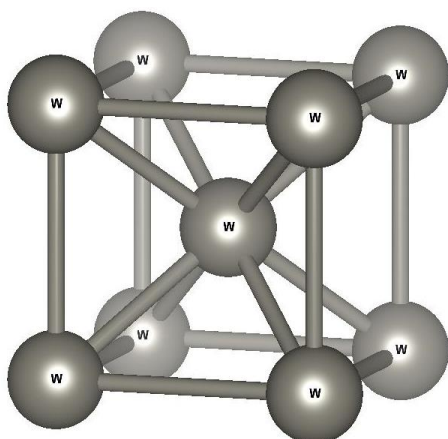


Figure 43: unit cell of W

W				
atom	position	x	y	z
W	2a	0	0	0

Table 22: atomic positions of W

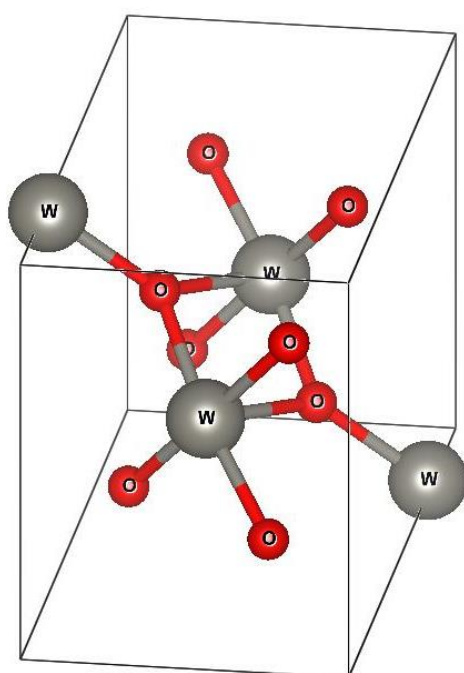


Figure 44: unit cell of WO<sub>2</sub>

WO <sub>2</sub>				
atom	position	x	y	z
O1	4e	0.1119	0.2186	0.2334
O2	4e	0.39	0.7024	0.2986
W	4e	0.2278	0.9898	0.0111

Table 23: atomic positions of WO<sub>2</sub>

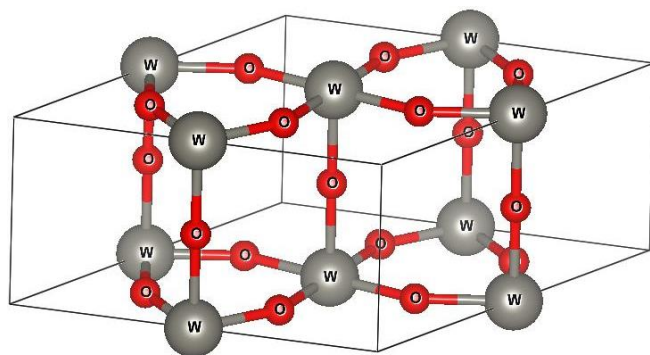


Figure 45: unit cell of WO<sub>3</sub>

WO <sub>3</sub>				
atom	position	x	y	z
W	3f	0.5	0	0
O1	3g	0.5	0	0.5
O2	6l	0.212	0.424	0

Table 24: atomic positions of WO<sub>3</sub>

#### 4.4 Determination of the Size Distribution

To determine if superparamagnetism is a relevant effect for the investigated FeW nanoparticles, the TEM images were used to measure the diameters of the pictured nanoparticles. The measurement of a statistically appropriate amount of nanoparticle diameters enabled the determination of the size distribution.

To obtain a size distribution as accurate as possible, the diameters were measured manually in use of the software “Digital Micrograph” designed by the company Gatan Inc. The diameters of the particles and, if existing, the diameters of their cores were measured by drawing circles around the spherical particles. Also, the particles were numbered consecutively to enable a reconstruction of the measurement process.

Two samples, one of each sample set, were added for diameter measurement. Table 25 shows the amount of particles measured per sample. For a statistical relevant size distribution sample B7 is most appropriate, because the TEM investigation made a measurement of more than 1000 nanoparticle diameters possible.

<i>Sample</i>	<i>Amount of particles measured</i>	<i>Production country</i>
A1	278	Austria
B7	1067	Spain

Table 25: Amount of analyzed particle diameters

##### 4.4.1 Size Distribution of Sample A1

Due to the lower laser wavelength and the lower laser repetition rate, these samples contain very large nanoparticles as one can see in figure 47, a TEM bright field image of sample A1. The histogram of 278 measured particle diameters is given in figure 48(a). Figure 48(b) represents the size of core diameters in relation to the particle diameters. To illustrate the meaning of the terms core diameter and particle diameter figure 46 is provided. Not all of the particles had cores, so in figure 48(b) only the particles with cores are regarded. The figures show that sample A contains very large nanoparticles with many particles with a diameter above 100 nm and a very broad size distribution. The particle diameters vary from 16 nm up to 706 nm. The average diameter is given by 157 nm. The average ratio between core diameter and particle diameter could be calculated to be 0.48.

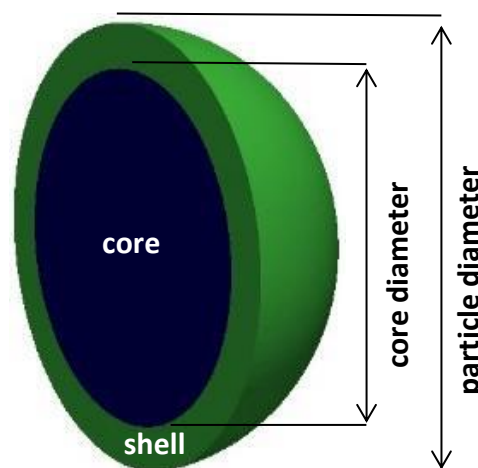


Figure 46: Illustration of a core/shell structure and term definitions

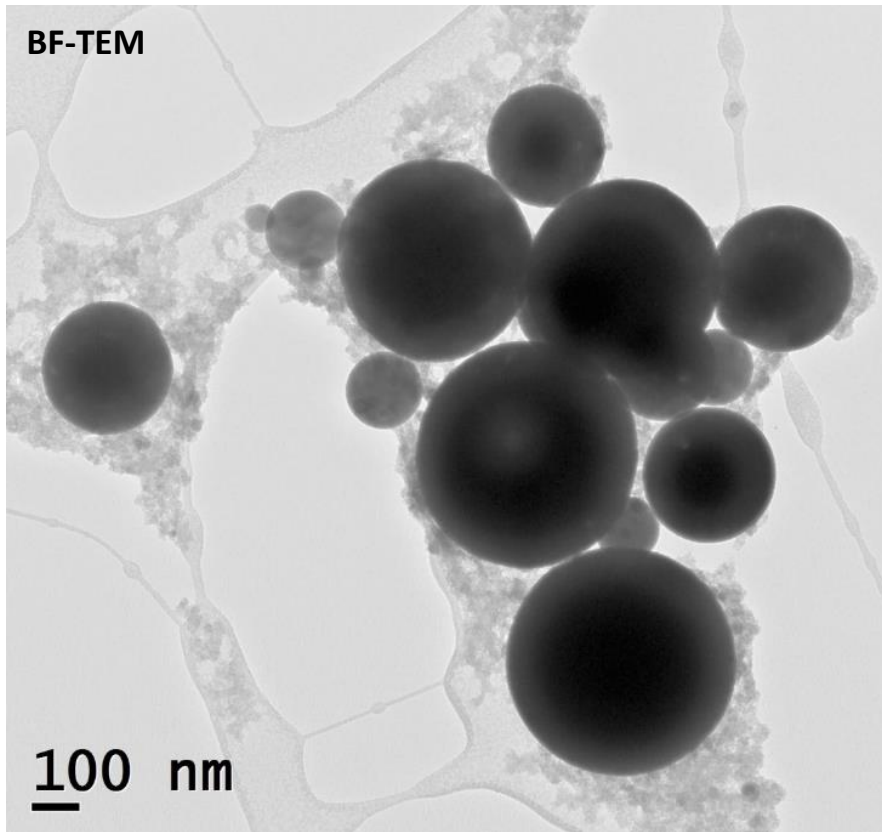


Figure 47: TEM bright field image of sample A1: very large nanoparticles with broad size distribution of spherical homogenous or core/shell particles

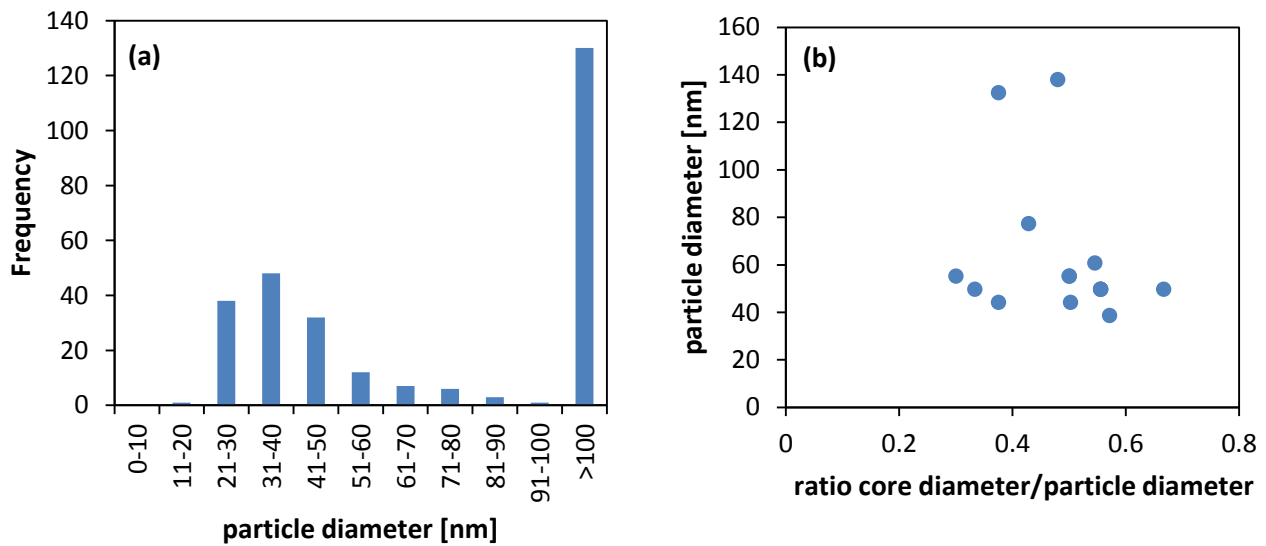


Figure 48: (a) size distribution of the 278 measured nanoparticles of sample A1: average particle diameter of 157 nm; (b) ratio between core diameters to particle diameters, if a particle had a core: average ratio of 0.48

#### 4.4.2 Size Distribution of Sample B7

As illustrated in the TEM bright field image in figure 49, the nanoparticles of sample B7 highly differ in size from the nanoparticles of sample A1. As mentioned above, these significant differences in size are caused by the different laser preparation parameters. Due to a high amount of appropriate TEM images, a measurement of 1067 nanoparticles of sample B7 was possible. The size distribution of these measured nanospheres is given in figure 50(a). Figure 50(b) represents the size of core diameters in relation to the particle diameters. Not all of the particles had cores, so in figure 50(b) only the particles with cores are regarded. Also sample B7 shows a broad size distribution with particle diameters varying from 8 nm up to 170 nm. The average particle diameter is given by 44 nm. The average ration between core diameter and particle diameter was measured to be 0.51.

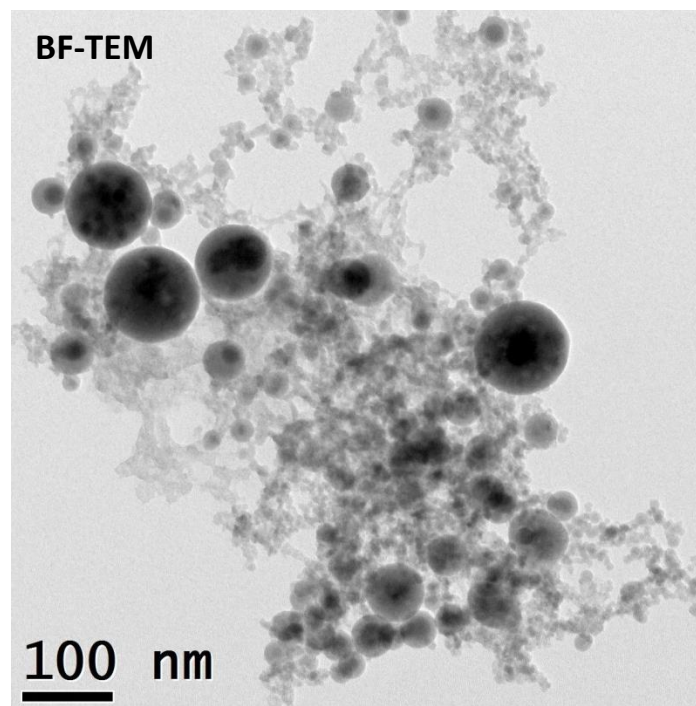


Figure 49: TEM bright field image of sample B7: broad size distribution with small nanoparticles in comparison to sample A1; observation of both homogenous and core/shell particles

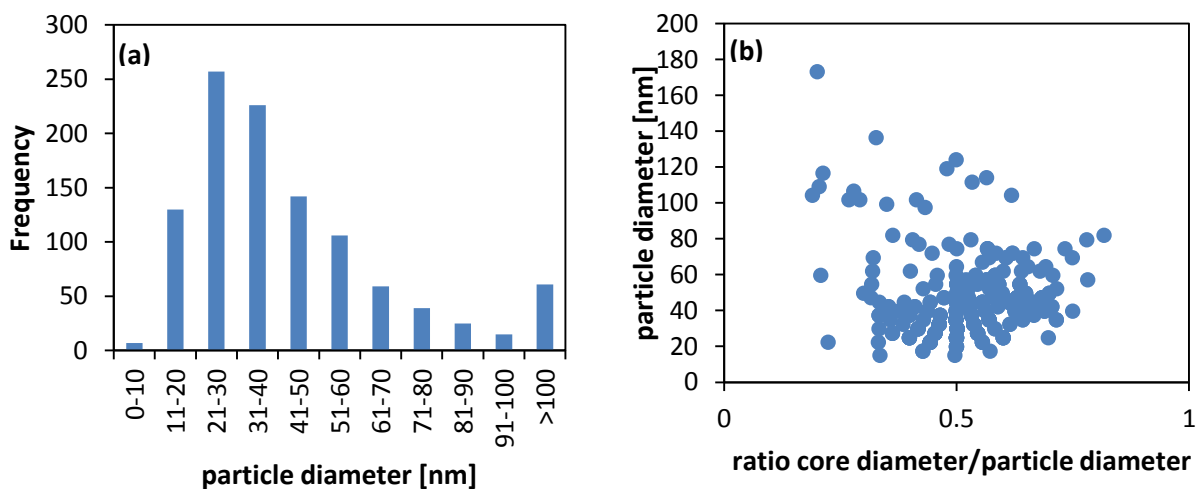


Figure 50: (a) size distribution of the 1067 measured nanoparticles of sample B7: average particle diameter of 44 nm; (b) ratio between core diameters to particle diameters, if a particle had a core: resulting in an average ratio of 0.51

## 4.5 Analysis of the Crystal Structure and Chemical Composition

During the performance of, in total, five TEM investigations two different types of particles have been found both in sample sets (A) and (B). Most particles showed a core/shell structure, but some particles did not own a core and were of homogenous shape. Especially the core/shell structure is of great interest for biomedical applications such as drug delivery as explained in chapter 1.3.3. Further knowledge about the crystal structure and chemical composition of core and shell is highly desirable. The two different types of nanoparticles found, can be seen in figure 51.

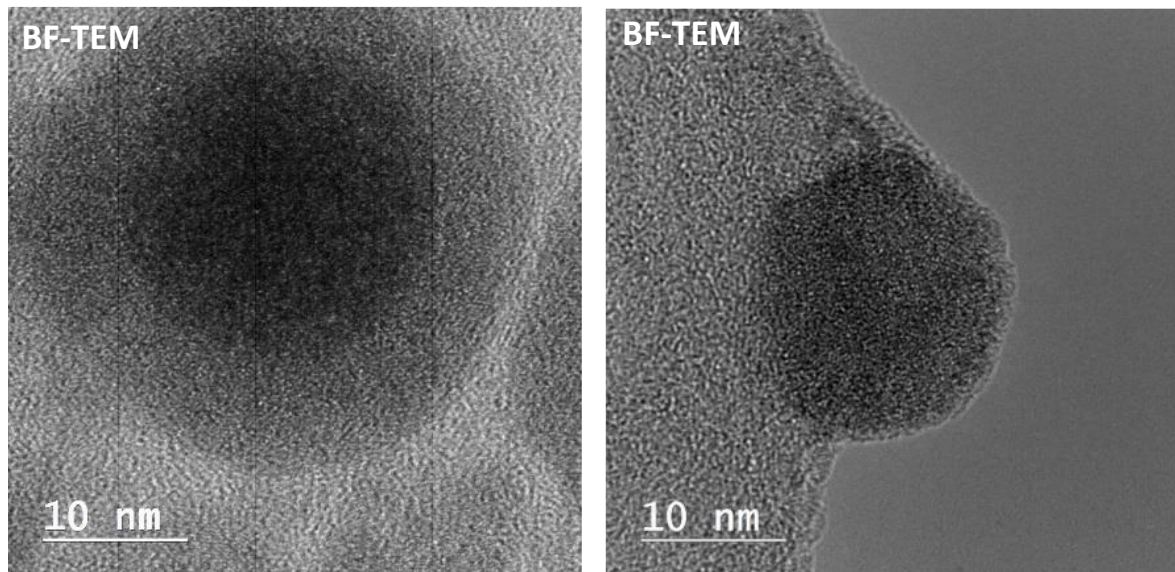


Figure 51: nanoparticle with core/shell structure (left); nanoparticle with a homogenous structure (right)

### 4.5.1 Characterization of Sample Set (A)

As described in chapter 4.4.1, sample set (A) contained very large particles with diameters up to 700 nm which made an investigation with HRTEM and EELS impossible. Also, the large size of the nanoparticles make the probability of an appearance of superparamagnetism very small which makes a further characterization of sample set (A) not necessarily relevant for this diploma thesis.

### 4.5.2 Characterization of Sample Set (B)

In contrast to sample set (A), sample set (B) with its smaller nanoparticles enabled a characterization of the crystal structure and chemical composition of some core/shell nanoparticles. Figure 52 shows a bright field image of sample B7 and a HRTEM-image of a nanoparticle's core. The visible lattice planes could be identified as the [110] direction of  $\alpha$ -Fe with a measured lattice plane distance of 0.199 nm.

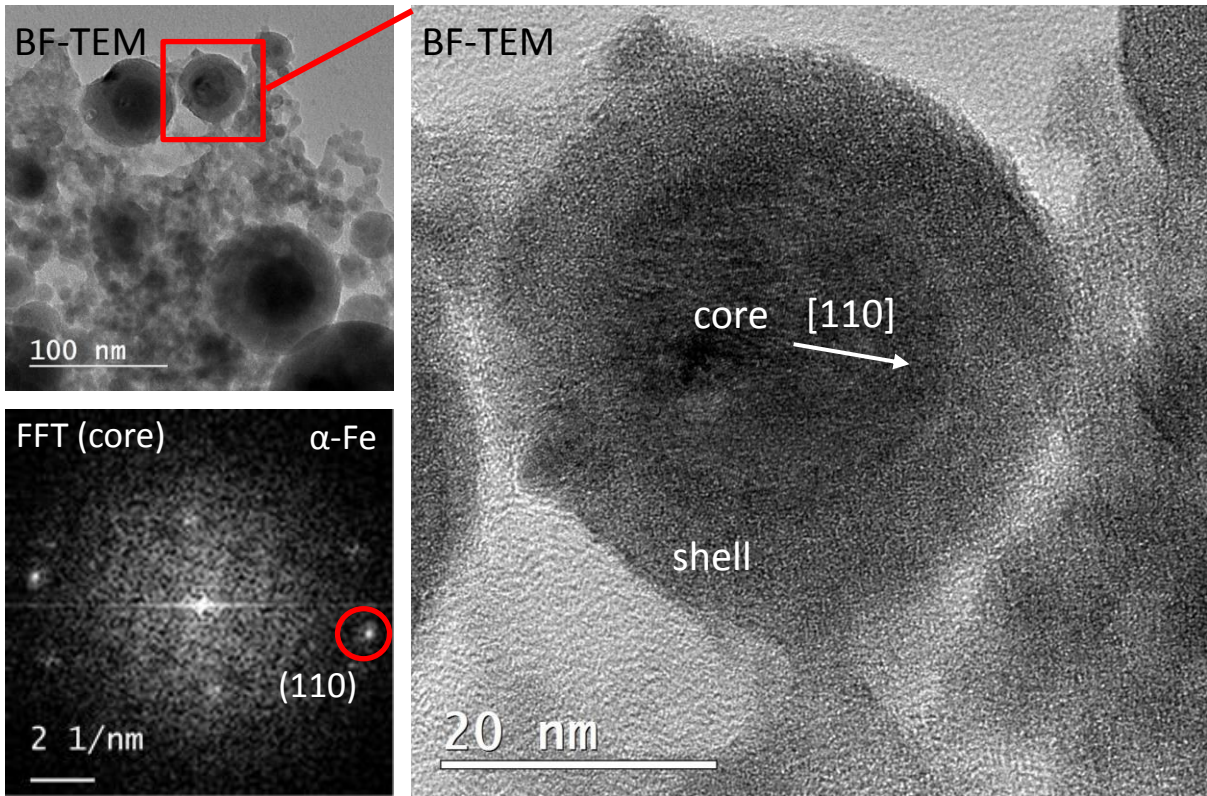


Figure 52: bright field images of sample B7 showing a core-shell-nanoparticle with an  $\alpha$ -Fe-core in the [110] direction; FFT of the particle's core with the brightest spot identified as the (110) reflection of  $\alpha$ -Fe

It was also possible to accomplish an EDX measurement of the same particle to better understand the chemical composition of both core and shell areas. The EDX line scan in figure 53 indicates an  $\alpha$ -Fe-core due to the drop of oxygen in the nanoparticle's core. The EDX spots illustrated in figure 54 lead to the assumption that there is far more  $\alpha$ -Fe in the core of the nanoparticle than in the shell and that W shows the opposite behaviour. The appearance of carbon and copper can be explained by the preparation method containing a copper grid with a carbon film on it.

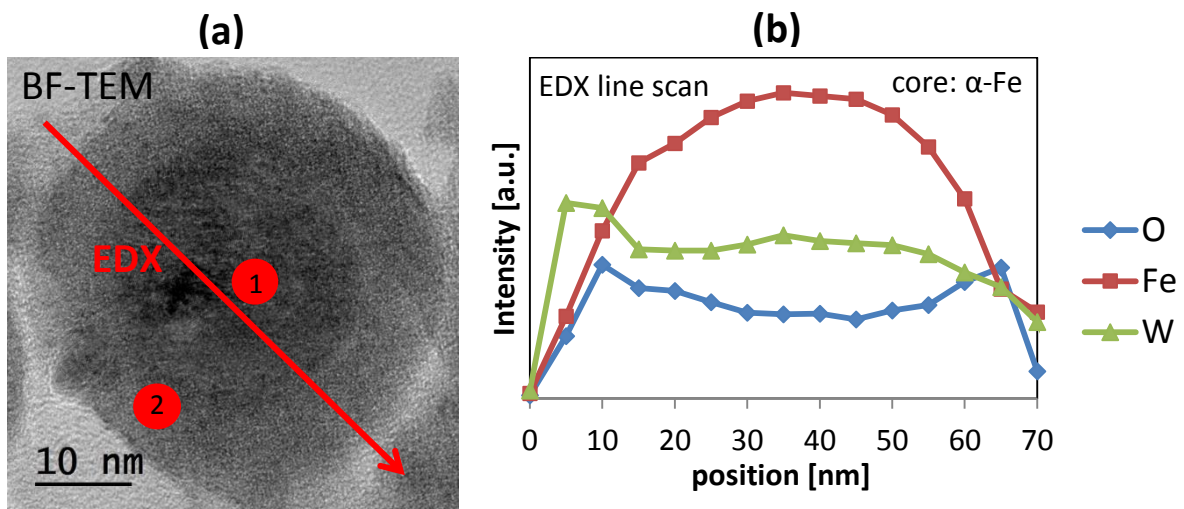
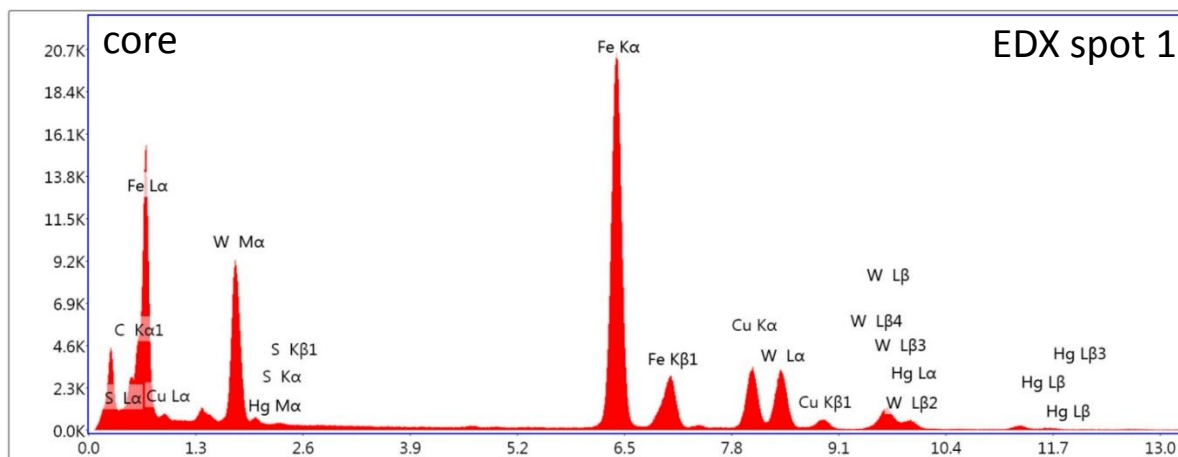


Figure 53: (a) location of the performed EDX line scan and the two EDX spots on a nanoparticle of sample B7; (b) EDX line scan of the above particle assuming an  $\alpha$ -Fe containing core

(a)

	O	Fe	W
[at.%]	8.33	50.86	13.87



(b)

	O	Fe	W
[at.%]	10.9	20.45	24.84

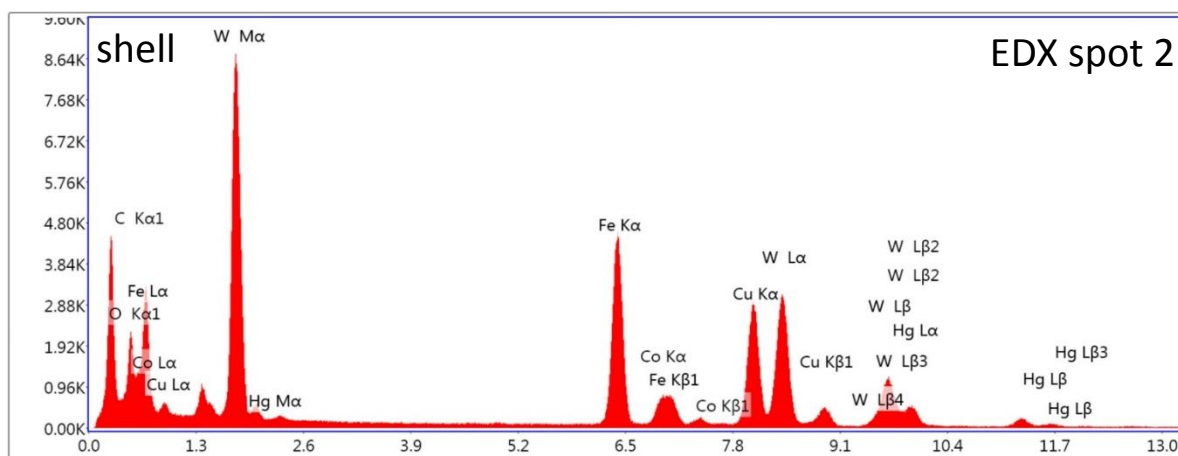


Figure 54: (a) EDX spot of the nanoparticle's core in figure 53 showing a high amount of iron; (b) EDX spot of the nanoparticle's shell in figure 53 indicating to a lower amount of iron and a higher amount of tungsten and oxygen in the shell than in the core



The appearance of  $\alpha$ -Fe-cores was also approved by EELS measurements. At this type of spectroscopy the spectrum of energy loss of monoenergetic electrons after the interaction with the sample is determined. The diagram in figure 55 shows a high rise of  $\alpha$ -Fe in the core and a simultaneous drop of tungsten and oxygen.

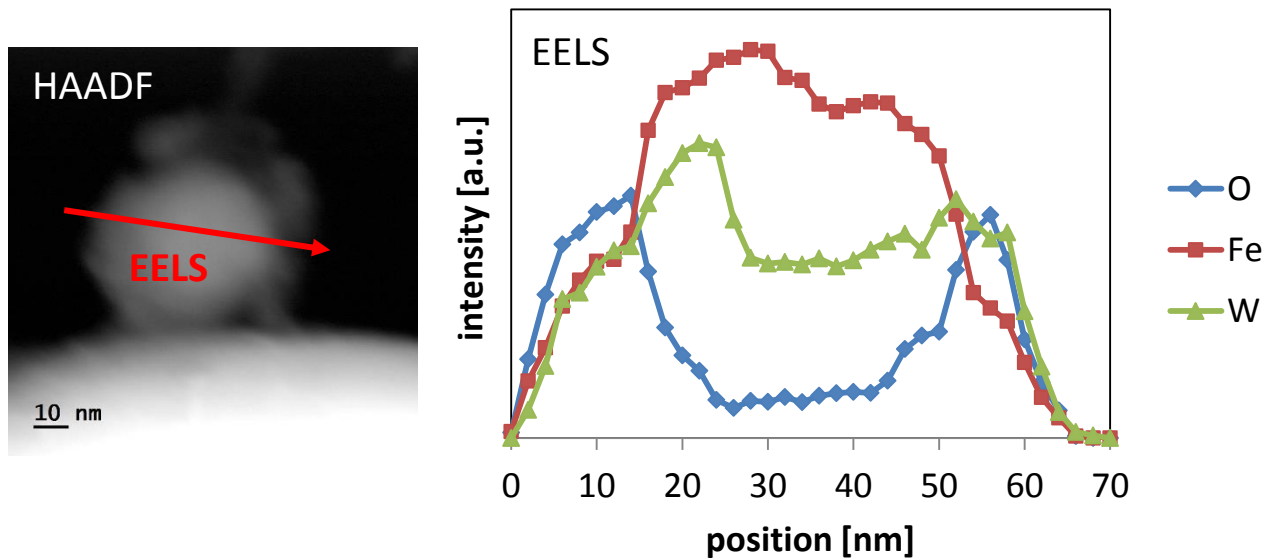


Figure 55: STEM image in HAADF mode of a core/shell nanoparticle (left); measured EELS intensity spectrum of the left particle with rising iron and dropping tungsten and oxygen in the core (right)

Furthermore, a second type of core was identified with the help of HRTEM and EDX measurements. A bright field image of sample B7 can be seen in figure 56. The visible lattice planes in the core were identified to be the [400] direction of  $\text{Fe}_3\text{O}_4$ . A second example of a  $\text{Fe}_3\text{O}_4$  core is illustrated in figure 57. The [400] direction of  $\text{Fe}_3\text{O}_4$  and the [110] direction of  $\alpha\text{-Fe}$  are very similar to each other, which gives rise to doubts about the existence of two different types of cores. But fortunately, not only the analysis of the crystal structure indicated the existence of a  $\text{Fe}_3\text{O}_4$  core, but also EDX measurements showed different properties than the previously illustrated ones. An EDX line scan with both rising Fe and O in the nanoparticle's core is shown in figure 58.

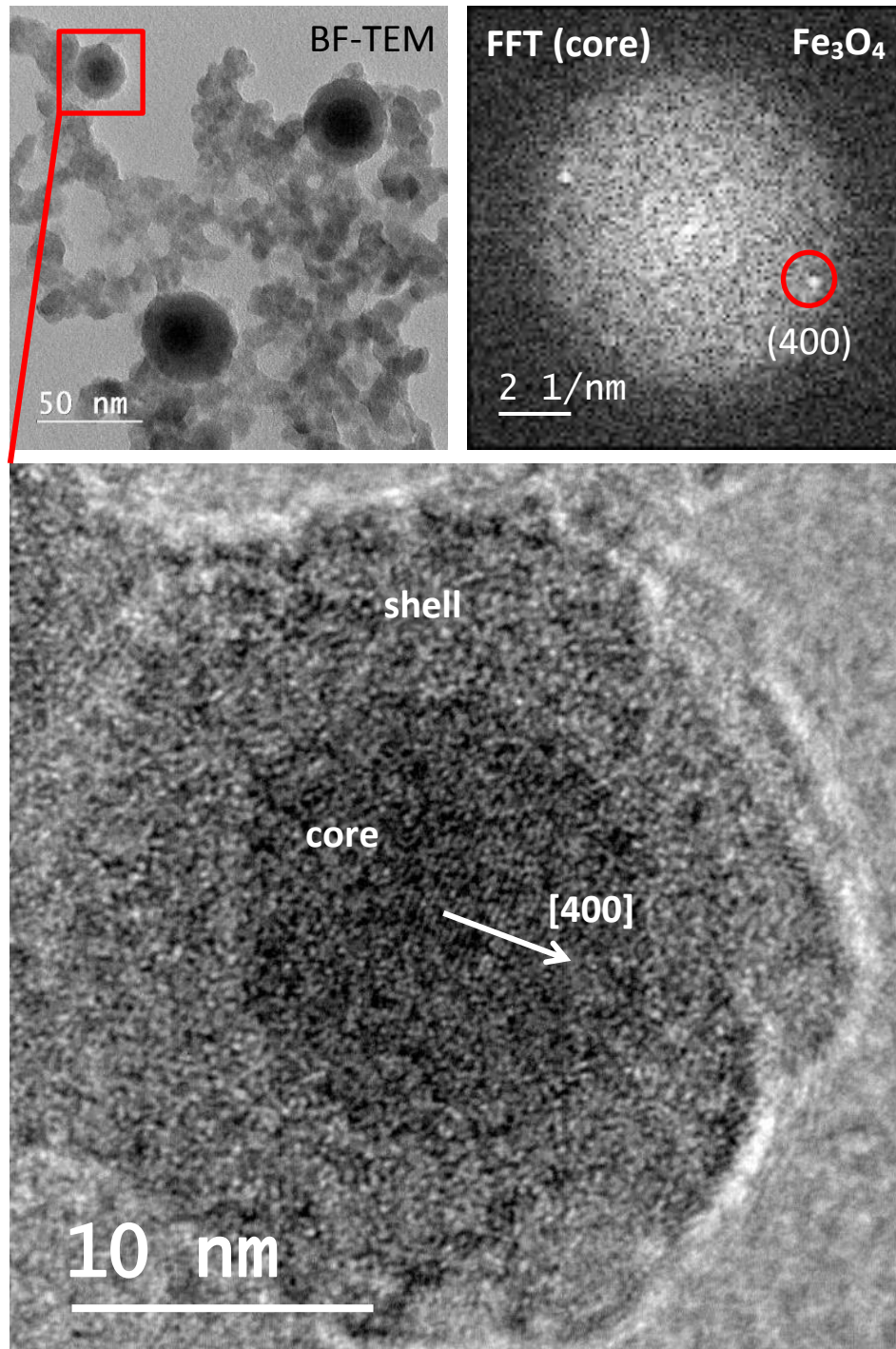


Figure 56: bright field images of sample B7 showing a core-shell-nanoparticle with a  $\text{Fe}_3\text{O}_4$  core in the [400] direction

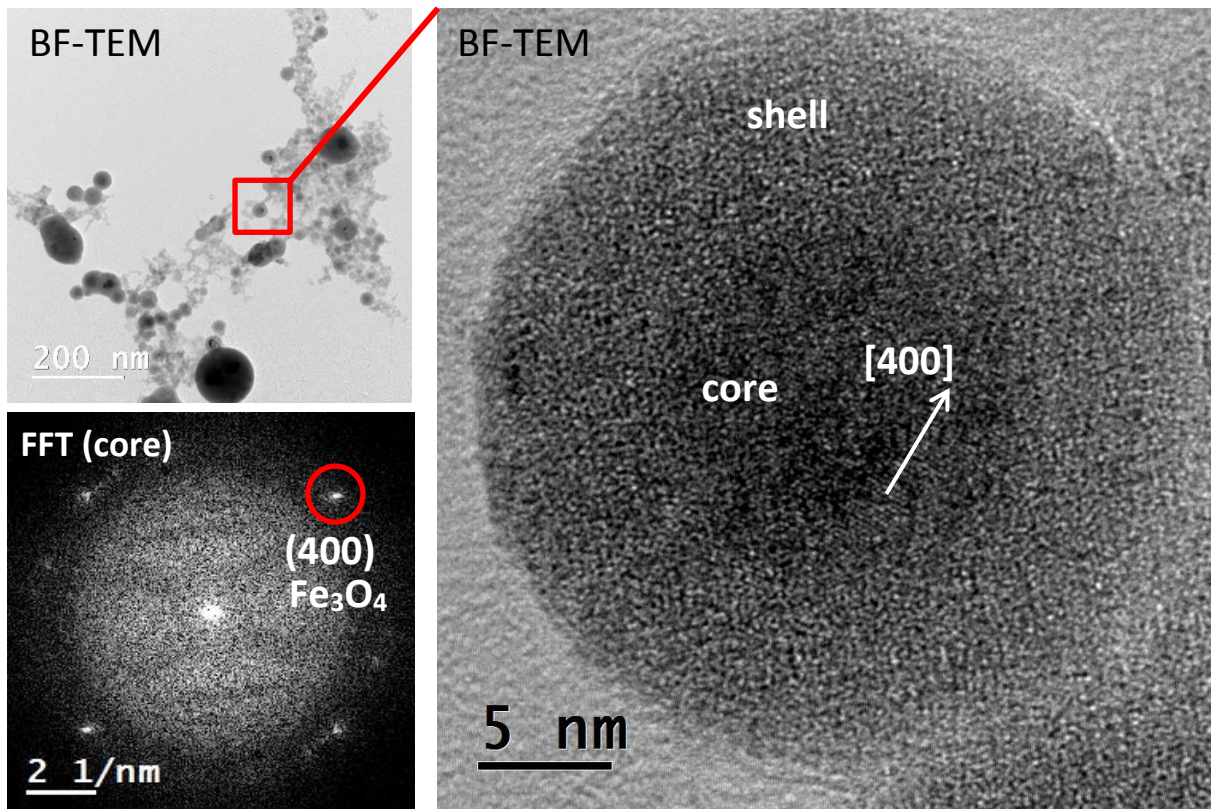


Figure 57: bright field images of sample B7 showing a core-shell-nanoparticle with a  $\text{Fe}_3\text{O}_4$  core in the  $[400]$  direction; FFT of the particle's core with the brightest spot identified as the  $(400)$  reflection of  $\text{Fe}_3\text{O}_4$

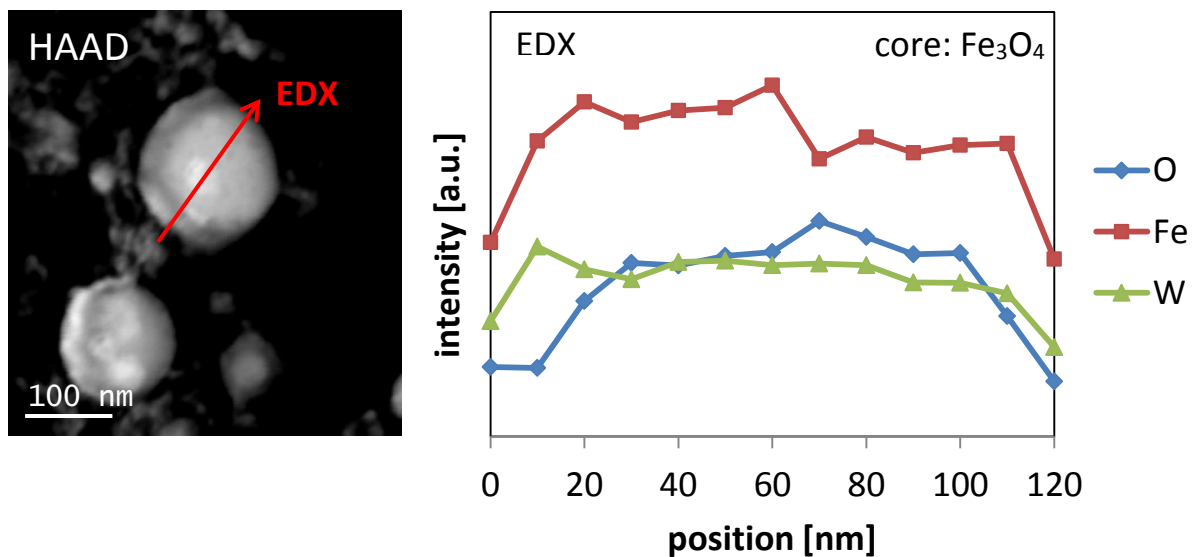


Figure 58: location of the performed EDX line scan on a nanoparticle of sample B7 (left); EDX line scan of the left particle assuming a  $\text{Fe}_x\text{O}_x$  core (right)

The determination of the microstructure of the shell proved difficult due to little chances to picture lattice planes. One of the few positive examples is given in figure 59. The lattice planes in the shell of this core/shell particle are very well visible and were assumed to be  $\text{WO}_3$  with the  $[110]$  and the  $[100]$  directions. According the previously shown EDX line scans some shells may also contain iron.

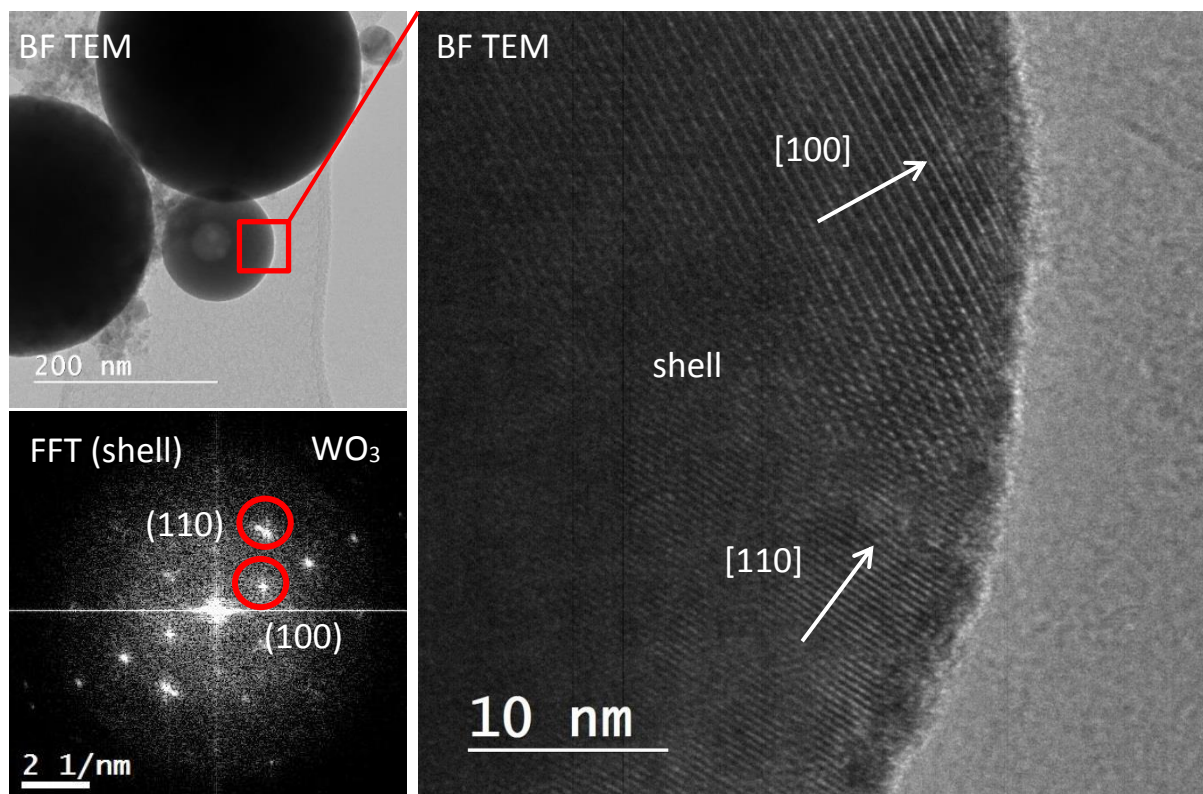


Figure 59: bright field images of sample B7 showing a core-shell-nanoparticle with an  $\text{WO}_3$  shell in the  $[100]$  and  $[110]$  directions; FFT of the particle's shell with spots identified as the  $(100)$  and  $(110)$  reflections of  $\text{WO}_3$

## 5 Discussion

### 5.1 Combining of Numerical and Experimental Results

The gained knowledge about the transition to superparamagnetic behaviour for various geometries and materials and the information about the investigated FeW nanoparticles is important for the explanation of the transition to superparamagnetism for magnetic nanoparticles used for biomedical applications such as magnetic hyperthermia. An overview of the obtained results from the micromagnetic simulations from chapter 3 is provided in table 26.

Material	Geometry	Initial/final state	Transition Diameter [nm]	Transition volume [nm <sup>3</sup> ]
Fe <sub>3</sub> O <sub>4</sub>	Sphere	[111]/[-111]	44	44602
		[-111]/[-11-1]	44	44602
		[-11-1]/[-1-1-1]	36	24429
		[111]/[-1-1-1]	26.5	9744
Fe	Sphere	[001]/[010]	19.5	3882
		[001]/[100]	17.5	2806
		[010]/[00-1]	20.5	4511
		[100]/[00-1]	20.5	4511
		[001]/[00-1]	16.5	2352
Fe <sub>3</sub> O <sub>4</sub>	Disc	[111]/[-111]	69	44871
		[-111]/[-11-1]	69	44871
		[-11-1]/[-1-1-1]	47	20819
		[111]/[-1-1-1]	29	7926

Table 26: Summary of received critical diameters and volumes for the transition to superparamagnetic behaviour of all simulated shapes and materials

With the knowledge about the transition diameters of Fe<sub>3</sub>O<sub>4</sub>- and Fe-spheres and the fact that the cores of the investigated particles are made both of Fe<sub>3</sub>O<sub>4</sub> and Fe, it is now possible to evaluate the amount of superparamagnetic nanoparticles in the sample sets (A) and (B). Assuming that the shell is non-magnetic because of finding the crystal structure of WO<sub>3</sub>, enables the calculation of the critical size for superparamagnetism by using the ratios between core diameters and particle diameters which are 0.48 for sample A1 and 0.51 for sample B7 (see chapter 4.5). Dividing the transition diameters by the mentioned ratio delivers the transition diameter for a FeW nanoparticle under which superparamagnetic behavior appears. For this issue, the transition diameters for a complete reversal is taken, therefore D=26.5 nm for a Fe<sub>3</sub>O<sub>4</sub>-core and D=16.5 nm for a Fe-core. Assuming that the nanospheres of sample set (A) have a similar crystal structure like the particles of sample set (B) leads to the following transition diameters for FeW nanoparticles (table 27).

	<i>Transition particle diameter (Fe<sub>3</sub>O<sub>4</sub>-core) [nm]</i>	<i>Transition particle diameter (Fe-core) [nm]</i>
<i>Sample A1</i>	55	34
<i>Sample B7</i>	52	32

Table 27: particle diameters for a transition to superparamagnetic behaviour for both samples A1 and B7

Using the size distributions determined for the samples A1 and B7 of chapter 4.5, the amount of superparamagnetic nanoparticles in these two samples is evaluated by connecting the transition particle diameters of table 27 to the size distributions. The amount of superparamagnetic nanoparticles depends on the ratio of Fe<sub>3</sub>O<sub>4</sub> cores to Fe cores which is unknown. Hence, the two extrema of only Fe<sub>3</sub>O<sub>4</sub> cores and only Fe cores are regarded, providing the minimally possible amount of superparamagnetic nanoparticles and the maximally possible amount of superparamagnetic nanoparticles. Consequently, for sample A1 the amount of superparamagnetic particles lies between 23% - 43%. For sample B7 the amount of superparamagnetic particles is between 37% - 71%. These relations are illustrated in figure 60.

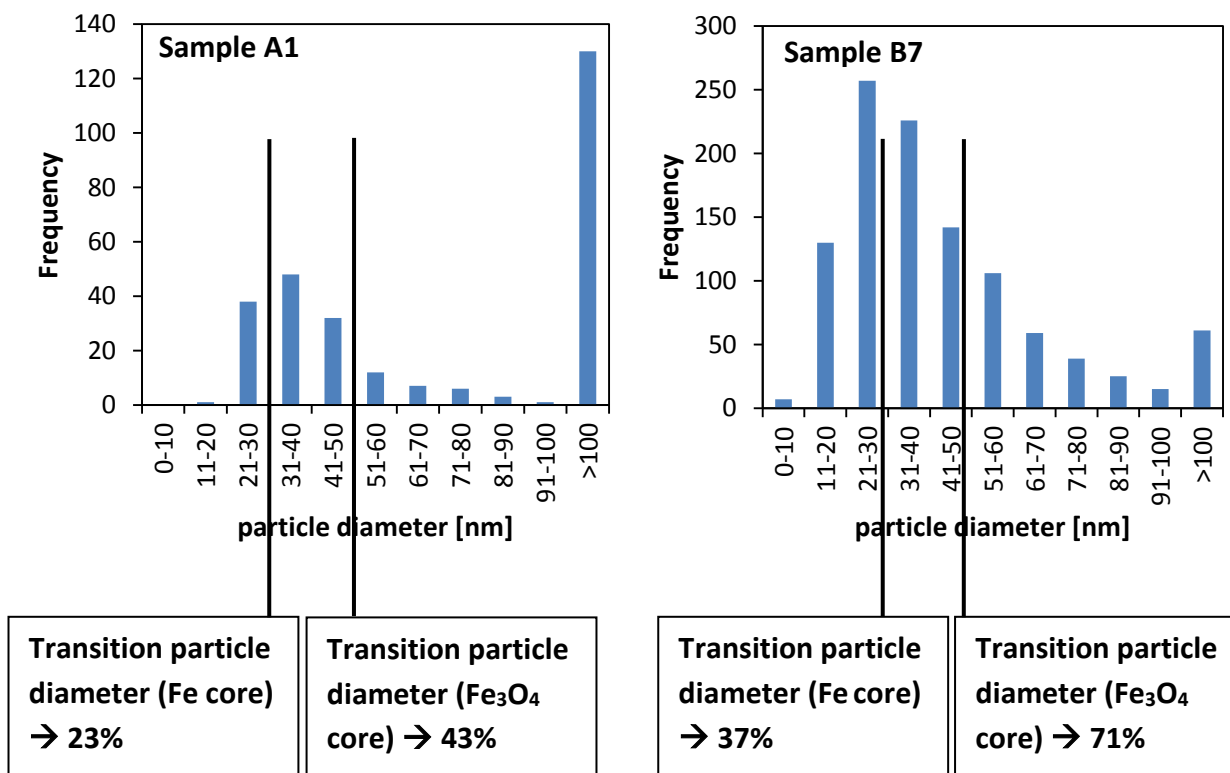


Figure 60: Size distributions of sample A1 and sample B7 and the labelling of the amount of superparamagnetic particles for the assumption of either only Fe<sub>3</sub>O<sub>4</sub> or Fe cores in the samples

## 5.2 Comparison of Fe<sub>3</sub>O<sub>4</sub>-Spheres and Fe<sub>3</sub>O<sub>4</sub>-Discs

According to formula (2) which states that the product of the magnetocrystalline anisotropy and the volume is a good approximation for the energy barrier, the numerically simulated spheres and discs made of magnetite should have similar transition volumes. Indeed, the comparison of the two geometries in table 28 shows similar values for the transition volume.

<i>Initial/Final state</i>	<i>Transition volume [nm<sup>3</sup>]</i>	
	<i>Fe<sub>3</sub>O<sub>4</sub> Sphere</i>	<i>Fe<sub>3</sub>O<sub>4</sub> Disc</i>
[111]/[-111]	44602	44871
[-111]/[-11-1]	44602	44871
[-11-1]/[-1-1-1]	24429	20819
[111]/[-1-1-1]	9744	7926

Table 28: Comparison of transition volumes for spheres and discs made of magnetite

## 5.3 Appearance of Incoherence for Fe<sub>20</sub>Ni<sub>80</sub>-Discs

As documented in chapter 3.4, even very small nanodiscs with a diameter of D=25 nm and a height of H=12 nm show incoherent behaviour at thermal magnetization reversal, if they are made of permalloy. Due to their possible application, these observation may offer several advantages. As stated, the produced nanodiscs of Tiberto et al. [41] have a height of H=30 nm and a diameter of D=650 nm. The magnetization reversal of these large nanodiscs is marked by magnetic vortex nucleation which makes them suitable for biomedical applications being detectable at relatively low-frequency, where they display a collective mode spin resonance excitation.

The fact that also smaller Fe<sub>20</sub>Ni<sub>80</sub>-nanodiscs show vortex nucleation which should also ensure the above mentioned detectability at low-frequency, enables the usage of smaller nanodiscs for biomedical applications. Permalloy nanodiscs with smaller dimensions could reduce the deposition in the tissue caused by gravitation. In addition, if desirable for a biomedical application, smaller nanodiscs could get through cell walls or similar tissue more easily.

## 6 Conclusions and Outlook

Summarizing, the TEM investigations explored two different types of nanoparticles, homogenous and core/shell nanospheres with very broad size distributions. Various high resolution and FFT analysis made it possible to identify two different core crystal structures,  $\text{Fe}_3\text{O}_4$  and  $\alpha\text{-Fe}$ . Also EDX and EELS measurements confirmed a high amount of Fe in the core. HRTEM indicated the shell's crystal structure to be  $\text{WO}_3$  which is non-magnetic.

At a defined time period between two switching processes by thermal activation of 100 seconds the micromagnetic simulations delivered the transition diameters to superparamagnetic behaviour for  $\text{Fe}_3\text{O}_4$  spheres ( $D=26.5$  nm), Fe spheres ( $D=16.5$  nm) and  $\text{Fe}_3\text{O}_4$  discs ( $D=29$  nm,  $H=12$  nm). Connecting the numerical and experimental results enabled the evaluation of the transition particle diameter for FeW nanoparticles to be 55 nm ( $\text{Fe}_3\text{O}_4$ -core) and 34 nm (Fe-core) for sample A1 and 52 nm ( $\text{Fe}_3\text{O}_4$ -core) and 32 nm (Fe-core) for sample B7. The amount of superparamagnetic particles lies between 23% - 43% for sample A1 and 37% - 71% for sample B7.

As the performed investigations have shown, superparamagnetism is a relevant phenomenon for nanoparticles in biomedical applications and therefore, has to be taken into account of. Regarding the work in this diploma thesis particularly, further investigation should be done focussing on the heat generation in the hyperthermia process and its frequency-dependence, to conclusively evaluate the ideal particle size and shape for efficient heating.

Generally speaking, to fully establish magnetic hyperthermia as a standard therapy for cancer treatment the consequences of superparamagnetic behaviour of magnetic nanoparticles has to be further investigated. Also, the search for a fabrication method to produce highly uniform nanoparticles with a clearly defined, narrow size distribution will be object of future research. The aim of research in magnetic nanoparticles in biomedical applications has to be to completely substitute treatments using toxics or damaging radiation with treatments in use of biocompatible and non-harming materials such as magnetite. Therefore, a profound understanding of the behaviour of magnetic nanoparticles under different circumstances is essential.



## 7 References

- [1] F. J. Heiligtag and M. Niederberger, “The fascinating world of nanoparticle research,” *Mater. Today*, vol. 16, no. 7–8, pp. 262–271, Jul. 2013.
- [2] M. Faraday, “The Bakerian Lecture: Experimental Relations of Gold (and Other Metals) to Light,” *Philos. Trans. R. Soc. Lond.*, vol. 147, no. 0, pp. 145–181, Jan. 1857.
- [3] H. Jarvie, “Nanoparticle,” *Encyclopaedia Britannica* <https://www.britannica.com/science/nanoparticle> July 7, 2016.
- [4] D. Frick and H. K. Pulker, “Easy-to-clean Schichten – spezielle Anwendungen,” *Vak. Forsch. Prax.*, vol. 18, no. 2, pp. 16–19, Apr. 2006.
- [5] M. Jaffe, G. Collins, and J. Menczel, “The thermal analysis of fibers in the twenty first century: From textile, industrial and composite to nano, bio and multi-functional,” *Thermochim. Acta*, vol. 442, no. 1–2, pp. 95–99, Mar. 2006.
- [6] P.-J. Lu, S.-C. Huang, Y.-P. Chen, L.-C. Chiueh, and D. Y.-C. Shih, “Analysis of titanium dioxide and zinc oxide nanoparticles in cosmetics,” *J. Food Drug Anal.*, vol. 23, no. 3, pp. 587–594, Sep. 2015.
- [7] K. Hossain and S. Rameeja, “Importance of Nanotechnology in Civil Engineering,” *Eur. J. Sustain. Dev.*, vol. 4, no. 1, pp. 161–166, Feb. 2015.
- [8] R. Wiltschko and W. Wiltschko, “Magnetoreception,” in *Sensing in Nature*, vol. 739, C. López-Larrea, Ed. New York, NY: Springer US, 2012, pp. 126–141.
- [9] R. Blakemore, “Magnetotactic bacteria,” *Science*, vol. 190, no. 4212, pp. 377–379, Oct. 1975.
- [10] J. L. Kirschvink, M. M. Walker, and C. E. Diebel, “Magnetite-based magnetoreception,” *Curr. Opin. Neurobiol.*, vol. 11, no. 4, pp. 462–467, Aug. 2001.
- [11] A. Muxworthy, “Magnetotactic Bacteria,” Imperial College London <http://www.imperial.ac.uk/people/adrian.muxworthy/research.html> July 7, 2016.
- [12] S. Toraya-Brown, M. R. Sheen, P. Zhang, L. Chen, J. R. Baird, E. Demidenko, M. J. Turk, P. J. Hoopes, J. R. Conejo-Garcia, and S. Fiering, “Local hyperthermia treatment of tumors induces CD8+ T cell-mediated resistance against distal and secondary tumors,” *Nanomedicine Nanotechnol. Biol. Med.*, vol. 10, no. 6, pp. 1273–1285, Aug. 2014.
- [13] J. A. Nagy, S.-H. Chang, A. M. Dvorak, and H. F. Dvorak, “Why are tumour blood vessels abnormal and why is it important to know?,” *Br. J. Cancer*, vol. 100, no. 6, pp. 865–869, Mar. 2009.
- [14] K. Sugimachi, H. Matsuda, S. Ohno, A. Fukuda, H. Matsuoka, M. Mori, and H. Kuwano, “Long-term effects of hyperthermia combined with chemotherapy and irradiation for the treatment of patients with carcinoma of the esophagus,” *Surg. Gynecol. Obstet.*, vol. 167, no. 4, pp. 319–323, Oct. 1988.
- [15] C. W. Song, H. J. Park, C. K. Lee, and R. Griffin, “Implications of increased tumor blood flow and oxygenation caused by mild temperature hyperthermia in tumor treatment,” *Int. J. Hyperth. Off. J. Eur. Soc. Hyperthermic Oncol. North Am. Hyperth. Group*, vol. 21, no. 8, pp. 761–767, Dec. 2005.
- [16] H. I. Robins, “Whole body hyperthermia (41–42 °C): A simple technique for unanesthetized mice,” *Med. Phys.*, vol. 11, no. 6, p. 833, 1984.
- [17] M. Bañobre-López, A. Teijeiro, and J. Rivas, “Magnetic nanoparticle-based hyperthermia for cancer treatment,” *Rep. Pract. Oncol. Radiother.*, vol. 18, no. 6, pp. 397–400, Nov. 2013.
- [18] A. Kolhatkar, A. Jamison, D. Litvinov, R. Willson, and T. Lee, “Tuning the Magnetic Properties of Nanoparticles,” *Int. J. Mol. Sci.*, vol. 14, no. 8, pp. 15977–16009, Jul. 2013.
- [19] A. E. Deatsch and B. A. Evans, “Heating efficiency in magnetic nanoparticle hyperthermia,” *J. Magn. Magn. Mater.*, vol. 354, pp. 163–172, Mar. 2014.

- [20] R. Ramprasad, P. Zurcher, M. Petras, M. Miller, and P. Renaud, "Magnetic properties of metallic ferromagnetic nanoparticle composites," *J. Appl. Phys.*, vol. 96, no. 1, p. 519, 2004.
- [21] "Fighting cancer more effectively and with fewer side effects." Retrieved from <http://www.magforce.de/en/produkte/nanothermr-therapie.html> (2016, May 25).
- [22] "Brain tumour localisation and destruction facilitated by gadolinium-based nanoparticles in microbeam radiation therapy." (2012, June 21). Retrieved from [http://www.esrf.eu/news/spotlight/spotlight162/index\\_html](http://www.esrf.eu/news/spotlight/spotlight162/index_html) (2016, May 25).
- [23] A. Senyei, K. Widder, and G. Czerlinski, "Magnetic guidance of drug-carrying microspheres," *J. Appl. Phys.*, vol. 49, no. 6, p. 3578, 1978.
- [24] S. C. McBain, H. H. P. Yiu, and J. Dobson, "Magnetic nanoparticles for gene and drug delivery," *Int. J. Nanomedicine*, vol. 3, no. 2, pp. 169–180, 2008.
- [25] T. Kubo, T. Sugita, S. Shimose, Y. Nitta, Y. Ikuta, and T. Murakami, "Targeted delivery of anticancer drugs with intravenously administered magnetic liposomes in osteosarcoma-bearing hamsters.," *Int. J. Oncol.*, Aug. 2000.
- [26] M. Colombo, S. Carregal-Romero, M. F. Casula, L. Gutiérrez, M. P. Morales, I. B. Böhm, J. T. Heverhagen, D. Prospero, and W. J. Parak, "Biological applications of magnetic nanoparticles," *Chem. Soc. Rev.*, vol. 41, no. 11, p. 4306, 2012.
- [27] T.K. Indira and P.K. Lakshmi, "Magnetic Nanoparticles - A Review," *Int. J. Pharm. Sci. Nanotechnol.*, vol. 3, pp. 1035–1042, 2010.
- [28] V. Melfos, B. Helly, and P. Voudouris, "The ancient Greek names 'Magnesia' and 'Magnetes' and their origin from the magnetite occurrences at the Mavrovouni mountain of Thessaly, central Greece. A mineralogical–geochemical approach," *Archaeol. Anthropol. Sci.*, vol. 3, no. 2, pp. 165–172, Jun. 2011.
- [29] J. Vardalas, "A History of the Magnetic Compass," *IEEE*, Nov. 2013.
- [30] M. Bellis, "The Compass and other Magnetic Innovations," *About.com*, Dec. 2014.
- [31] K. D. Sattler, Ed., *Handbook of nanophysics. Nanomedicine and nanorobotics*. Boca Raton: Taylor & Francis, 2011.
- [32] M. Mahmoudi, S. Sant, B. Wang, S. Laurent, and T. Sen, "Superparamagnetic iron oxide nanoparticles (SPIONs): Development, surface modification and applications in chemotherapy," *Adv. Drug Deliv. Rev.*, vol. 63, no. 1–2, pp. 24–46, Jan. 2011.
- [33] M. Koneracká, P. Kopčanský, M. Timko, C. . Ramchand, A. de Sequeira, and M. Trevan, "Direct binding procedure of proteins and enzymes to fine magnetic particles," *J. Mol. Catal. B Enzym.*, vol. 18, no. 1–3, pp. 13–18, Sep. 2002.
- [34] C. Alexiou, W. Arnold, R. J. Klein, F. G. Parak, P. Hulin, C. Bergemann, W. Erhardt, S. Wagenpfeil, and A. S. Lübke, "Locoregional cancer treatment with magnetic drug targeting," *Cancer Res.*, vol. 60, no. 23, pp. 6641–6648, Dec. 2000.
- [35] B. Polyak and G. Friedman, "Magnetic targeting for site-specific drug delivery: applications and clinical potential," *Expert Opin. Drug Deliv.*, vol. 6, no. 1, pp. 53–70, Jan. 2009.
- [36] C. H. Cunningham, T. Arai, P. C. Yang, M. V. McConnell, J. M. Pauly, and S. M. Conolly, "Positive contrast magnetic resonance imaging of cells labeled with magnetic nanoparticles," *Magn. Reson. Med.*, vol. 53, no. 5, pp. 999–1005, May 2005.
- [37] J. Meng, J. Fan, G. Galiana, R. T. Branca, P. L. Clasen, S. Ma, J. Zhou, C. Leuschner, C. S. S. R. Kumar, J. Hormes, T. Otit, A. C. Beye, M. P. Harmer, C. J. Kiely, W. Warren, M. P. Haataja, and W. O. Soboyejo, "LHRH-functionalized superparamagnetic iron oxide nanoparticles for breast cancer targeting and contrast enhancement in MRI," *Mater. Sci. Eng. C*, vol. 29, no. 4, pp. 1467–1479, May 2009.
- [38] R.L. Kahn, *Serum Diagnosis for Syphilis*. In *Colloidal Chemistry*. J. Alexander, Ed. New York, 1928.

- [39] L. Dykman and N. Khlebtsov, “Gold nanoparticles in biomedical applications: recent advances and perspectives,” *Chem Soc Rev*, vol. 41, no. 6, pp. 2256–2282, 2012.
- [40] R. Das, J. Alonso, Z. Nematı Porshokouh, V. Kalappattıl, D. Torres, M.-H. Phan, E. Garaio, J. Á. García, J. L. Sanchez Llamazares, and H. Srikanth, “Tunable High Aspect Ratio Iron Oxide Nanorods for Enhanced Hyperthermia,” *J. Phys. Chem. C*, vol. 120, no. 18, pp. 10086–10093, May 2016.
- [41] P. Tiberto, G. Barrera, F. Celegato, G. Conta, M. Coisson, F. Vinai, and F. Albertini, “Ni<sub>80</sub>Fe<sub>20</sub> nanodisks by nanosphere lithography for biomedical applications,” *J. Appl. Phys.*, vol. 117, no. 17, p. 17B304, May 2015.
- [42] C. Martinez-Boubeta, K. Simeonidis, A. Makridis, M. Angelakeris, O. Iglesias, P. Guardia, A. Cabot, L. Yedra, S. Estradé, F. Peiró, Z. Saghi, P. A. Midgley, I. Conde-Leborán, D. Serantes, and D. Baldomir, “Learning from Nature to Improve the Heat Generation of Iron-Oxide Nanoparticles for Magnetic Hyperthermia Applications,” *Sci. Rep.*, vol. 3, Apr. 2013.
- [43] G. Zhen, B. W. Muir, B. A. Moffat, P. Harbour, K. S. Murray, B. Moubaraki, K. Suzuki, I. Madsen, N. Agron-Olshina, L. Waddington, P. Mulvaney, and P. G. Hartley, “Comparative Study of the Magnetic Behavior of Spherical and Cubic Superparamagnetic Iron Oxide Nanoparticles,” *J. Phys. Chem. C*, vol. 115, no. 2, pp. 327–334, Jan. 2011.
- [44] E. A. Sykes, Q. Dai, K. M. Tsoi, D. M. Hwang, and W. C. W. Chan, “Nanoparticle exposure in animals can be visualized in the skin and analysed via skin biopsy,” *Nat. Commun.*, vol. 5, May 2014.
- [45] C. P. Bean and J. D. Livingston, “Superparamagnetism,” *J. Appl. Phys.*, vol. 30, no. 4, p. S120, 1959.
- [46] L. Néel and N. Kurti, *Selected works of Louis Néel: translation from the French authorized by the Centre national de la recherche scientifique*. New York: Gordon and Breach, 1988.
- [47] P. Toson, “Multiscale Modelling of Advanced Hard Magnets,” Institut für Festkörperphysik, Technische Universität, Wien, 2015.
- [48] L. D. Landau and E. M. Lifshitz, *Theory of the dispersion of magnetic permeability in ferromagnetic bodies*. Phys. Z. Sowietunion, 1935.
- [49] T. L. Gilbert, “Abstracts of Papers to be Presented at the 1955 Thanksgiving Meeting at the University of Chicago, Chicago, Illinois, November 25 and 26, 1955,” *Phys. Rev.*, vol. 100, no. 4, pp. 1235–1235, Nov. 1955.
- [50] Stoner E.C. and Wohlfarth E.P., “A Mechanism of Magnetic Hysteresis in Heterogenous Alloys,” *Philosophical Transactions of the Royal Society of London*, vol. A240, pp. 599–642, 1948.
- [51] J. Fidler and T. Schrefl, “Micromagnetic modelling-the current state of the art,” *Journal of Physics D: Applied Physics* 33 (15), R135, 2000.
- [52] “GID 12.0.7,” [http://www.gidhome.com/ftp/pub/GiD\\_Official\\_Versions/Windows/win-x64/64bit](http://www.gidhome.com/ftp/pub/GiD_Official_Versions/Windows/win-x64/64bit).
- [53] H. Kronmüller, *Magnetisierungskurve der Ferromagnetika*, vol. 2. Berlin: Ed. A. Seeger, Springer-Verlag, p.52, 1966.
- [54] V. Tsiantos, W. Scholz, D. Suess, T. Schrefl, and J. Fidler, “The effect of the cell size in Langevin micromagnetic simulations,” *J. Magn. Magn. Mater.*, vol. 242–245, pp. 999–1001, Apr. 2002.
- [55] E. Kneller, *Ferromagnetismus*. Berlin/Göttingen/Heidelberg: Springer, p.190, 1962.
- [56] J. M. D. Coey, *Magnetism and magnetic materials*. Cambridge; New York: Cambridge University Press, p.247-249, p.596-597, 2009.
- [57] R. Skomski, *Simple models of magnetism*. Oxford; New York: Oxford University Press, p.313, 2008.
- [58] “ParaView 4.2.0,” <http://www.paraview.org/download>, Oct. 2014.

- [59] W. Scholz, J. Fidler, T. Schrefl, D. Suess, R. Dittrich, H. Forster, and V. Tsiantos, "Scalable parallel micromagnetic solvers for magnetic nanostructures," *Comput. Mater. Sci.*, vol. 28, no. 2, pp. 366–383, Oct. 2003.
- [60] R. Dittrich, T. Schrefl, D. Suess, W. Scholz, H. Forster, and J. Fidler, "A path method for finding energy barriers and minimum energy paths in complex micromagnetic systems," *J. Magn. Magn. Mater.*, vol. 250, pp. 12–19, Sep. 2002.
- [61] G. Henkelman and H. Jónsson, "Improved tangent estimate in the nudged elastic band method for finding minimum energy paths and saddle points," *J. Chem. Phys.*, vol. 113, no. 22, p. 9978, 2000.
- [62] Fleur Burrows, "A Model of Magnetic Hyperthermia." University of York, Department of Physics, Mar-2012.
- [63] I. Baker, Q. Zeng, W. Li, and C. R. Sullivan, "Heat deposition in iron oxide and iron nanoparticles for localized hyperthermia," *J. Appl. Phys.*, vol. 99, no. 8, p. 08H106, 2006.
- [64] V. Novosad, F. Y. Fradin, P. E. Roy, K. S. Buchanan, K. Y. Guslienko, and S. D. Bader, "Magnetic vortex resonance in patterned ferromagnetic dots," *Phys. Rev. B*, vol. 72, no. 2, Jul. 2005.
- [65] M. Dell'Aglio, R. Gaudio, O. De Pascale, and A. De Giacomo, "Mechanisms and processes of pulsed laser ablation in liquids during nanoparticle production," *Appl. Surf. Sci.*, vol. 348, pp. 4–9, Sep. 2015.
- [66] K. Sasaki and N. Takada, "Liquid-phase laser ablation," *Pure Appl. Chem.*, vol. 82, no. 6, Jan. 2010.
- [67] K. Momma and F. Izumi, "VESTA 3 for three-dimensional visualization of crystal, volumetric and morphology data," *J. Appl. Crystallogr.*, vol. 44, no. 6, pp. 1272–1276, Dec. 2011.
- [68] N. Mattern, W. X. Zhang, S. Roth, H. Reuther, C. Baetz, and M. Richter, "Structural and magnetic properties of non-stoichiometric  $\text{Fe}_2\text{Zr}$ ," *J. Phys. Condens. Matter*, vol. 19, no. 37, p. 376202, Sep. 2007.
- [69] G. Beskow, "V. M. Goldschmidt: Geochemische Verteilungsgesetze der Elemente," *Geol. Foereningan Stockh. Foerhandlingar*, vol. 46, no. 6–7, pp. 738–743, Dec. 1924.
- [70] N. Pailhé, J. Majimel, S. Pechev, P. Gravereau, M. Gaudon, and A. Demourgues, "Investigation of Nanocrystallized  $\alpha\text{-Fe}_2\text{O}_3$  Prepared by a Precipitation Process," *J. Phys. Chem. C*, vol. 112, no. 49, pp. 19217–19223, Dec. 2008.
- [71] A. Sawaoka and N. Kawai, "The Effect of Hydrostatic Pressure on the Magnetic Anisotropy of Ferrous and Ferric Ions in Ferrites with Spinel Structure," *J. Phys. Soc. Jpn.*, vol. 25, no. 1, pp. 133–140, Jul. 1968.
- [72] X. D. Dai, Y. Kong, J. H. Li, and B. X. Liu, "Extended Finnis–Sinclair potential for bcc and fcc metals and alloys," *J. Phys. Condens. Matter*, vol. 18, no. 19, pp. 4527–4542, May 2006.
- [73] D. J. Palmer and P. G. Dickens, "Tungsten dioxide: structure refinement by powder neutron diffraction," *Acta Crystallogr. B*, vol. 35, no. 9, pp. 2199–2201, Sep. 1979.
- [74] B. Gerand, G. Nowogrocki, J. Guenot, and M. Figlarz, "Structural study of a new hexagonal form of tungsten trioxide," *J. Solid State Chem.*, vol. 29, no. 3, pp. 429–434, Sep. 1979.

## 8 List of Figures

Figure 1: The Lycurgus Cup in reflected (left) and in transmitted (right) light.....	1
Figure 2: Magnetotactic bacteria containing chains of magnetic crystals [11].....	2
Figure 3: MRI images of rat brain glioma before and.....	5
Figure 4: Possible design for a drug delivering nanoparticle [24].....	6
Figure 5: Iron-oxide nanocubes (a) with average edge length of 20.5 nm; inset reveals 2D self-assembly arrangements. (b) Corresponding TEM micrograph of 40 nm nanocubes: Observation of chain-like configurations [40].....	9
Figure 6: Anisotropy type depending on the uniaxial constants $K_1$ and $K_2$ [46].....	14
Figure 7: Easy, intermediate and hard axes in dependence on the cubic anisotropy constants $K_1$ and $K_2$ [46].....	14
Figure 8: Damped magnetization precession.....	16
Figure 9: Stoner-Wohlfarth particle (rotational ellipsoid).....	17
Figure 10: Magnetization curves for the Stoner-Wohlfarth model for various angles $\alpha$ .....	18
Figure 11: Sphere with a diameter of 25 nm before (left) and after meshing (right) in GID... ..	19
Figure 12: values for the coercivity $H_c$ delivered from numerical simulations at different mesh sizes; the smaller the mesh size the more accurate and stable the result for the coercivity $H_c$ .....	21
Figure 13: Cut-out of a master.par file for field magnetization reversal performed by FEMME.....	23
Figure 14: Exemplary hysteresis curve of a Fe-Sphere with a diameter of 25 nm.....	24
Figure 15: Visualization of the basic idea of the nudged elastic band method [50].....	25
Figure 16: Modells of simulated magnetite nanospheres ranging from diameter $D=5\text{nm}$ up to $D=100\text{nm}$ (designed with GID); the mesh size was scaled down from $D=100\text{nm}$ with the geometry size.....	26
Figure 17: field magnetization reversal from the [111] to the [-1-1-1] direction of a $\text{Fe}_3\text{O}_4$ nanosphere with $D=50\text{ nm}$ ; coherent switching behaviour.....	27
Figure 18: field magnetization reversal from the [111] to the [-1-1-1] direction of a $\text{Fe}_3\text{O}_4$ nanosphere with $D=100\text{ nm}$ ; incoherent switching behaviour.....	28
Figure 19: thermal magnetization reversal of the $D=50\text{ nm}$ $\text{Fe}_3\text{O}_4$ nanosphere from the [111] to the [-111] direction showing only coherent switching behaviour.....	29
Figure 20: thermal magnetization reversal of the $D=100\text{ nm}$ $\text{Fe}_3\text{O}_4$ nanosphere from the [111] to the [-111] direction showing vortex formation.....	30
Figure 21: MEPs for the transition from the [111] to the [-111] direction of $\text{Fe}_3\text{O}_4$ ; the images are arranged according to rising diameter/volume.....	31
Figure 22: Relation between transition diameter/transition volume and energy barrier revealing when superparamagnetic behaviour appears for a $\text{Fe}_3\text{O}_4$ nanosphere; the red curve corresponds to the primary x-axis (diameter) and the blue curve corresponds to the secondary x-axis (volume).....	32
Figure 23: Modells of simulated iron nanospheres ranging from diameter $D=5\text{nm}$ up to $D=100\text{ nm}$ (designed with GID); the mesh size was scaled down from $D=100\text{ nm}$ with the geometry size.....	33

Figure 24: field magnetization reversal from the [001] to the [00-1] easy direction of iron nanospheres with D=25 nm (upper graph) and with D=50 nm (lower graph); transition from coherent to incoherent switching behaviour.....	34
Figure 25: thermal magnetization reversal of the D=25 nm Fe nanosphere from the [001] to the [010] direction showing only coherent switching behaviour .....	35
Figure 26: thermal magnetization reversal of the D=50 nm Fe nanosphere from the [001] to the [010] direction showing vortex formation.....	36
Figure 27: Relation between transition diameter/transition volume and energy barrier revealing when superparamagnetic behaviour appears for an iron nanosphere; the red curve corresponds to the primary x-axis (diameter) and the blue curve corresponds to the secondary x-axis (volume) .....	37
Figure 28: Modells of simulated Fe <sub>3</sub> O <sub>4</sub> nanodiscs ranging from diameter D=25 nm up to D=200 nm at a constant height of H=12 nm (designed with GID) .....	38
Figure 29: field magnetization reversal from the [111] to the [-1-1-1] easy direction of Fe <sub>3</sub> O <sub>4</sub> nanodiscs with D=25 nm (upper graph) and with D=200 nm (lower graph), both at a constant height of H=12 nm; both show incoherent switching behaviour which is also proved by the additional pictures in the graphs.....	39
Figure 30: thermal magnetization reversal of the D=200 nm Fe <sub>3</sub> O <sub>4</sub> nanodisc from the [111] to the [-111] direction showing only coherent switching behaviour .....	40
Figure 31: Relation between transition diameter/transition volume and energy barrier revealing when superparamagnetic behaviour appears for a Fe <sub>3</sub> O <sub>4</sub> nanodisc; the red curve corresponds to the primary x-axis (diameter) and the blue curve corresponds to the secondary x-axis (volume) .....	41
Figure 32: (a) deposition of Fe <sub>20</sub> Ni <sub>80</sub> ; (b) deposition of polystyrene nanospheres; (c) shrinking of nanospheres by etching; (d) removing Fe <sub>20</sub> Ni <sub>80</sub> by etching; (e) nanosphere removal by sonication; (f) dissolution of optical resist using acetone .....	42
Figure 33: Modells of simulated permalloy nanodiscs ranging from diameter D=25 nm up to D=200 nm with a constant height of H=12 nm (designed with GID).....	43
Figure 34: field magnetization reversal from the [001] to the [00-1] easy direction of Fe <sub>20</sub> Ni <sub>80</sub> nanodisc with D=100 nm and a constant height of H=12 nm; vortex formation.....	43
Figure 35: thermal magnetization reversal of the D=25 nm Fe <sub>20</sub> Ni <sub>80</sub> nanodisc (upper graph) and the D=200 nm Fe <sub>20</sub> Ni <sub>80</sub> nanodisc (lower graph) from the [001] to the [100] direction; all simulated models show incoherent switching behaviour .....	44
Figure 36: experimental setup for laser ablation in liquid (University of Vienna) .....	46
Figure 37: Time sequence of laser ablation in a liquid [58].....	46
Figure 38: (a) section of a ring with a copper grid and lacey carbon film on the grid;.....	47
Figure 39: unit cell of $\alpha$ -Fe.....	49
Figure 40: unit cell of FeO .....	49
Figure 41: unit cell of Fe <sub>2</sub> O <sub>3</sub> .....	50
Figure 42: unit cell of Fe <sub>3</sub> O <sub>4</sub> .....	50
Figure 43: unit cell of W .....	51
Figure 44: unit cell of WO <sub>2</sub> .....	51
Figure 45: unit cell of WO <sub>3</sub> .....	51
Figure 46: Illustration of a core/shell structure and term definitions .....	52

Figure 47: TEM bright field image of sample A1: very large nanoparticles with broad size distribution of spherical homogenous or core/shell particles .....	53
Figure 48: (a) size distribution of the 278 measured nanoparticles of sample A1: average particle diameter of 157 nm; .....	53
Figure 49: TEM bright field image of sample B7: broad size distribution with small nanoparticles.....	54
Figure 50: (a) size distribution of the 1067 measured nanoparticles of sample B7: average particle diameter of 44 nm; .....	54
Figure 51: nanoparticle with core/shell structure (left); nanoparticle with a homogenous structure (right).....	55
Figure 52: bright field images of sample B7 showing a core-shell-nanoparticle with an $\alpha$ -Fe core in the [110] direction; FFT of the particle's core with the brightest spot identified as the (110) reflection of $\alpha$ -Fe .....	56
Figure 53: (a) location of the performed EDX line scan and the two EDX spots on a nanoparticle of sample B7; (b) EDX line scan of the above particle assuming an $\alpha$ -Fe containing core .....	56
Figure 54: (a) EDX spot of the nanoparticle's core in figure 53 showing a high amount of iron; (b) EDX spot of the nanoparticle's shell in figure 53 indicating to a lower amount of iron and a higher amount of tungsten and oxygen in the shell than in the core .....	57
Figure 55: STEM image in HAADF mode of a core/shell nanoparticle (left); measured EELS intensity spectrum of the left particle with rising iron and dropping tungsten and oxygen in the core (right).....	58
Figure 56: bright field images of sample B7 showing a core-shell-nanoparticle with a $\text{Fe}_3\text{O}_4$ core in the [400] direction .....	59
Figure 57: bright field images of sample B7 showing a core-shell-nanoparticle with a $\text{Fe}_3\text{O}_4$ core in the [400] direction; FFT of the particle's core with the brightest spot identified as the (400) reflection of $\text{Fe}_3\text{O}_4$ .....	60
Figure 58: location of the performed EDX line scan on a nanoparticle of sample B7 (left); ..	60
Figure 59: bright field images of sample B7 showing a core-shell-nanoparticle with an $\text{WO}_3$ shell in the [100] and [110] directions; FFT of the particle's shell with spots identified as the (100) and (110) reflections of $\text{WO}_3$ .....	61
Figure 60: Size distributions of sample A1 and sample B7 and the labelling of the amount of superparamagnetic particles for the assumption of either only $\text{Fe}_3\text{O}_4$ or Fe cores in the samples .....	63

## 9 List of Tables

Table 1: material parameters of Fe, Fe <sub>3</sub> O <sub>4</sub> and Fe <sub>20</sub> Ni <sub>80</sub> used for the numerical micromagnetic simulations .....	20
Table 2: Calculated exchange lengths for the three simulated materials Fe, Fe <sub>3</sub> O <sub>4</sub> and Fe <sub>20</sub> Ni <sub>80</sub> .....	20
Table 3: mesh sizes for the simulated geometries; the spheres were drawn with a diameter of 100 nm and scaled down to smaller diameters .....	22
Table 4: output from GID; information of the finite element grid.....	22
Table 5: diameters and correlating volumes .....	27
Table 6: Simulated energy paths from one easy .....	29
Table 7: Summary of all transition diameters and corresponding transition volumes of different magnetization reversals for nanospheres made of magnetite .....	33
Table 8: diameters and correlating volumes .....	33
Table 9: Simulated energy paths from one easy .....	35
Table 10: Summary of all transition diameters and corresponding transition volumes of different magnetization reversals for nanospheres made of iron .....	36
Table 11: height, diameters and correlating volumes.....	38
Table 12: Simulated energy paths from one easy .....	40
Table 13: Summary of all transition diameters and corresponding transition volumes of different magnetization reversals for nanodiscs made of Fe <sub>3</sub> O <sub>4</sub> .....	41
Table 14: Dimensions of simulated Fe <sub>20</sub> Ni <sub>80</sub> nanodiscs.....	43
Table 15: Preparation parameters for both sample sets (A) and (B).....	48
Table 16: List of expectable phases .....	48
Table 17: possible crystal structures and lattice parameters for the prepared nanoparticles ...	49
Table 18: atomic positions of $\alpha$ -Fe.....	49
Table 19: atomic positions of FeO .....	49
Table 20: atomic positions of Fe <sub>2</sub> O <sub>3</sub> .....	50
Table 21: atomic positions of Fe <sub>3</sub> O <sub>4</sub> .....	50
Table 22: atomic positions of W .....	51
Table 23: atomic positions of WO <sub>2</sub> .....	51
Table 24: atomic positions of WO <sub>3</sub> .....	51
Table 25: Amount of analyzed particle diameters.....	52
Table 26: Summary of received critical diameters and volumes for the transition to superparamagnetic behaviour of all simulated shapes and materials.....	62
Table 27: particle diameters for a transition to superparamagnetic behaviour for both samples A1 and B7.....	63
Table 28: Comparison of transition volumes for spheres and discs made of magnetite .....	64



# 10 Appendix

## 10.1 hkl Tables

### $\alpha$ -Fe

<b>h</b>	<b>k</b>	<b>l</b>	<b>d<sup>-1</sup> [nm<sup>-1</sup>]</b>	<b>d [nm]</b>	<b>Intensity</b>	<b>Multiplicity</b>	<b>Extinction length [nm]</b>
1	1	0	4.934	0.203	1000.00	12	36.758
2	0	0	6.978	0.143	167.00	6	53.420
2	1	1	8.547	0.117	329.00	24	68.831
2	2	0	9.869	0.101	95.00	12	84.426

### FeO

<b>h</b>	<b>k</b>	<b>l</b>	<b>d<sup>-1</sup> [nm<sup>-1</sup>]</b>	<b>d [nm]</b>	<b>Intensity</b>	<b>Multiplicity</b>	<b>Extinction length [nm]</b>
1	1	1	4.056	0.247	361.00	8	84.507
2	0	0	4.684	0.214	1000.00	6	40.937
2	2	0	6.624	0.151	693.00	12	58.475
3	1	1	7.767	0.129	137.00	24	171.526
2	2	2	8.113	0.123	227.00	8	75.392
4	0	0	9.368	0.107	98.00	6	92.607

### Fe<sub>3</sub>O<sub>4</sub>

<b>h</b>	<b>k</b>	<b>l</b>	<b>d<sup>-1</sup> [nm<sup>-1</sup>]</b>	<b>d [nm]</b>	<b>Intensity</b>	<b>Multiplicity</b>	<b>Extinction length [nm]</b>
1	1	1	2.063	0.485	63.00	8	356.485
2	2	0	3.368	0.297	269.00	12	164.857
3	1	1	3.950	0.253	1000.00	24	111.706
2	2	2	4.125	0.242	17.00	8	487.963
4	0	0	4.764	0.210	363.00	6	84.456
3	3	1	5.191	0.193	6.00	24	1290.576
4	2	2	5.834	0.171	111.00	24	275.632
3	3	3	6.188	0.162	71.00	8	192.966
5	1	1	6.188	0.162	320.00	24	157.782
4	4	0	6.737	0.148	767.00	12	69.050
5	3	1	7.045	0.142	15.00	48	955.009
6	2	0	7.532	0.133	47.00	24	372.875
5	3	3	7.809	0.128	121.00	24	228.206
6	2	2	7.900	0.127	6.00	24	1041.792
4	4	4	8.251	0.121	79.00	8	158.323
5	5	1	8.505	0.118	8.00	24	834.869
7	1	1	8.505	0.118	1.00	24	2250.328
6	4	2	8.912	0.112	54.00	48	452.592
5	5	3	9.147	0.109	81.00	24	257.527
7	3	1	9.147	0.109	112.00	48	310.670
8	0	0	9.527	0.105	105.00	6	110.848
7	3	3	9.748	0.103	0.00	24	12904.182

**Fe<sub>2</sub>O<sub>3</sub>**

<b>h</b>	<b>k</b>	<b>l</b>	<b>d<sup>-1</sup> [nm<sup>-1</sup>]</b>	<b>d [nm]</b>	<b>Intensity</b>	<b>Multiplicity</b>	<b>Extinction length [nm]</b>
-1	0	2	2.716	0.368	287.00	6	161.173
1	0	4	3.704	0.270	1000.00	6	73.961
1	1	0	3.973	0.252	620.00	6	90.697
0	0	6	4.363	0.229	2.00	2	918.840
1	1	3	4.532	0.221	460.00	12	139.445
2	0	2	4.812	0.208	16.00	6	518.508
-2	0	4	5.432	0.184	477.00	6	88.390
1	1	6	5.901	0.169	760.00	12	95.073
2	1	1	6.112	0.164	16.00	12	643.066
-2	-1	2	6.240	0.160	27.00	12	491.847
-1	0	8	6.253	0.160	113.00	6	169.108
2	1	4	6.730	0.149	426.00	12	118.828
3	0	0	6.881	0.145	586.00	6	70.864
-2	-1	5	7.074	0.141	10.00	12	766.000
2	0	8	7.409	0.135	34.00	6	283.100
1	0	10	7.625	0.131	168.00	6	125.715
1	1	9	7.656	0.131	90.00	12	242.852
2	1	7	7.921	0.126	6.00	12	895.371
2	2	0	7.946	0.126	73.00	6	186.888
3	0	6	8.148	0.123	4.00	12	1188.211
2	2	3	8.240	0.121	57.00	12	294.402
-3	-1	1	8.302	0.120	3.00	12	1343.400
3	1	2	8.397	0.119	34.00	12	378.919
-2	-1	8	8.407	0.119	56.00	12	292.524
-2	0	10	8.598	0.116	78.00	6	173.876
0	0	12	8.726	0.115	10.00	2	278.334
-3	-1	4	8.767	0.114	111.00	12	203.689
3	1	5	9.034	0.111	2.00	12	1537.496
2	2	6	9.065	0.110	162.00	12	165.925
-4	0	2	9.289	0.108	19.00	6	336.781
2	1	10	9.471	0.106	123.00	12	186.559
1	1	12	9.588	0.104	17.00	12	496.185
4	0	4	9.625	0.104	28.00	6	272.620
-3	-1	7	9.711	0.103	1.00	12	1739.955

**W**

<b>h</b>	<b>k</b>	<b>l</b>	<b>d<sup>-1</sup> [nm<sup>-1</sup>]</b>	<b>d [nm]</b>	<b>Intensity</b>	<b>Multiplicity</b>	<b>Extinction length [nm]</b>
1	1	0	4.475	0.223	1000.00	12	22.990
2	0	0	6.329	0.158	185.00	6	31.800
2	1	1	7.752	0.129	384.00	24	39.870
2	2	0	8.951	0.112	117.00	12	47.560

**WFe<sub>2</sub>**

<b>h</b>	<b>k</b>	<b>l</b>	<b>d<sup>-1</sup> [nm<sup>-1</sup>]</b>	<b>d [nm]</b>	<b>Intensity</b>	<b>Multiplicity</b>	<b>Extinction length [nm]</b>
1	0	0	2.434	0.411	24.00	6	319.011
0	0	2	2.590	0.386	16.00	2	223.822
1	0	1	2.757	0.363	25.00	12	421.692
1	0	2	3.554	0.281	67.00	12	224.976
1	1	0	4.215	0.237	526.00	6	52.183
1	0	3	4.584	0.218	899.00	12	54.148
2	0	0	4.867	0.205	140.00	6	94.060
1	1	2	4.947	0.202	1000.00	12	49.414
2	0	1	5.036	0.199	637.00	12	61.346
0	0	4	5.180	0.193	100.00	2	62.296
2	0	2	5.513	0.181	38.00	12	238.876
1	0	4	5.723	0.175	60.00	12	188.092
2	0	3	6.227	0.161	9.00	12	463.195
1	2	0	6.438	0.155	3.00	12	790.557
1	2	1	6.567	0.152	11.00	24	569.132
1	1	4	6.678	0.150	0.00	12	8689.706
1	0	5	6.917	0.145	82.00	12	145.742
2	1	2	6.940	0.144	34.00	24	321.312
2	0	4	7.108	0.141	3.00	12	731.317
3	0	0	7.301	0.137	105.00	6	88.793
3	0	1	7.415	0.135	1.00	12	1608.811
1	2	3	7.520	0.133	378.00	24	92.166
3	0	2	7.746	0.129	246.00	12	79.588
0	0	6	7.770	0.129	42.00	2	78.999
2	0	5	8.100	0.123	303.00	12	70.141
1	0	6	8.142	0.123	36.00	12	203.004
2	1	4	8.264	0.121	45.00	24	254.986
3	0	3	8.270	0.121	0.00	12	1845.456
2	2	0	8.430	0.119	251.00	6	53.420
3	1	0	8.774	0.114	3.00	12	714.037
2	2	2	8.819	0.113	6.00	12	498.039
1	1	6	8.840	0.113	6.00	12	474.404
3	1	1	8.869	0.113	3.00	24	952.491
3	0	4	8.952	0.112	0.00	12	10467.262
2	1	5	9.131	0.110	72.00	24	192.196
3	1	2	9.148	0.109	9.00	24	545.686
2	0	6	9.168	0.109	89.00	12	121.713
1	0	7	9.386	0.107	25.00	12	225.639
3	1	3	9.596	0.104	168.00	24	122.240
4	0	0	9.734	0.103	15.00	6	205.194
3	0	5	9.758	0.102	0.00	12	2324.662
4	0	1	9.820	0.102	68.00	12	134.799
2	2	4	9.894	0.101	65.00	12	137.418

**FeWO<sub>4</sub>**

<b>h</b>	<b>k</b>	<b>l</b>	<b>d<sup>-1</sup> [nm<sup>-1</sup>]</b>	<b>d [nm]</b>	<b>Intensity</b>	<b>Multiplicity</b>	<b>Extinction length [nm]</b>
0	1	0	1.748	0.572	21.00	2	296.846
1	0	0	2.105	0.475	102.00	2	121.776
0	1	1	2.665	0.375	1000.00	4	48.785
1	1	0	2.737	0.365	261.00	4	94.293
-1	1	1	3.393	0.295	44.00	4	206.212
1	1	1	3.400	0.294	49.00	4	195.318
0	2	0	3.497	0.286	94.00	2	98.144
0	0	2	4.024	0.249	126.00	2	79.188
1	2	0	4.081	0.245	18.00	4	296.066
2	0	0	4.211	0.238	46.00	2	128.501
1	0	2	4.547	0.220	100.00	2	83.623
-1	2	1	4.548	0.220	470.00	4	54.451
1	2	1	4.553	0.220	28.00	4	223.693
-1	1	2	4.861	0.206	43.00	4	174.633
1	1	2	4.872	0.205	40.00	4	179.703
-2	1	1	4.978	0.201	235.00	4	73.657
2	1	1	4.988	0.200	158.00	4	89.818
0	2	2	5.331	0.188	96.00	4	111.589
2	2	0	5.473	0.183	101.00	4	107.210
0	3	1	5.617	0.178	11.00	4	321.207
1	3	0	5.652	0.177	174.00	4	80.346
-1	2	2	5.727	0.175	16.00	4	260.963
-2	0	2	5.816	0.172	110.00	2	70.495
-2	2	1	5.827	0.172	54.00	4	142.460
2	0	2	5.833	0.171	133.00	2	63.983
2	2	1	5.835	0.171	33.00	4	181.573
0	1	3	6.284	0.159	100.00	4	100.717
-1	1	3	6.622	0.151	12.00	4	287.133
1	1	3	6.633	0.151	16.00	4	247.212
2	3	0	6.726	0.149	14.00	4	262.938
-2	2	2	6.786	0.147	36.00	4	160.171
2	2	2	6.801	0.147	32.00	4	170.494
-3	1	1	6.850	0.146	16.00	4	238.988
3	1	1	6.861	0.146	12.00	4	280.779
-1	3	2	6.934	0.144	89.00	4	101.389
1	3	2	6.941	0.144	75.00	4	110.708
0	2	3	6.976	0.143	56.00	4	127.273
0	4	0	6.993	0.143	22.00	2	144.198
2	3	1	7.024	0.142	12.00	4	269.632
1	2	3	7.292	0.137	45.00	4	138.999
-3	0	2	7.479	0.134	24.00	2	132.154
3	2	1	7.499	0.133	104.00	4	89.979
-2	1	3	7.555	0.132	59.00	4	119.262
-1	4	1	7.574	0.132	47.00	4	133.692
2	1	3	7.574	0.132	57.00	4	120.685
1	4	1	7.577	0.132	89.00	4	96.795

**WO<sub>2</sub>**

<b>h</b>	<b>k</b>	<b>l</b>	<b>d<sup>-1</sup> [nm<sup>-1</sup>]</b>	<b>d [nm]</b>	<b>Intensity</b>	<b>Multiplicity</b>	<b>Extinction length [nm]</b>
1	0	0	2.086	0.479	18	2	218.591
0	1	1	2.893	0.346	1000	4	34.856
-1	1	1	2.896	0.345	34	4	189.668
1	1	0	2.919	0.343	3	4	607.726
-1	0	2	3.532	0.283	13	2	196.259
0	2	0	4.085	0.245	85	2	71.268
0	0	2	4.098	0.244	81	2	72.773
-2	0	2	4.106	0.244	141	2	55.072
-2	1	1	4.135	0.242	289	4	54.266
2	0	0	4.171	0.240	159	2	51.460
0	2	1	4.570	0.219	11	4	268.015
-1	2	1	4.572	0.219	4	4	422.526
0	1	2	4.578	0.218	7	4	332.124
-2	1	2	4.586	0.218	54	4	119.305
1	2	0	4.587	0.218	5	4	399.286
2	1	0	4.644	0.215	44	4	130.584
-1	2	2	5.400	0.185	24	4	165.207
1	2	1	5.438	0.184	6	4	337.335
-3	0	2	5.472	0.183	32	2	100.614
-1	1	3	5.771	0.173	22	4	165.673
-2	1	3	5.775	0.173	153	4	62.979
0	2	2	5.786	0.173	281	4	46.469
-2	2	2	5.792	0.173	158	4	62.036
1	1	2	5.829	0.172	3	4	421.770
2	2	0	5.838	0.171	164	4	60.580
2	1	1	5.868	0.170	179	4	57.893
-3	1	1	5.875	0.170	35	4	129.845
3	0	0	6.257	0.160	11	2	160.280
0	3	1	6.461	0.155	98	4	74.568
-1	3	1	6.462	0.155	8	4	266.592
1	3	0	6.473	0.155	6	4	314.195
0	1	3	6.477	0.154	96	4	75.026
-3	1	3	6.488	0.154	42	4	113.887
-3	2	2	6.828	0.146	25	4	144.930
-2	0	4	7.063	0.142	51	2	70.042
-2	3	1	7.105	0.141	123	4	63.423
2	0	2	7.178	0.139	61	2	63.348
-4	0	2	7.192	0.139	57	2	65.747
-2	1	4	7.353	0.136	5	4	301.910
-1	0	4	7.360	0.136	12	2	140.124
-3	0	4	7.369	0.136	14	2	130.410
2	3	0	7.412	0.135	9	4	230.471
2	1	2	7.463	0.134	8	4	241.924
3	2	0	7.472	0.134	11	4	207.539
-4	1	3	7.716	0.130	37	4	111.609
3	1	1	7.779	0.129	6	4	264.747

**WO<sub>3</sub>**

<b>h</b>	<b>k</b>	<b>l</b>	<b>d<sup>-1</sup> [nm<sup>-1</sup>]</b>	<b>d [nm]</b>	<b>Intensity</b>	<b>Multiplicity</b>	<b>Extinction length [nm]</b>
1	0	0	1.582	0.632	659.00	6	113.223
0	0	1	2.565	0.390	687.00	2	50.307
1	1	0	2.740	0.365	242.00	6	141.880
1	0	1	3.014	0.332	215.00	12	203.250
2	0	0	3.164	0.316	1000.00	6	65.010
1	1	1	3.753	0.266	117.00	12	247.017
2	0	1	4.073	0.246	397.00	12	128.636
2	1	0	4.186	0.239	25.00	12	510.577
3	0	0	4.747	0.211	123.00	6	151.344
0	0	2	5.130	0.195	240.00	2	60.227
1	0	2	5.368	0.186	101.00	12	221.931
3	0	1	5.395	0.185	102.00	12	220.583
2	2	0	5.481	0.182	384.00	6	79.662
3	1	0	5.705	0.175	115.00	12	202.186
1	1	2	5.816	0.172	75.00	12	247.553
2	0	2	6.027	0.166	365.00	12	110.192
2	2	1	6.051	0.165	264.00	12	129.373
3	1	1	6.255	0.160	95.00	24	300.760
4	0	0	6.329	0.158	254.00	6	91.205
2	1	2	6.621	0.151	13.00	24	787.672
4	0	1	6.829	0.146	187.00	12	144.648
3	2	0	6.897	0.145	68.00	12	239.494
3	0	2	6.989	0.143	77.00	12	223.206
4	1	0	7.251	0.138	29.00	12	354.072
3	2	1	7.358	0.136	61.00	24	344.271
2	2	2	7.507	0.133	284.00	12	112.003
3	1	2	7.672	0.130	87.00	24	282.298
4	1	1	7.691	0.130	21.00	24	577.282
0	0	3	7.694	0.130	37.00	2	124.832
1	0	3	7.855	0.127	15.00	12	477.958
4	0	2	8.147	0.123	218.00	12	122.772
1	1	3	8.168	0.122	12.00	12	522.672
2	0	3	8.320	0.120	49.00	12	256.228
4	2	0	8.372	0.119	148.00	12	146.669
3	2	2	8.595	0.116	62.00	24	316.926
4	2	1	8.756	0.114	109.00	24	237.075
5	1	0	8.809	0.114	26.00	12	342.906
4	1	2	8.882	0.113	29.00	24	455.915
3	0	3	9.041	0.111	18.00	12	401.726
5	1	1	9.175	0.109	25.00	24	483.616
2	2	3	9.447	0.106	61.00	12	214.886
6	0	0	9.493	0.105	39.00	6	188.854
3	1	3	9.578	0.104	22.00	24	505.863
4	3	0	9.624	0.104	8.00	12	590.067
4	2	2	9.819	0.102	166.00	24	181.410
6	0	1	9.834	0.102	28.00	12	309.897

# Curriculum Vitae

## Personal Data:

**Name:** Julia Toifl  
**Birth date:** March 26, 1993  
**Birth place:** Hollabrunn, Austria

## Education:

**March 2015 – Oct. 2016:** Master studies in Technical Physics at the Technical University of Vienna, Austria  
**Oct. 2011 – March 2015:** Bachelor studies in Technical Physics at the Technical University of Vienna, Austria  
**Sept. 2003 – June 2011:** Secondary school with focus on linguistics in Hollabrunn, Austria  
**Sept. 1999 – June 2003:** Elementary School in Augenthal, Austria

## Professional Experience:

**Sept. 2015 – Nov. 2015:** Project assistant in the working group “Advanced Magnetism Group” under the leadership of Prof. Josef Fidler, Technical University of Vienna, Austria  
**Aug. 2013:** Student apprentice at the OMV Refining & Marketing GmbH  
**July 2013:** Student apprentice at the Otto Bock HealthCare GmbH

## Presentations:

**April 2016:** 6<sup>th</sup> ASEM Workshop in Leoben, Austria  
Presentation of the diploma thesis topic “TEM/STEM Characterization and Modeling of the superparamagnetic transition of FeW nanoparticles”

## Additional Qualifications:

**Mother tongue:** German  
**Foreign languages:** English (Cambridge First Certificate Niveau B2)  
French (DELF-Certificate Niveau A2)  
Spanish (TELC-Certificate Niveau A2)  
**Economic education:** Entrepreneur Licence of the Austrian Federal Economic Chamber (Module A, B, C)